Doctoral Dissertation
Doctoral Program in Metrology (34^{th}cycle)

Metrology Infrastructure for Energy and Power Quality in DC Railway Systems

By

Davide Signorino

******

Supervisor(s):
Ph.D. D. Giordano

Doctoral Examination Committee:
Prof. Rietveld Gert , Referee, University of Twente, Enschede, The Netherlands
Prof. Di Cara Dario, Referee, National Research Council (CNR)

Politecnico di Torino
2022

Declaration

I hereby declare that, the contents and organization of this dissertation constitute my own original work and does not compromise in any way the rights of third parties, including those relating to the security of personal data.

Davide Signorino
2022

* This dissertation is presented in partial fulfillment of the requirements for **Ph.D. degree** in the Graduate School of Politecnico di Torino (ScuDo).

Acknowledgements

I would like to acknowledge my Ph.D. supervisor Domenico Giordano for his dedication, full availability and for leading me in this three-year journey.

Special thanks also to Gabriella Crotti from INRIM and to Daniele Gallo, Antonio Delle Femine, Mario Luiso and Carmine Landi from the University of Campania Luigi Vanvitelli for their essential collaboration for the entire duration of the doctorate.

At last, I would like to thank the reviewers for the considerations and the comments provided for this thesis work to enhance its scientific relevance and overall quality.

Abstract

The European community for over a decade is supporting scientific and technological studies in order to make public transport low environmental impact. The metrological community plays a key role in fostering this improvement, in fact all the activities described in this thesis work are carried out in the framework of the European project 16ENG04 MYRAILS (Metrology for Smart Energy Management in Electric Railway Systems). Within the project, a metrological infrastructure for accurate measurement of energy exchange and for reliable system monitoring is developed, which underpins the implementation of an energy efficient management of the European DC railway and metro system.

To this purpose, this work describes the measurement setups developed and the results of two on-board DC train measurement campaigns devoted to the accurate estimate of the energy exchanged between the locomotive and the DC feeder and the electrical energy wasted during the braking stage. Moreover, one of the two measurement campaigns is conducted onboard of a train operating on the metro line, where a reversible substation is installed. In this case, the aim is to quantify the impact of these technologies in a real application, providing information on energy saving in the different operating conditions and presenting a methodology to quantify them.

Another topic dealt with in-depth in this thesis work is the accurate determination of the energy dissipated on the braking rheostats. This measure is not necessary for the billing of the dissipated energy, but having an accurate and reliable knowledge of this quantity is a precious tool for collecting internal data useful in the design of more efficient DC power supply systems and real-time efficiency management of energy flows. In this context, two methodologies for the measurement of power dissipated on braking resistors are reported: the first is based on an offline algorithm which involves the measurement of the current, acquired with a high sampling

frequency, and the compensation of the current transducer frequency response. This methodology has exceptional performances but it is impossible to be applied online. The second methodology presented is designed to be applied directly on board with the instrumentation already available, and performances are comparable to the ones of the offline method.

A relatively new, but very relevant, topic in the railway world is the power quality issue. The grown interest is driven by technical and economic issues. The widespread monitoring of the railway and metro system performed both on-board and in supply substations can be not only a valuable tool for a much more predictive diagnosis of the entire railway electric system but also an economic tool to promote trains and supply system even more efficient. The research activity presented in this thesis work, enlarge the typology of Power Quality events found in the huge amount of data provided by the measurement campaigns, with a particular focus on arc events detected at pantograph.

Finally, the European commission requires that the billing for the energy consumption of the railway systems shall be computed on the actual energy consumed by 2019. The supply grid of the railway system is not ideal; it is strongly characterized by a non-stationary regime and many power quality events verified during the normal operations. In order to evaluate the metrological reliability of an energy meter under actual operating conditions, calibration set ups and procedures which go beyond the well-known procedures developed for pure DC regimes are required. Therefore, the realization of an accurate and reliable calibration system for evaluating the measurement of the energy absorbed/exchanged between the train and the railway grids is needed. The calibration system here presented takes into consideration the harsh on board measurement circumstances and the frequent non-stationary electrical conditions.

Contents

List of Figures

List of Tables

Chapter 1

Overview on Railway Systems

1.1 Introduction

A third of the total energy consumption in Europe is represented by transportation and the main actor of the transport technologies is the fossil fuel. In order to fight the global warming and climate change, this is expected to change gradually by 2050, based on current trends and policies. As reported in 2011 White Paper on Transport [1], a sustainable path for transport sector is possible only with an integrated system approach among the countries of European Union. The starting point of this approach is the actions on overall vehicle efficiency, encouraging the low emission means of transport and infrastructure, and the long-term shift to alternative fuels for transportation, based on an essential increase in transport system efficiency. Propulsion vehicle have been greatly improved in terms of energy efficiency thanks to the electric supply and the use of batteries. Electricity can also be supplied via catenary and pantograph systems, like in railway, tramway and metro systems or hypothetically via street electrification. Actually, the transportation on rail is one of the most ecological mode for mobility. New studies [2] predict that passenger transport activity will increase by 16% over the period 2015-2030 and by 35% by 2050. In the same time windows, the activities for passenger rail increase by 36% between 2015 and 2030, 72% for 2015-2050.

The project of an European Railway Area requires investments not only in the rolling stock but also in the rail infrastructure and a database that shows where electrification should be present in next years is already been developed by the

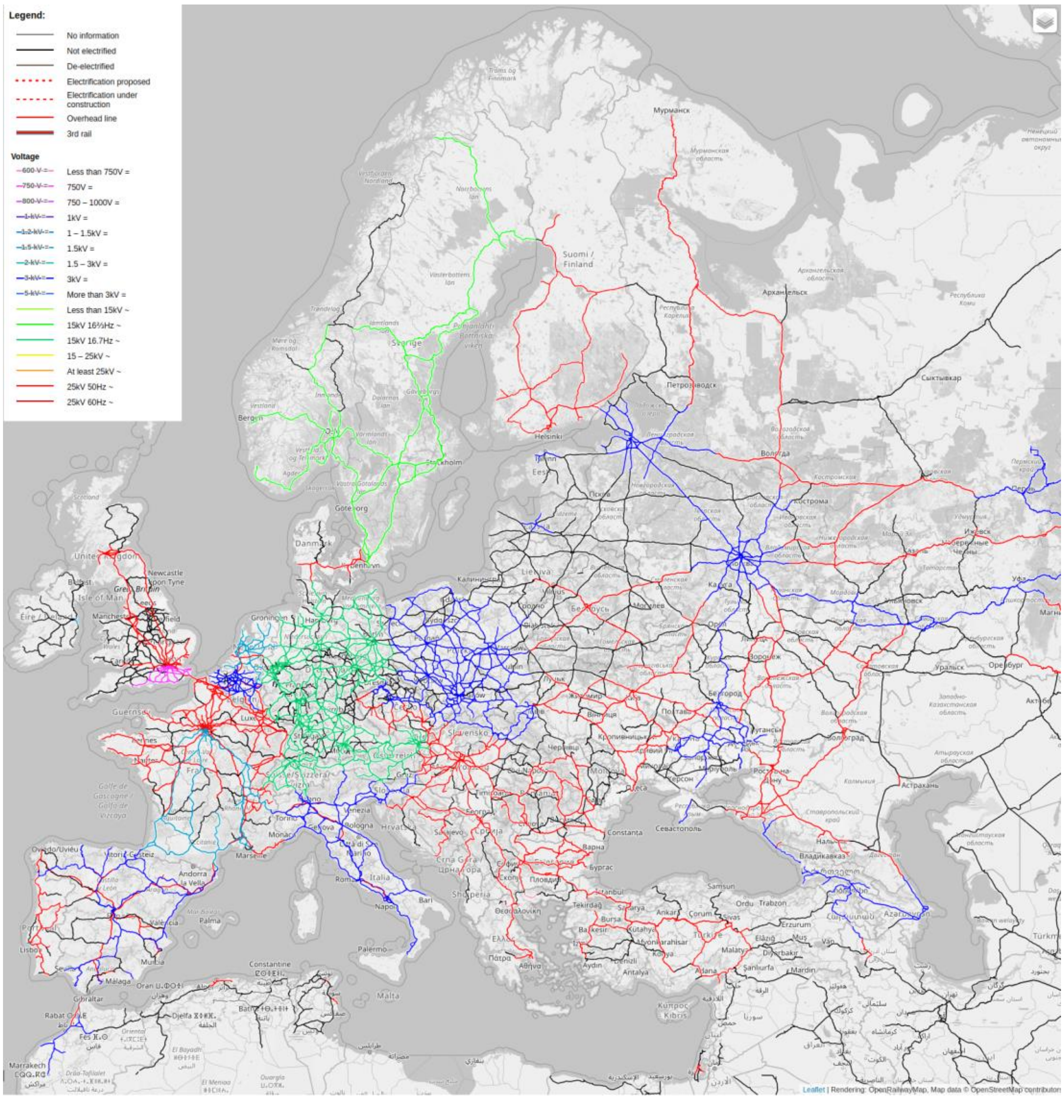

https://www.reddit.com/r/europe/comments/rqkkl1/electrified_railways_of_europe/

Fig. 1.1 Electrified Railways of Europe

European Union Agency. One of the main problems in the implementation of this project lies in supplying rail lines that today operate with different amplitude levels, DC or AC and even different frequencies for AC, as shown on the map in Fig. 1.1.

For the High Speed/High Capacity line predominantly at 25 kV and 50 Hz are used, except for Germany, Austria, Switzerland in which the supply system is at 15 kV and 16.7 Hz. In either case, the highest qualitative standards (peak train speeds, greatly reduced travel time ...) are guaranteed.

From a transmission point of view, AC systems are better than DC because they can distribute energy at high voltages over a small size conductor wire, whereas DC needs a large, heavy wire or, on many DC railways, an extra rail. DC also needs more frequent feeder substations than AC the ratio for a railway averages at about 8 to 1. It varies widely from one application to another but this gives a rough idea. Over the hundred years or so since the introduction of electric traction on railways, the rule has generally been that AC is used for longer distances and main lines and DC for shorter, suburban or metro lines. DC gets up to 3 kV, while AC uses 15÷50 kV. Until recently, DC motors were very easy to control and have been the preferred type for railways because the three-phase alternating current motors require very complicating locomotion regulation. For this reason, even trains powered from AC supplies were usually equipped with DC motors.

In DC systems, the supply line voltage is normally 3 kV, but experiments are also being carried out at 6 kV: the power is drawn from a high-voltage three-phase AC line and converted to DC at the desired voltage in appropriate supply substations. In the single-phase AC system with a frequency of 16.7 Hz, there is a frequency conversion plant the reduces by 1/3 the frequency of high-voltage AC lines to the industrial frequency of 50 Hz. Subsequently, the power substations lower the voltage to the value of 15 kV ordinarily adopted. In the single-phase industrial-frequency AC system, there is no longer any need to convert the frequency of high-voltage AC lines; the power substations simply lower the voltage to 25 kV or, in some cases, to 50 kV.

The characteristics of the newly installed transformers should be able to ensure a virtually constant output voltage when the value of the current absorbed by the trains ranges from a minimum of 75 A to a maximum of 3 kA. The rectifiers used by RFI, the Italian infrastructure manager, are usually equipped with silicon diodes divided into two systems for a total power of 3600 kW. In Italy the substations are spaced approximately 20 km, but in some sections designed to allow very high speeds, the distance between a substation and the next is reduced to about 16 km.

1.1.1 Description of dynamic braking

A major reason why electrified rail systems are considered to be very sustainable and energy-efficient lies in the usage of electric motors. Compared to combustion

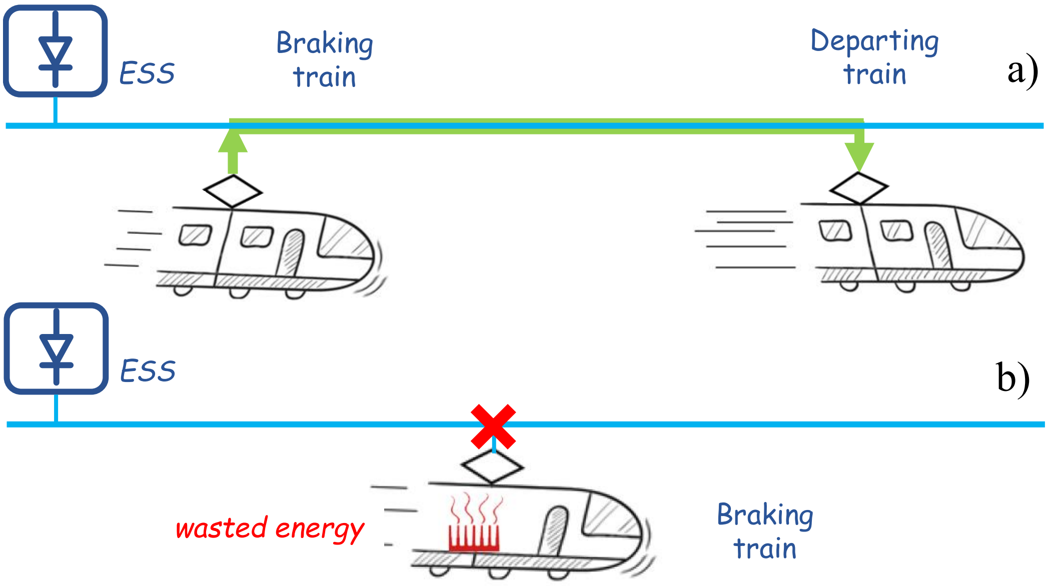

Fig. 1.2 Energy exchange between trains (a), energy dissipation on-board (b).

engines, the electric motors implements the dynamic braking, a regenerative braking system, that allow the conversion of the braking kinetic energy into the electrical form. In this way is possible to avoid mechanical braking which is subject to wear (leading to high maintenance cost). Moreover it enables the recovery of energy, when possible, by injecting it in to the catenary.

As described in [3], in particular for DC supplied railways, the overhead contact line is not always able to receive this energy, depending on the presence of other trains in traction simultaneously, the distance of this train, the presence of storage systems on the line [4, 5] or the presence of reversible substations [6, 7].

Currently, the DC supply system of a railway network is obtained by means of unidirectional rectifier, that does not allow the energy flow back to the mains grid. For this reason the energy recovered during braking can only be used by other trains on the line. When there is no other train, injection is not possible and the trains use a chopper to dissipate braking energy on the on-board rheostats bank.

In Fig. 1.2a two trains supplied by unidirectional Electrical Sub Station (ESS) are depicted: the one on the left is braking with a generation of energy; the other is accelerating thus recovering the braking energy from the first train. To allow the energy flow between the trains, the voltage at the pantograph of braking train rises, in order to win the line resistance between the two trains.

In Fig. 1.2b the train accelerating is missing, thus the train cannot inject power on the line otherwise the voltage would rise indefinitely. In fact, when voltage exceeds a certain threshold, the braking chopper takes action dissipating all the power on board.

More in general, mixed situations can occur, in which part of the energy can be injected and the energy surplus is dissipated on board [3]. The chopper implements a Pulse Width Modulation (PWM), so varying the duty cycle it is able to modulate the amount of the energy dissipated.

For the Italian locomotives operating in 3 kV systems, the energy may be completely recovered only at voltages lower than 3.8 kV, over this value the on-board dissipation starts to limit the voltage increment. In details, for voltage value between 3.8 kV and 3.9 kV the train implements a mix of dissipative and regenerative braking. Above 3.9 kV, purely dissipative braking is applied to avoid further voltage rise to an unacceptable level [8].

Obviously, the installation of storage systems or Reversible SubStations (RSS) can significantly foster the energy efficiency, increasing the possibility to recover braking energy. Currently some experimental installations are ongoing in Europe [7]. For this reason, it is very important measuring the amount of energy that trains waste during braking, so as to provide valuable information for dimensioning and positioning RSS or energy storage systems [5].

1.2 Metrology infrastructure for railway applications

The white paper for efficient transport system [1] requires, as one of the main aim, the high efficiency for the new European railway area. The metrological community provided an important contribution developing means and method for the estimation, with high reliability, of the energy flows measured on-board locomotives and the Power Quality (PQ) events that usually occurs between the pantograph and the supply line.

The activities of this thesis work are carried out within the European project MyRails [9], funded by EURAMET in the EMPIR program and ended in January 2021. Within the project, a metrological infrastructure for accurate measurement of energy exchange and for reliable system monitoring is developed, which underpins the implementation of an energy efficient management of the European DC railway and metro system. The covered topics are the following:

- the measurement campaigns on board trains in Italian Piedmont region and Madrid metro;
- the measurement issue of the energy dissipated by the braking rheostats;
- the PQ events experienced on board trains;
- the characterization of the energy meter installed on board trains.

1.2.1 Introduction to the measurement campaigns

The development of an efficient and environment-friendly electric railway system plays a key role in the evolution of transport worldwide. Reliability and absence of local emissions but also the high energy efficiency, compared with other means of transportation, are some of the most important advantages of the railway system. Nevertheless, further fostering the energy efficiency of railway system is an important issue, considering that the total amount of energy required for the European railway system is a huge number (36.5 TWh) and that the growing need of vehicles with a higher on-board comfort and, in turn, higher transport capacity entails a growing demand for traction energy. Furthermore, given the highly competitive context of the other modes of urban transportation, reduction in energy consumption is crucial for the rail to keep its competitiveness as the most sustainable and economic means of transport.

In order to perform evaluations on energy efficiency, together with Trenitalia (the main Italian railway company) a measurement campaign has been carried out on a 3 kV DC railway locomotive, the E464-041, operating in commuter service. 78 journeys have been recorded and about 4 TB of data have been stored with a sample frequency of 50 kHz. The objectives of these campaign were the measurement of the energy exchanged between the train and catenary, more in specific the electrical energy wasted and reinjected to the supply line during braking, and the identification of PQ events occurring at pantograph.

Adopting a measurement system capable of acquiring fast-transient phenomena with high frequency content is important for a accurate PQ study. The existing measurement equipment aboard trains only has a sample rate up to 10 Hz, making it impossible to identify phenomena like rapid fluctuations in the monitored signals. In order to examine rapid voltage or current variations, such as the chopped currents in the train's braking rheostats, a system with wide bandwidth has been design, developed and presented in this thesis work.

To improve the efficiency of the railway system, the European policy pushes railway system operators towards improving their capabilities of re-using the electrical energy produced by the braking. New installations of reversible substations in DC railway system, able to transfer the excess of energy, produced during braking to the upstream AC network, can improve energy saving. A reliable procedure in the estimation and measurement of the potential energy saved by RSSs is then a valuable tool in the cost-benefit evaluation. Typically, up to 50% of the traction energy is dissipated in braking process, but only 10%-30% is sent back to the catenary, due to the receptivity of the supply network limited by unidirectional nature of the substations. Nowadays, new RSSs, which adopt high voltage high power inverters, allow the bidirectional energy exchange between AC and DC railway grids, saving a traction energy from 11% to 20%. Future goal is to enlarge RSS technology from metros and suburban lines to all DC railways. The high cost of the initial investment requires an accurate estimate of the energy saved by the RSS, up to now carried out only in an indirect way with low accuracy. The scientific and technical world pays great attention to the new solutions that allow the saving of such energy. Several technical solutions are proposed: reversible substations that inject the energy to the upstream AC grids for suburban or railway[10, 11], storage systems onboard and/or in substation [12, 13], able to collect and store the braking energy, and algorithms for the identification of the optimal speed profile [14], and algorithms for the cooperation among braking and absorbing of multiple trains [15]. Most of these activities are based on simulation, which do not represent the actual variability of real cases. The actual energy dissipated depends not only on braking effort and time duration but also on the driving style, the traffic conditions, the catenary resistance, and even on the difference between the supply voltage amplitude and the threshold voltage that triggers the insertion of the braking rheostat [16]. Several studies have shown that these massive infrastructural modifications ensure the recovery of the energy dissipated on the braking rheostats from 10% up to 30%. The quantification of the real wasted energy enables to evaluate the potential benefit before an infrastructural investment or to measure its impact afterwards.

For this reason, a measurement campaign has been carried out on a Metro Madrid metro train, working in a 1.5 kV DC line. From a metrological point of view, this is a non-common activity as a reversible substation is installed on this line. Thanks to the availability of MetroMadrid operators, it was possible to study the impact of the reversible substation performing measurement when the latter is ON and OFF.

1.2.2 The power wasted on braking rheostats

The data provided by these measurement campaigns allow the study of another important research topic: the accurate measure of the power dissipated on board rheostats. As described in Chapter 3 an accurate evaluation of the power/energy wasted during a braking is not a trivial task for several reasons. The data obtained, not for billing purposes, shows that along a 120 km route, a train wastes on average 200 kWh on the rheostats [9]. Considering that several trains of the same type travel on the same route, a consumption of 1 GWh per year is estimated for a single route. To give an idea of the amount of energy, just think that this value corresponds to the annual consumption of about 365 families. Having accurate knowledge of wasted energy is a valuable for insiders, as, for example, it can help in the design, sizing and positioning of energy storage systems and/or reversible substations. It is clear that the knowledge provided by this information can facilitate a decision-making process related to infrastructure investment that points towards energy saving.

1.2.3 The analysis PQ events detected in measurement campaigns

The efficient use of the infrastructure, encouraged by the European Union, requires new constraints for the railway supply systems. In this scenario, an accurate knowledge of the real-time PQ is a valuable tool to foster the efficiency of the whole railway system by “awarding” the good power quality delivered and absorbed.

As to the assessment of the power supply quality, [17] defines limit variations for frequency and supply voltage. Today, monitoring is required only at commissioning or on response of problems. Standard [18] deals with the quality interface between traction unit and fixed installation, it defines the procedure of compatibility assessment (by simulation, test in the lab and on test tracks) only for new rolling stock or new infrastructure component.

Significant research on definitions, measurement systems and algorithms related to PQ in fixed installations, AC transmission/distribution grids, have been carried out in the last 10 years. Unfortunately, techniques are not suitable to railways, because the time interval of interest are longer, the trains are mobile, and the PQ phenomena are not the same.

After a classification of the main characteristics PQ events of the railway system, in this thesis work numerous PQ events in the 3 kV DC railway and the 1.5 kV DC metropolitan systems are reported. In particular, a section is dedicated to electric arc events with the conducted effects on the supply grid. In facts, thanks to the very dense sampling of the waveforms acquired during the measurement campaigns, it was possible to develop and patent a technique for detecting electric arcs. At the time of writing, an industrial prototype of an energy meter that implements this functionality has already been realized; the next activity relates to a field test of the prototype.

1.2.4 Calibration of the Energy Measurement Function

Finally, this work focuses on the characterization of the railway metering units, with a view to its performances not only in ideal conditions, with pure DC signals, but even in real test case situations. Considering the overall annual energy consumption of the European railway system, about 36.5 TWh, and the ambitious target of reducing CO_2 railway transport emissions to 50% by 2030, it is clear that an efficient use of the energy in the railway system is mandatory. To this end, accurate and reliable knowledge of the absorbed/exchanged energy between the train and the railway grid is essential, considering the harsh on-board measurement conditions. The “new deal” established by the European commission through the Technical Specification on Interoperability [19] imposes billing to be performed on real rolling stock energy consumption. This choice will foster energy saving and thus will transform the railway system in a more sustainable means of transport. All the trains shall be equipped with an Energy Measurement Function (EMF), whose measurement accuracy has to be assessed and periodically re-verified, as required by [20]. To assess the metrological reliability of the EMF under operating conditions, calibration setups and procedures, which go beyond the well-known procedures developed for pure continuous regimes, are required. For energy measurements on-board trains, the in force European standard [20] adopts the same requirements given for fixed 50 Hz installation, so disregarding wideband effects specific for railway systems.

With respect to [21], the present work aims to improve the metrological reliability and decrease the uncertainty of the energy measuring system. To this end, a particular generation setup for calibration purposes, capable of generating a phantom power up to 10 MW and superimposed voltage distortions up to 10 kHz and current distortions in a bandwidth up to some hundred of hertz is developed. Moreover, this generation system is able to emulate real operating conditions generating signals obtained in on-board measurement campaigns. This could improve the reliability and accuracy of the energy billing of a railway undertaking. Finally, knowledge of EMF behaviour under harsh waveforms (harmonic pollution, arc events, dip, swell) will lead to the development of new EMFs with better performances in terms of accuracy and reliability.

Chapter 2

Energy flow analysis on board trains

For over a decade, Europe is encouraging the technological and scientific community in order to reduce the environmental impact of public transport. Therefore, it's clear that the accurate knowledge of the railway system's energy consumption is fundamental. In this context, this chapter describes measurement setups and the results of two on board DC train measurement campaign: one in a conventional 3 kV railway system in Piedmont region and one in a 1.5 kV metro system in Madrid. Both these campaigns were dedicated to the accurate evaluation of the energy exchanged between the locomotive and the DC supply line and the energy that is wasted in the braking phase. These information are crucial in the precise determination of the amount of energy that could be saved because can be useful in the decision process related to the infrastructure investment. In fact, having this knowledge, investments such as installation of reversible substation or on-board storage systems in order to improve energy efficiency can be very fruitful.

2.1 Realization of an high performance measurement system for on-board trains applications

One of the primary goal of this thesis project is to create a flexible instrument that can accurately capture and handle a variety of signals from trains or substations. In order to achieve this, the National Instrument Compact Rio was selected. This device enables the use of several acquisition modules depending on the type of input signal

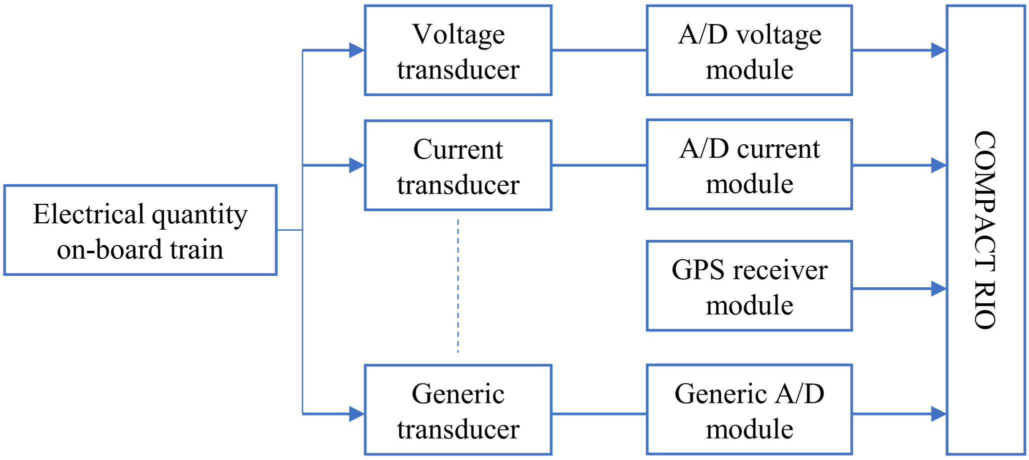

Fig. 2.1 Measurement system architecture

and a GPS receiver module for relating timing data. The measurement system's architecture presents the configuration provided in Fig. 2.1.

It is simple to understand that any type of physical quantity can be measured and processed by altering or introducing acquisition modules downstream of the transducers; specifically, for the measurement campaign that will be illustrated in this thesis work, the Compact Rio 9034 was used to measure the signals coming from the transducers placed on the train.It use ad hoc network architecture designed for connecting scattered metering units. The network interfaces, high-reliability power supply, real-time configurability, control, mobility and independence make of this instrument a winning choice for the porpoises.

Due to its compact design, the Compact Rio 9034 is a stand-alone reconfigurable embedded chassis with an integrated real-time controller that can be mounted simply on trains and in substations. The system architecture considers measurement devices on substations for managing and monitoring power flow to the train as well as a device on the railway for monitoring power that has been dissipated and returned. High-accuracy measurements require advanced DAQ and control applications, which are provided by NI C-Series modules. Each module comes in a single rugged package with measurement-specific signal conditioning to connect to a variety of sensors and signals, bank and channel-to-channel isolation options, and support for a wide temperature range. These features allow each module to meet the requirements of various applications and environments.

In order to achive the goal of accurately measure the electrical quantities involved in the energy metering and PQ monitoring, the data acquisition system used is composed by two NI 9223 module, with 16 bits resolution, input up to 10 V, 50 kHz sampling frequency, 4 channels each with synchronized sampling among all 8 channels. Moreover, the GPS module NI 9469, capable of providing a Pulse Per Second (PPS) with an accuracy of 100 ns was used for time synchronization. The typical measurement system installed for monitoring electrical quantities on board trains has very low performances from metrological point of view. In facts, it acquires voltage and current at pantograph with a sampling rate of tens of hertz, and it cannot perform any energy analysis. It is easy to understand that a comprehensive analysis of energy flows from this type of systems is not allowed. Moreover, an important upgrade is needed if the measurement subject is the detection and analysis of power quality phenomena. Events such as electric arcs, rapid voltage or current variations of the pantograph, analysis of the behaviour of the chopper of braking resistors and so on require measurement device with high sampling frequency and very high performances in terms of data signal processing.

2.1.1 Synchronization algorithm

The synchronization-related issue is unquestionably one of the measuring device realization's most intriguing issues. Each measurement equipment present on the grid must make reference to a universal time in order to rapidly examine the voltage and current behavior throughout a over a wide area of railway network. The difficulty lies in gathering signal information simultaneously for all devices dispersed across substations and on trains. The time reference is provided by a GPS receiver that can generate a PPS signal with high accuracy and, with a systematic delay, provide the number of nanoseconds since January 1 at 12:00 in International Atomic Time (TAI, from the French name temps atomique international). It is important to build an algorithm that reports the acquired data to the time instants established by the external reference because the acquisition modules clock (single for all), the FPGA clock, and the external time reference are completely independent to one another. The behaviour reported in Fig. 2.2 would occur under perfect circumstances, assuming that the sample step is constant and that its value is equal to the nominal one, that the FPGA clock is exactly the one stated in the specifications, and that the acquisition begins at the time the PPS arrives.

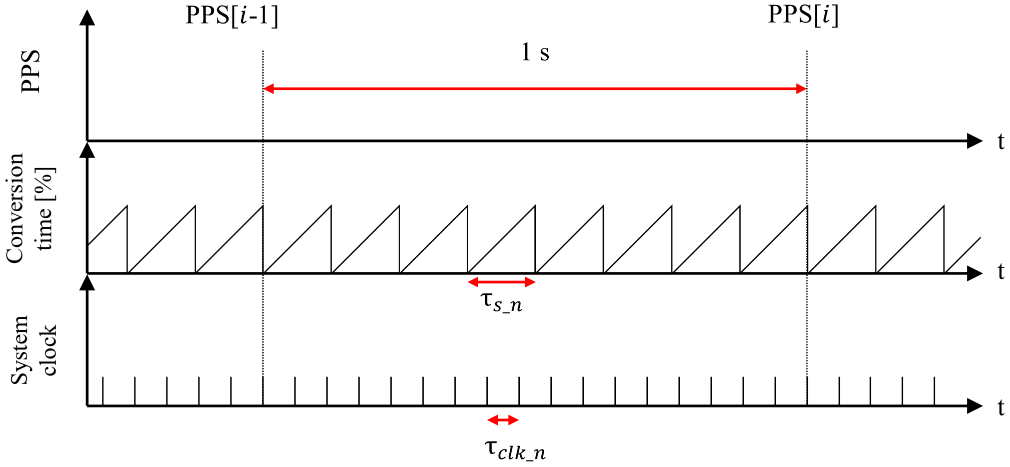

Fig. 2.2 Ideal behaviour of system compared to time

The discrepancy between the nominal values of sampling frequency or system clock frequency and the real ones are not negligible for applications like this one that demand a high precision level, hence these variables must be measured. Fig. 2.3 depicts the actual behavior of the acquisition system, the external reference, and the FPGA clock throughout a typical time period of one second.

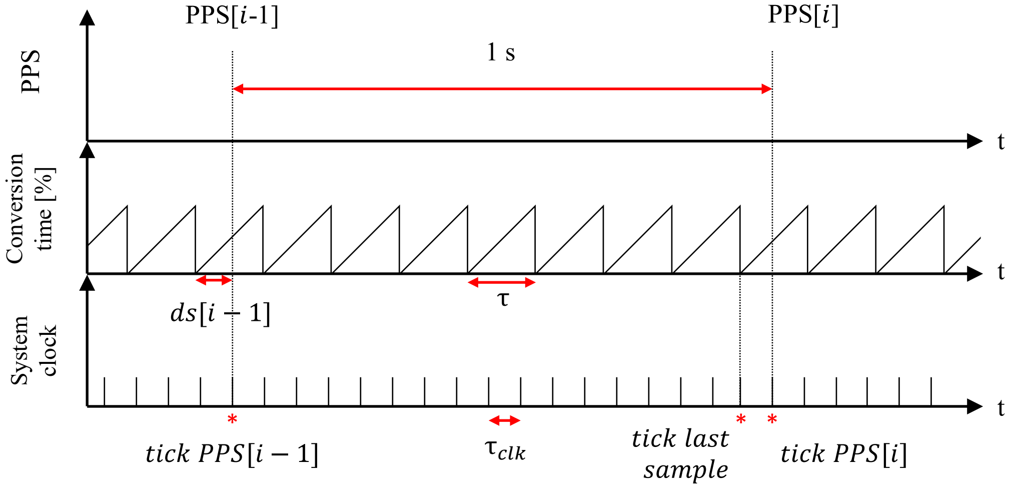

Fig. 2.3 Actual behaviour of system compared to time

Fig 2.3 provides:

- The interval between two PPS occurrences measured in system ticks. The actual FPGA clock frequency is represented by this number (f_{clk})
- The quantity of samples collected between two PPS events (N_s).
- Time value for desynchronization (ds). The difference between the most recent sample acquired and the PPS event is represented by this value.
- $TickPPS[i-1]$, $TickPPS[i]$, $Ticklastsample[i]$ are the system tick value in PPS events and in last sample acquired event. $[i]$ is the index of the seconds.

Considering all the information, the real-time instants at which each point in the interval is sampled can be estimated as follow:

$$TickPPS[i] - TickPPS[i-1] = N_s \tau_s + ds[i] - ds[i-1] \tag{2.1}$$

$$\tau_s = \frac{1}{f_s} = \frac{\delta Ticklastsample}{N_s} \tag{2.2}$$

where: $ds[i] = tickPPS[i] - ticklastsample[i]$ and f_s is the actual sampling frequency.

2.1.2 Data storage and processing

Managing saved data for a system with this performance, operating continuously over time (months), was not an easy task. The Compact Rio 9034 is equipped with an SD interface for data storage. 1 TB SDs were used, which were promptly replaced before the storage space was exhausted. In addition, thanks to the software developed, it was possible to make sure that the Compact Rio's internal memory was used as a filter during the card swap phase, guaranteeing uninterrupted temporal continuity of acquisition.

A comparison was made between the utilization of hard disks and solid state drives, two different storage options with larger allocation space. Hard disks have the advantage of having a much larger allocation space, up to 8TB, but on the train they suffer from the problem of vibrations that can lead to the rupture of the storage system and the resulting loss of all data. On the other hand, Solid state drives, because of their non-mechanical technology, solve the issue of excessive sensitivity to vibrations but, in addition to having a limited maximum capacity (2 TB), are connectable to the measurement system only through the USB port, which is sensitive to variations in the electric and magnetic field present near the installation site on board the train. For SD cards, the Compact Rio provides a shielded and protected encapsulation, which, at the cost of lower maximum storage capacity, ensures the greatest reliability from a data storage point of view.

It is evident that the issue of the massive volume of data must also be taken into consideration throughout the processing step. It was important to handle all the data implementing from scratch Matlab scripts in order to evaluate phenomena lasting a few milliseconds, such as transients and PQ events. In order to analyze data offline, the following functions are used:

- selecting the measurements from the files at particular time intervals;
- correction for the introduced transducers systematic errors;
- implementation of algorithms to calculate power and energy;
- post-processing to accurately assess the amount of energy lost through the brake resistors;
- spectral analysis and time-domain evaluation of single tones;
- a PQ phenomenon analysis.

2.2 Measurement campaign in Piedmont region

An important contribution to the improvement of the European railway system, provided by the metrological community, is the development of means and methods for the estimation of the energy flows on board the locomotive, with high reliability, exchanged between the train and the supply line. In the framework of the European Project 16ENG04 MyRailS [9], a DC 3 kV locomotive for the commuter service has been considered for a measurement campaign. This activity was possible thanks to the participation in the project of Trenitalia, the main Italian railway company. In more than three months 78 journeys have been recorded, and about 4 TB of data have been stored at the sample frequency of 50 kHz. The main objectives of this campaign were to evaluate, at current state, the amount of energy involved in the traction, the one recovered by braking and the amount of energy wasted due to the unavailability of the line in receiving it.

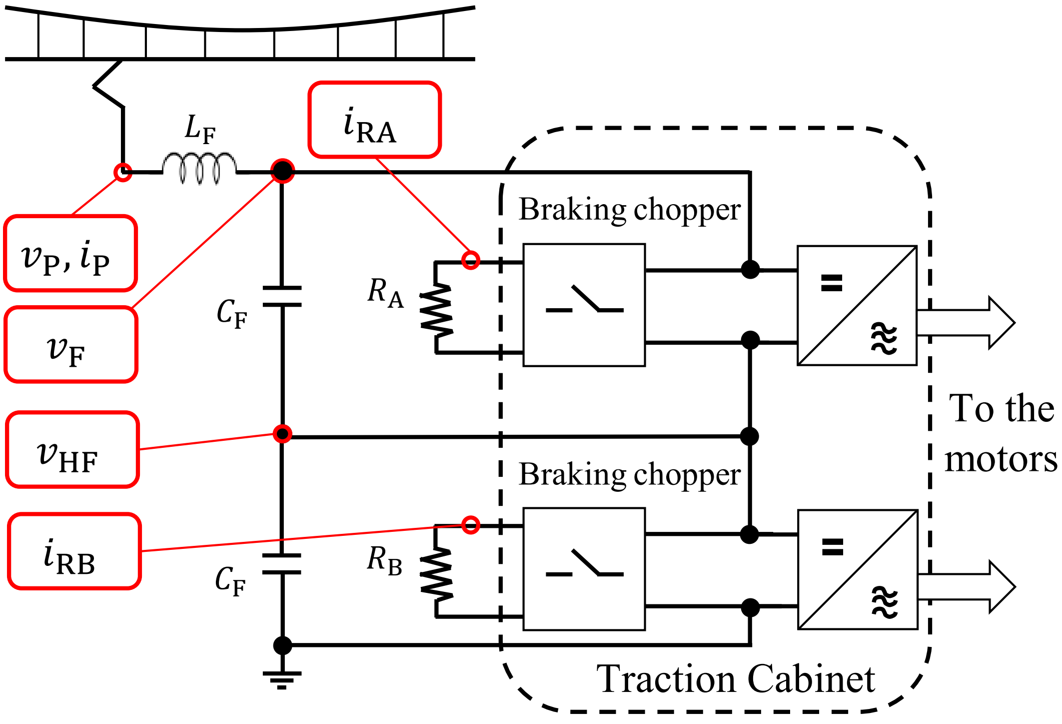

Fig. 2.4 E464 input stage

2.2.1 Trenitalia locomotive E464-041

The Trenitalia locomotive E464-041 was considered as test case. With a rated power of 3.5 MW and a maximum speed of 160 km/h the traction architecture is composed by two inverters, with a rated voltage of 1.5 kV, series connected that supplies four asynchronous three-phase motors. The input stage of the locomotive is composed by a second order low pass filter that is used to limit the disturbances generated by the inverters towards the supply line and vice versa.

The electrical scheme is shown in Fig. 2.4. The inductance L_F, 8.5 mH, and the two identical capacitor C_F, 17.1 mF each, constitute the input stage filter.

In the same figure are highlighted the six measurement points. Upstream the inductance L_F, the voltage v_P and current i_P represent the quantities at pantograph. The filtered voltage v_F, measured in parallel to the capacitors banks, represents the voltage applied to the two inverters, connected in series, that control the asynchronous motors. A chopper system, connected to the inverters, manages the energy that must be eventually dissipated during a braking. In this stage, the train provides an high amount of energy for a very short time so, it happens that the grid is not able to absorb this power and, consequently, it must be partially o totally dissipated by on board resistors known as rheostats. The amount of this energy is regulated through a Pulse Width Modulation (PWM) that controls the switches connected to the rheostat circuitry and the greater is the duty cycle imposed by the Train Control Unit (TCU), the greater is the energy dissipated. From Fig. 2.4 can be noted that the voltage applied to R_{B} rheostat is v_{HF}, that is the one of node between the two capacitors, and i_{RB} represents the pulsed current that flows into it. The same goes for R_{A} where the voltage applied is $v_{\mathrm{F}} - v_{\mathrm{HF}}$ and the current measured is i_{RA}. In Table 2.1 the main characteristics of the braking rheostat are provided:

Table 2.1 Rheostat Characteristic of E464-041

Parameter	**Value**
Maximum power	2 x 1200 kW
Resistance at 20 °C	5 x 1.52 Ω
Maximum resistance variation [20-600]°C	5 %
Operating voltage	3.8 kV
Maximum rms current	900 A
Stray inductance	$\leq 12\ \mu$H
Chopper frequency	260 Hz

Fig. 2.5 is a collection of pictures of the measurement system installed. The supply systems of the current transducers, the voltage transducers and the acquisition system were placed in the ground-connector cabinet (Fig. 2.5(a)). The current transducers for the rheostats were placed at the input box containing the resistors and the cooling system (Fig. 2.5(b)). In the high voltage switchgear, the transducer for i_{P} (Fig. 2.5(c)) and the acquisition system (Fig. 2.5(d)) were accommodated.

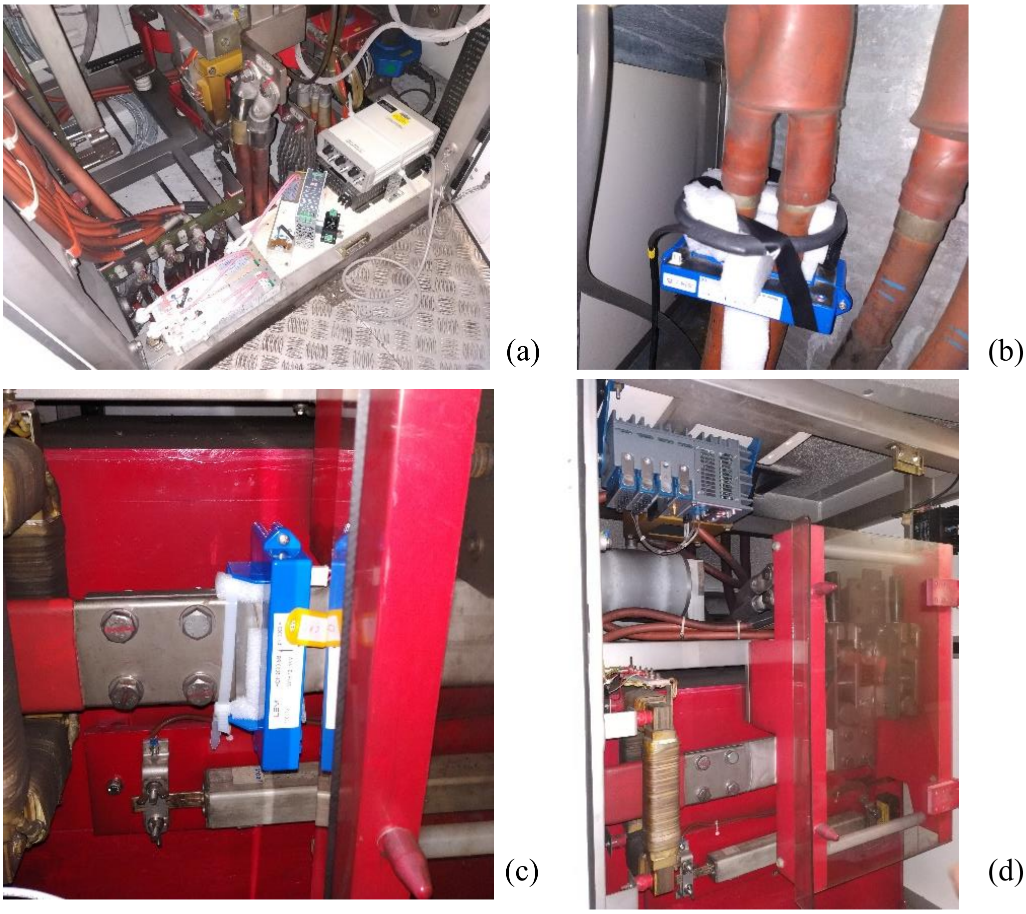

Fig. 2.5 Collection of pictures of installed measurement instrumentation

2.2.2 Transducers set and calibration

For the measurement of the v_P, v_F and v_HF, resistive-capacitive ULTRAVOLT TF40 voltage divider were used. The nominal scale factor is 1000 (V/V) and this type of transducers are designed for accurate high voltage in-line measurements, view and measure ac ripple & noise on DC high voltage and AC signal up to 10 MHz, with an accuracy of 0.25%. In order to measure the current i_P and being acquired by the voltage data acquisition system, the LEM HOP 2000 Hall effect transducer has been used. The primary nominal rms current is 2 kA, corresponding to the output voltage of 4 V. Supplied ($\pm5\%$) at 15 V, this transducer has a flat frequency response from DC to 10 kHz and the accuracy is $<\pm2\%$. This value is not so high but the possibility to insert the probe without interrupting the power circuit, its dynamic and the dimension of the window make this a winning choice. To measure the power dissipated by braking rheostats, two Rogowski coils were used. These probes have a wider band than HOP transducer, actually up to 200 kHz, but they do not allow the measurement of the DC component. All the transducers were previously characterized at INRIM (Italian NMI) laboratories. The measurement chain installed on-board the train is shown in Fig. 2.6.

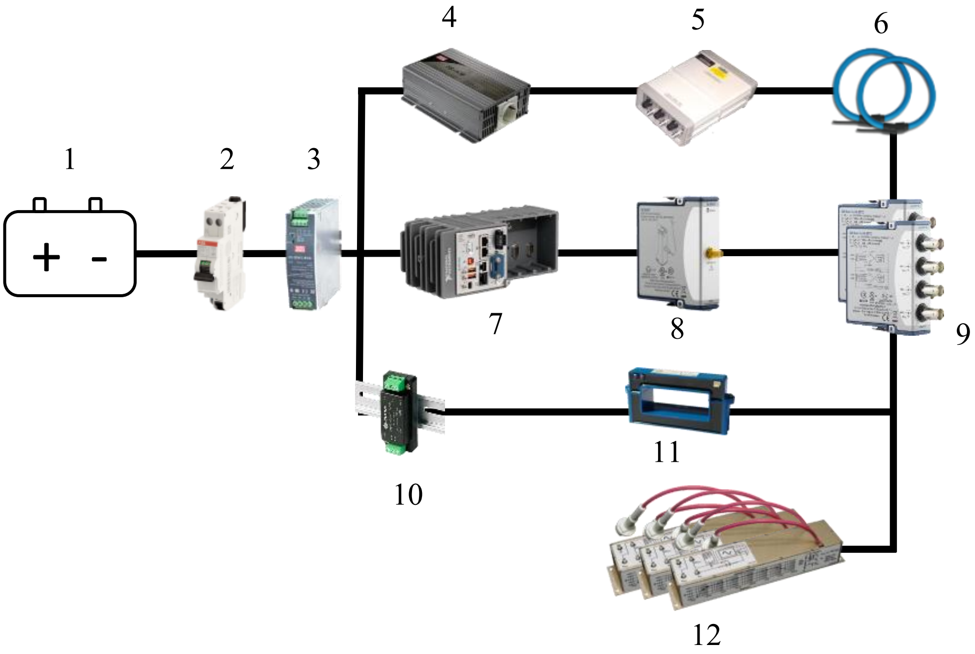

Fig. 2.6 Scheme of measurement chain installed on board E464

The supply system is connected directly to the train battery (1) in order to guarantee a continuous monitoring of the trains signals even when the pantograph is not in contact with the catenary. Downstream the battery, a magneto-thermic switch (2) and a DC/DC 24V-24V (3) are present for safety and isolation reasons. There are also present a DC/AC 24V-230V converter (4) for supply the Rogowski Coil integrator (5) and a DC/DC 24V±15 V converter (10) for the supply of LEM HOP transducers (11). The Compact Rio chassis (7) with the GPS module (8), and two acquisition modules (9), directly connected to Rogowski Coil (6), LEM HOP transducers and ULTRAVOLT transducers (12). After the installation, the measurement system was set for continuous acquisition and storage mode for about three month. All the transducers used in the campaign have been calibrated at INRiM laboratories under controlled environmental conditions (temperature of

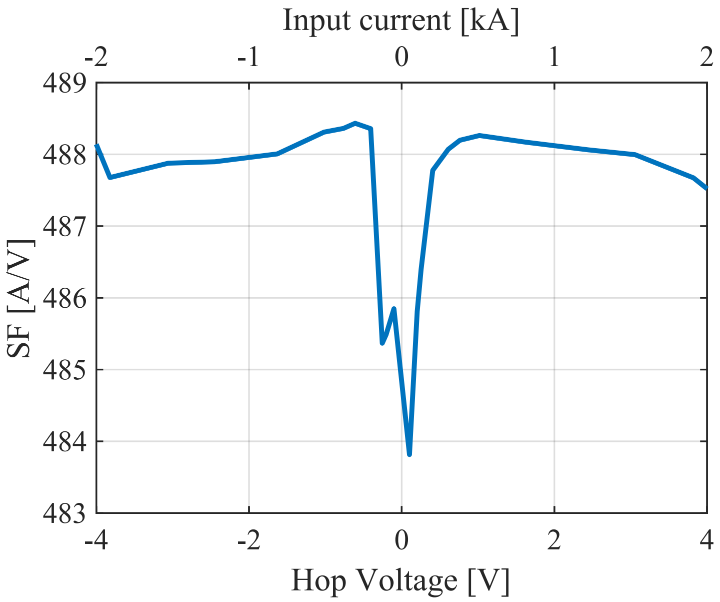

Fig. 2.7 Scale factor characterization of the LEM HOP 2000 transducer

23 ± 1 °C and the humidity in the [40 60] % range). All the voltage transducers and the transducer used for the current at pantograph have been characterized adopting DC national standards as reference. Instead, the performances of Rogowski coils have been tested using AC 50 Hz national standard; further test has been conducted also at the braking chopper frequency, 260 Hz.

As regards the three dividers, five steps in amplitude between 1 kV and 5 kV were performed; for each step, 31 iterations were implemented as prescribed by [22] in order to evaluate repeatability and stability correctly; finally, the type B uncertainty of the reference system (3 $\mu V/V$) was combined too. The transducers showed good amplitude linearity. In fact, the scale factor variability on the five different amplitudes is kept limited within the uncertainty (140 $\mu V/V$) interval; in other words, the measurement results at the different amplitude levels are compatible. For this reason, the scale factor can be considered constant with the amplitude in the range of interest.

Results coming from the calibration of the HOP 2000 current transducers are shown in Fig. 2.7. Twenty-four steps in amplitude, in the range -2 kA to 2 kA, with an analysis time of 1 s were performed. The technique adopted is explained in [23]. For each step, 31 iterations were implemented [22] in order to evaluate type A

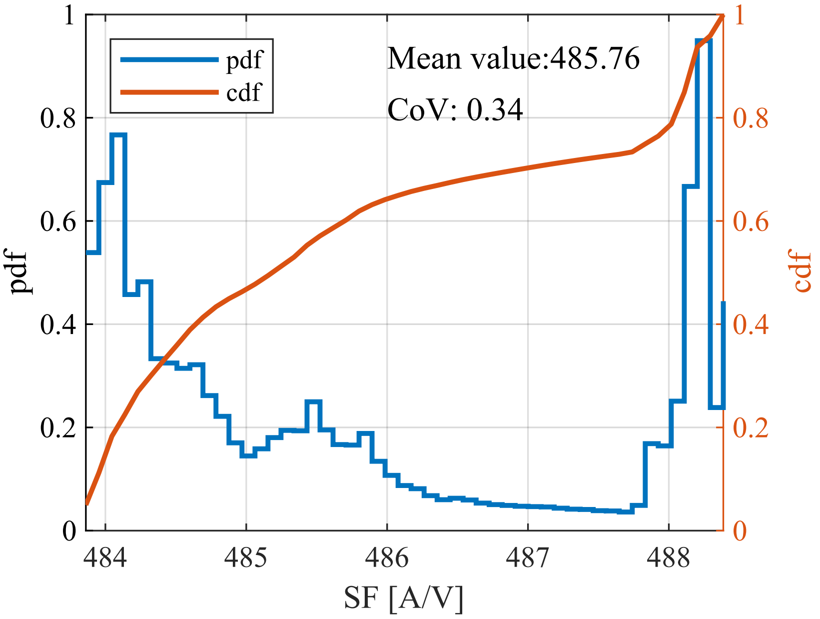

Fig. 2.8 Probability density function of SF

uncertainty correctly. The type B uncertainty for DC current setup is 150 $\mu A/A$ and was combined too. This sensor presents a linearity problem; in fact, it can be noted that the value of the scale factor (SF) significantly changes with the amplitude of the current. Thus the value of the SF can be written as a function of the transducer output voltage, $SF(v_{\mathrm{HOP}})$. In order to use a single SF value, and to estimate the impact of this linearity issue, a statistical analysis has been conducted, using all the v_{HOP} values coming from the measurement campaign averaged over 1 s. It can be assumed that SF is a random variable with the pdf (probability density function) shown in Fig. 2.8. The mean of the distribution can be used for all subsequent analyses to minimize the linearity issue impact on uncertainty. Moreover, it is possible to adopt the CoV (Coefficient of Variation) as a good estimation of the standard relative uncertainty contribution due to the non-linearity of the current measurements. In fact, according to the GUM Supplement 1 [24] the distributions of the input sources of uncertainty propagates through the model to provide the distribution of the output. Thus being $i_{\mathrm{P}} = SF \cdot v_{\mathrm{HOP}}$, and neglecting the contribution due to the voltage channel, the relative standard uncertainty on the current measurements coincides with that of the SF.

Moreover from the cdf (cumulative distribution function) it is possible to easily evaluate also the confidence level of such uncertainty for the real measurements dis-

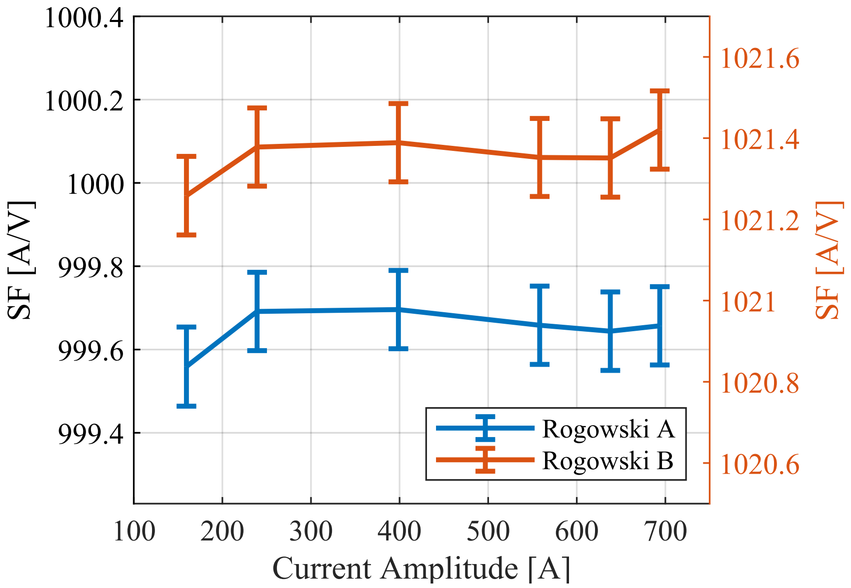

Fig. 2.9 Scale factor of Rogowski coil with expanded uncertainty ($k = 2$)

tribution (more than 92 % of the occurrence fall inside the interval 485.76 ± 0.5 %). Laboratory calibration was also performed for the Rogowski coils; the results are shown in Fig. 2.9. The error bars represent the expanded combined uncertainty at a confidence level of 95.45% ($k = 2$). As it can be seen, like the voltage dividers, the Rogowski exhibits a minimal variation of scale factor with amplitude. It can be considered almost constant in the range of interest, and the variation with amplitude was included in the uncertainty computation. Of course all active transducers have an offset, that has been opportunely compensated. Moreover experiments in laboratory has been conducted to take into account the temperature as influence factor. The variation of offset and gain with temperature was considered as source of uncertainty. It has been checked that the uncertainty contribution due to temperature variation in the range of measurement campaign maintains lower than the other sources, especially for HOP. For sake of brevity, not all the results coming from calibration of transducers, varying the amplitude and the temperature are reported. Table 2.2 summarizes the scale factor of each transducer adopted together with expanded combined uncertainty, with a confidence level of 95.45%($k = 2$).

Table 2.2 Sensors characteristics

Signal	**Scale Factor**	**U/M**	**Expanded Uncertainty in DC (k=2)**
v_{P}	1016.54569	[V/V]	0.014%
v_{F}	1016.85997	[V/V]	0.014%
v_{HF}	997.58296	[V/V]	0.014%
i_{P}	488.633	[A/V]	0.5%
i_{RA}	999.6509	[A/V]	0.03%
i_{RB}	1021.3581	[A/V]	0.03%

2.2.3 Power and energy computation

To measure the energy exchange by a train during the working condition, steady state of dynamic, the definition of the absorbed energy E_{A} on a time interval T has been applied:

$$E_{\text{A}} = \int_0^T P(t)dt = \int_0^T v(t) \cdot i(t)dt \tag{2.3}$$

where $P(t)$ is the instantaneous power, $v(t)$ and $i(t)$ are the generic voltage and current considered, and T is the time interval. To apply eq.(2.3) to the recorded data, a discretization is needed. Therefore:

$$E_{\text{A}} = \sum_{k=0}^{NT_C} v(kT_C) \cdot i(kT_C)dt \simeq \tag{2.4}$$

$$\simeq \sum_{k=0}^{N-1} v[k] \cdot i[k] \cdot T_C \tag{2.5}$$

where T_C is the sampling period, N is the number of sample in T, $v[k]$ and $i[k]$ the k-th samples acquired on voltage and current respectively. The overall energy is the sum of all the energy contributions, each of them is associated to one of the N sampling interval and obtained multiplying T_C by the k-th sample of voltage and current. In practice, it is useful to refer to the power associated to the k-th time interval as:

$$p[k] = v[k] \cdot i[k] \tag{2.6}$$

that is the values are the k-th sampled values of instantaneous power. Therefore, the total energy can be calculated by:

$$E_{\mathrm{A}} = T_C \sum_{k=0}^{N-1} p[k] \tag{2.7}$$

The power and energy obtained through eq. 2.7 and eq. 2.6 are negative when the locomotive is providing energy to the grid and are positive when is the grid that supplies the locomotive. This means that, appling these two equation on all the voltage and current samples of a whole journey, the net value of the energy absorbed is obtained. Nevertheless, it is very useful to evaluate separately the amount of energy, E_{D} , dissipated by the train for the traction and the auxiliary services and amount of energy, and the amount of energy E_{G}, generated by the train during braking and injected in the supply system in order to be re-used by another train. To this end, starting from eq. 2.6, it is defined the power dissipated in the k-th time interval p_{D}, simply considering only positive values of active power, thus:

$$p_{\mathrm{D}}[k] = \begin{cases} p[k] & \text{if } p[k] > 0, \\ 0 & \text{otherwise} \end{cases} \tag{2.8}$$

In the same way, to define the power recovered in the k-th time interval $p_{\mathrm{R}}[k]$, simply considering only negative values of active power, thus:

$$p_{\mathrm{R}}[k] = \begin{cases} -p[k] & \text{if } p[k] < 0, \\ 0 & \text{otherwise} \end{cases} \tag{2.9}$$

Therefore, the energy dissipated E_{D} and the recovered energy E_{R} during the time interval T can be calculated as:

$$E_{\mathrm{D}} = T_C \sum_{k=0}^{N-1} p_{\mathrm{D}}[k] \tag{2.10}$$

$$E_{\mathrm{R}} = T_C \sum_{k=0}^{N-1} p_{\mathrm{R}}[k] \tag{2.11}$$

The mathematical treatment until here was conducted referring to total power and energy absorbed by train but, hypothetically, the energy dissipated by the rheostats can been computed in the same way. In the next chapter, how this simplified approach can lead to a considerable error in the case of rheostatic braking will be illustrated.

2.2.4 Examples from the measurement campaign

In this Section, examples of data acquired in measurement campaign are provided. The following images are provided in order to clarify the energy exchange phenomena between the supply line and the train during a dynamic braking. The graphs reported in Fig. 2.10 represent the instantaneous powers, calculated as follows:

$$p_{\mathrm{P}}(t) = v_{\mathrm{P}}(t) \cdot i_{\mathrm{P}}(t) \tag{2.12}$$

$$p_{\mathrm{R}}(t) = (v_{\mathrm{F}}(t) - v_{\mathrm{HF}}(t)) \cdot i_{\mathrm{RA}}(t) + v_{\mathrm{HF}}(t) \cdot i_{\mathrm{RB}}(t) \tag{2.13}$$

$$p_{\mathrm{T}}(t) = p(t) - p_{\mathrm{R}}(t) \tag{2.14}$$

The behaviour of the voltage at pantograph, the power absorbed by the locomotive and the power wasted on rheostats in a particular braking along the Susa-Torino route are reported in Fig. 2.10(a). All the quantities in (2.12), (2.13), (2.14) are averaged over 100 *ms*. V_{TH}, represented with the dashed blue line, is the voltage threshold for the activation of chopper. At beginning the braking is totally regenerative, with the negative value of the absorbed power p_{p}. This means that the power is totally transferred to the line and, consequentially, the voltage v_{F} increases. After 2 seconds, V_{TH}, is reached and the chopper allows the dissipation, ($p_{\mathrm{R}} > 0$), wasting a fraction of the power provided by the inverters, p_{T}, on the rheostats. The dissipated share increases of the same amount, reaching a maximum of 1 MW around second 5. In the same time span, the traction power is almost 3 MW and the power injected by the train is almost 2 MW. Braking continues in a mixed scenario, between generation and dissipation, up to second 8, in which the voltage is below the threshold and the power is totally injected. Subsequently, the braking effort increases causing an increase in the line voltage with a consequent increase in dissipation.

As reported before, the chopper regulates the share of dissipated power changing the duty cycle value. This variation is shown in the enlargement provided in Fig. 2.10b and 2.10c.

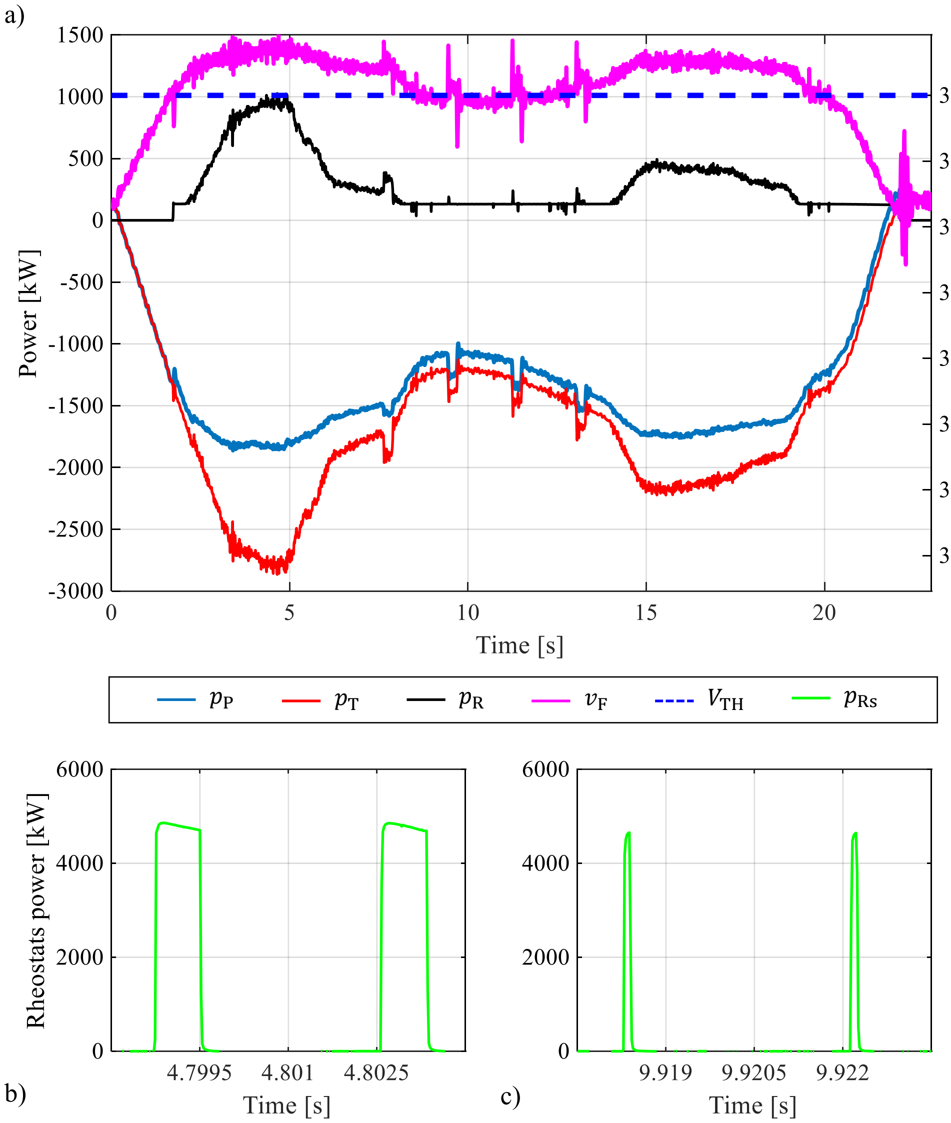

Fig. 2.10 Example of a mixed braking during Susa - Torino: (a) the powers averaged over 100 ms, (b, c) instantaneous rheostats power

Note that braking effort is at maximum, the dissipation is high and the duty cycle is about 20% (Fig. 2.10b). On the contrary, when the braking effort is at minimum, the duty cycle is only 4% (Fig. 2.10c), and the pantograph voltage drops below the V_{TH}. The power wasted on the rheostats is minimal so the power provided by the inverters is almost totally sent back to the supply line.

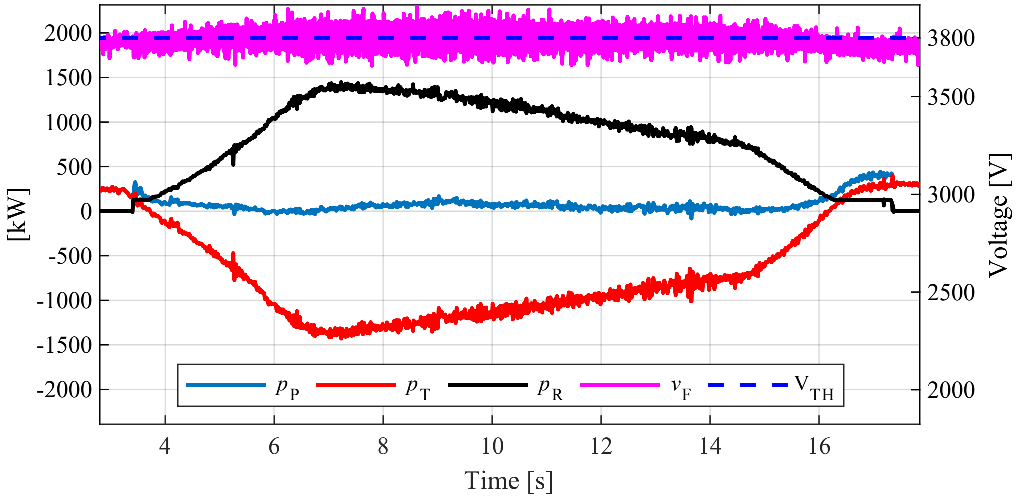

Fig. 2.11 Example of a dissipative braking during Novara - Domodossola

Fig. 2.11 provides an example of a purely dissipative braking. As soon as the traction power becomes negative, the voltage threshold is reached and the chopper starts working. For this reason, the power generated by the inverters, p_T, is completely delivered to the rheostats for dissipation. In facts, the p_T and p_R are symmetrical with respect to time axis, and p_p is always zero. The power provided by the inverters during this braking, starting from second 6, is about 1.3 MW for about 8 seconds. An energy of 2.89 kWh, recovered in 8 seconds, can potentially be used by other loads instead of being wasted.

2.2.5 Energy analyses

In Fig. 2.12 the behaviour in time of the instantaneous power absorbed by the locomotive along the Bardonecchia-Torino route is reported as an example of data analysed for a whole journey. This journey is characterized by an high difference in altitude between the stations of about 1000 m so the are very intense braking and acceleration events. Table 2.3 provides the absorbed energy compared with the recovered one obtained during the braking for different journeys. For each journey, the braking energy is fractioned into wasted and recovered energy. For most of the journeys, a remarkable percentage of the braking energy is wasted and not recovered. These figures depend on the capability of the DC supply system to receive such energy and obviously it changes in different days.

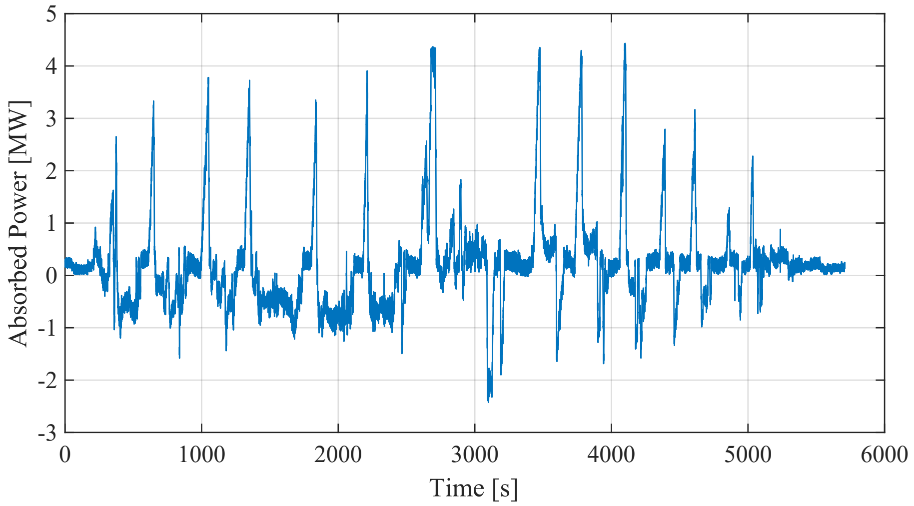

Fig. 2.12 Time behaviour of the instantaneous power along the route Bardonecchia – Torino

Table 2.3 Braking energy analysis on several journeys.

Railway route	**Absorbed Energy [kWh]**	**Braking Energy [%]**	**Wasted Energy [%]**	**Recovered Energy [%]**
Aqui Terme - Alessandria	282.5	23	20	3
Alessandria - Aqui terme	397.9	6	4	2
Alessandria - Savona	978.9	21	9	12
Savona - Alessandria	940.3	22	14	8
Alessandria - Voghera	372.4	15	6	9
Voghera - Alessandria	327.7	23	5	18
Novara - Domodossola	982.9	15	9	6
Domodossola - Novara	837.5	19	14	5
Mortara - Novara	201.0	10	5	5
Novara - Mortara	231.6	24	12	12
Novara - Domodossola	962.0	17	17	0
Domodossola - Novara	843.7	15	11	4
Bardonecchia - Torino	302.4	150	50	100
Torino - Bardonecchia	1580.8	8	1	7

2.3 Metro de Madrid measurement campaign

European energy strategy urges the rail line partners to embrace technological answers to decrease the rail line transport ecological footprint by 50% by 2030. In DC frameworks, the traditional substations permit just a unidirectional energy flow (from the electrical grid to the trains) so the recovered energy, when injected on the catenary, can be just reused by other adjacent trains that need energy simultaneously. When this is not possible, the recovered energy must be dissipated on board by dedicated rheostats in order to limit the voltage increase up to unacceptable levels [25, 14, 26]. Consequently, just a share of energy is recovered and an impressive one is wasted. The volume of recovered energy depends by few elements such the quantity of braking occasions, the effort of each braking, the amount of trains operating on the line, etc.

The adoption of energy storage devices is an example of solutions used to increase the energy saving from braking. Since braking is characterized by a high power density in a short time, supercapacitors can represent a winning choice to implement the strategy of energy storage along the line. The issue with supercapacitor is the room requirements for their installation and devoted power converters to regulate the system voltage to the storage voltage and to manage with the re-utilization of energy inside a brief time frame, to prevent self-discharge and preserve the high efficiency, [27]. One more answer for exploiting the most significant part of the energy delivered by braking is the timetable optimization.

In literature, various models intend to coordinate the start, stop and coasting phases of the trains on the same line to synchronize the braking with the traction phases [7, 28–35].

One of the main and most promising solution implemented is the adoption of RSSs, used to reinject the energy recovered by the dynamic braking into the supply grid [36]. Currently, this innovation is considerably more diffused in metro and tram frameworks than the rail one, since the power requirements of this type of substations make easier the design and the implementation of the RSS.

Numerical simulations give exciting information on the amount of energy that is wasted in rail systems; results show that the traction energy can be wasted up to 40% [28]. Instead, a real measurement campaign on board an Italian locomotive for railway commuter service provides wasted energy of up to 20% [37].

Many more RSSs are introduced in metro and railway systems these days. However, most of the data on the impact of installing an RSS provided in the scientific literature are based on simulations. With the experiences made during the project and this thesis work, our research team tends to fill a lack of valid and reliable data, obtained in measurement campaigns made on prototypes and devices currently in use, providing information on energy saving in different operating conditions and introducing an approach to quantify it. An impact ranging between 15% and 20% for the computed energy efficiency impact of RSS are quite common. Fascinating information are gathered by the review work published by Douglas & al. [28].

The single RSS installed in the Bilbao metro shown energy savings which surpassed predicted results. In this case, the single prototype installed on high traffic section reduced annual substation consumptions by 11.3% when originally savings of only 8.3% were theorized [7, 28–35, 37, 38, 15, 39]. To expand the scientific literature on the RSS innovation in real test cases, this section shows the results of a measurement campaign conducted on a train working on the metro line that serves the city of Madrid, where a reversible substation was introduced.

2.3.1 Train under analysis

The train considered for the measurement campaign is a subway train with three cars, model S9000 3 CARS SS3, whose main mechanical characteristics are reported in Table 2.4.

Table 2.4 Main characteristics of S9000 train

Parameter	Value
Total length	54 m
CarM length	18.55 m
CarR length	17.8 m
Axle	12
Rated supply voltage	1500 V
Total power	8x187 kW
Maximum car height	3.878 m
Car width	2.808
Total weight	95 Mg
Maximum speed	110 km/h

The considered train is composed by two identical traction units, supplied by independent pantographs. The operating line voltage is 1.5 kV and the maximum power absorption is 2.5 MW. Considering that the traction effort is balanced between two cars and, since they work in practically the same conditions, only one of these two has been equipped with the measurement setup. All considerations and results discussed from now on will refer to a single traction unit. It follows that, in order to obtain the values of current, power and energy exchanged by the entire train, it is necessary to scale these two quantities by a factor of 2. Obviously, the same argument does not apply for the voltage which is the same for both cars.

The simplified scheme of the input stage of the monitored car is provided in Fig. 2.13. As expected, the power drawn from the grid is largely dissipated by the traction effort but another not negligible share is used to power auxiliary loads such as air conditioning, ventilation, lighting, carriages, etc. As provided in Fig. 2.13, the inductance L_{F} and the capacitor bank C_{F} compose an input stage second order filter on the traction branch. This filter has a double function: limiting the frequency content of the voltage imposed on the inverters that regulate traction and filtering the noise produced by the inverters during the braking phase, i.e. when the power is supplied by the train to the line.

As described in Chapter 1, if it is not possible to transfer the energy recovered during braking to another train in the dissipation phase, this must be dissipated on board by the braking rheostats. The average current values on the rheostats, indicated in the figure with i_{RA} and i_{RB} are managed through a chopper regulated with PWM modulation. For the train in question, the modulation frequency is 300 Hz, with a duty cycle that can vary between 2% and 50%, and the rated current value is 600 A. It is helpful to remember that the higher the duty cycle, the more energy is wasted on the rheostats. For this reason, the chopper has the fundamental role of sorting the energy recovered by the inverter between the power line and the rheostats and the control variable for this process is v_{F}. When the latter is higher than a certain threshold, in the specific case of 1.7 kV (value found experimentally), the chopper begins to operate, trying to counteract an intolerable increase in the voltage level. For voltage values above 1.8 kV, the energy is completely injected into the braking resistors.

We can say that the traction scheme of the S9000 metropolitan train shown in Fig. 2.13 and that of the E464 train shown in Fig. 2.4 are almost the same; the main

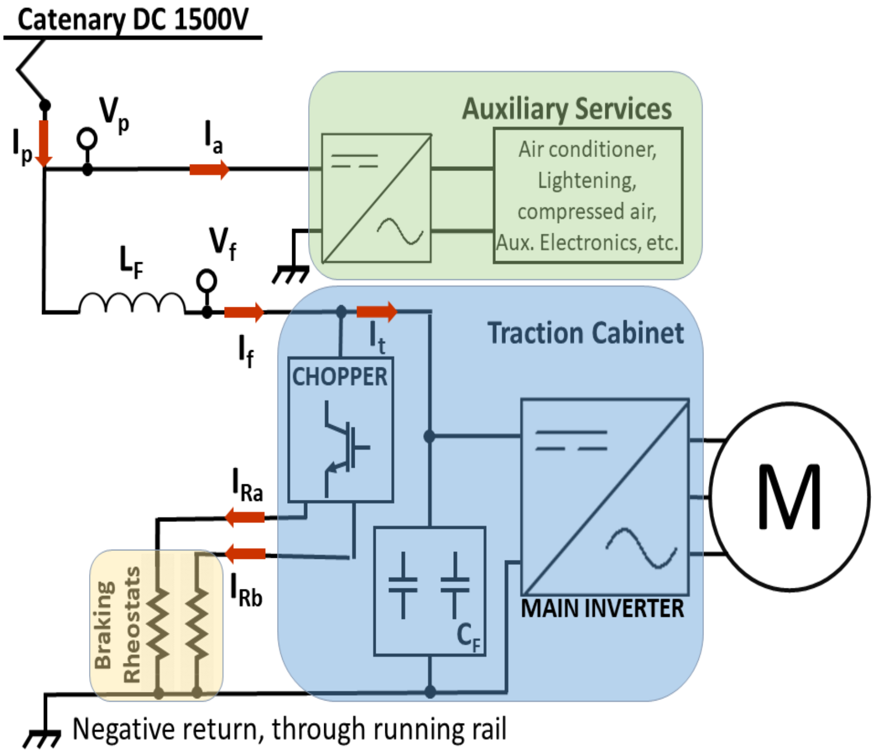

Fig. 2.13 Input stage scheme of S9000 metro train

difference consists in the line voltage reduced by 50%. Still, no inverter or rheostat operates with a common mode voltage other than zero.

2.3.2 The subway line

The subway line under analysis is the one that goes from Hospital Infanta Sofia to Tres Olivos. It is powered by five substations: Tres Olivos, Las Tablas, La Moraleja, Baunatal and Hospital Infanta Sofia. It is composed of 11 stations for 15 km, travelled in about 47 minutes. This line was selected because one of the five substations, La Moraleja (in red in Fig. 2.14), is characterized by the presence of a 2 MVA DC/AC converter for injection into the grid of energy recovered from braking.

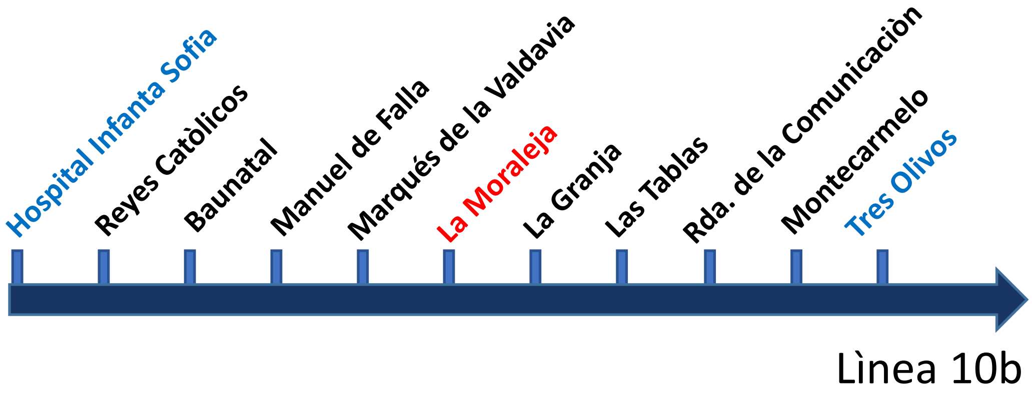

Fig. 2.14 Line 10B - Metro de Madrid

As schematized in Fig. 2.15, to increase the efficiency of the overall system avoiding waste, the goal of Metro de Madrid is to reuse energy to power all the loads of the substation (elevators, escalators, air conditioning system) and to return any surplus to the grid.

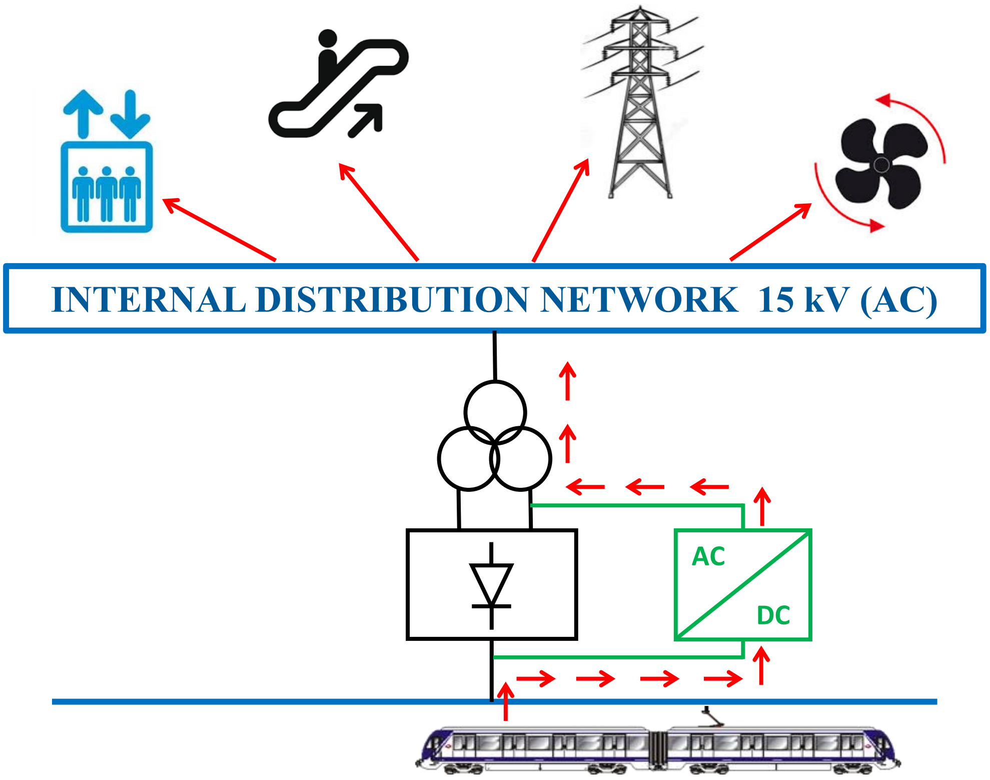

Fig. 2.15 Power flow during a braking in presence of a RSS

It is essential to underline that at the time of the measurement campaign, the substation recovery capacity was reduced by the lack of possibility of re-feeding the power into the grid due to legal constraints. For this reason, the results reported below refer to a partial impact that the use of a reversible substation can have in a metropolitan system. The recovered energy is exclusively the one used for loads of the substation. However, it is interesting to evaluate the performance in this condition, even if the impact of this installation can only improve when the limitation will be removed.

2.3.3 Measured quantities

In Fig. 2.13 the quantities measured to analyse the power flows in all operating conditions are shown. These are:

- voltage at pantograph, v_P

- current at pantograph, i_P
- filter voltage, also applied to the rheostats, v_F
- current provided to the auxiliary system, i_A
- currents flowing into the braking rheostats, i_RA and i_RB.

Due to installation issues, the traction current i_T shown in Fig. 2.13, that represents the current supplied to the inverter, is not measured through any sensor but it is indirectly determined. The knowledge of this quantity is fundamental because it allows the measurement of the power absorbed during the traction effort and allows the measurement of the power generated during the braking phase. In addition to the accurate measurement of the energy exchanged between trains and power lines, these measurement campaigns had as their objective the analysis of fast PQ phenomena, such as electric arcs [40], that require very high performance from the measurement setup. The measurement system developed for this campaign (shown in Fig. 2.16) allows for recording the two voltages and five currents mentioned above with a high resolution and high sampling frequency to carry out analyzes on signals with a wide bandwidth.

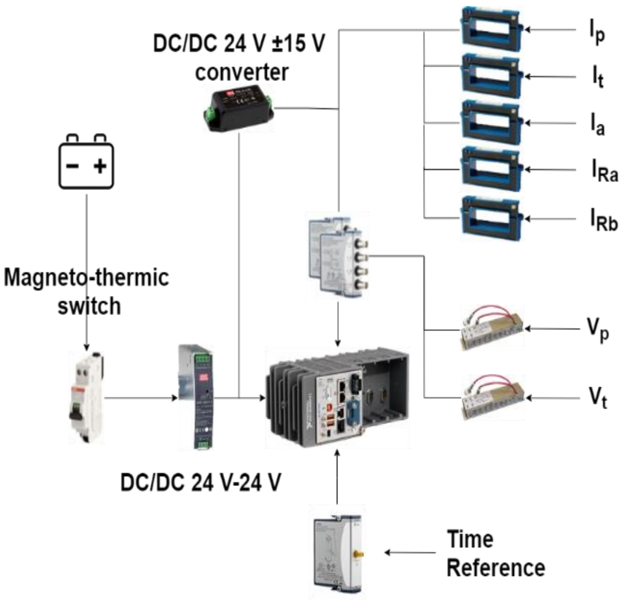

Fig. 2.16 Measurement setup installed on Metro de Madrid train, S9000

The acquisition system is referenced to absolute time via the GPS module NI 9467, that provides a PPS signal with an accuracy of 100 ns. Obviously, the GPS receiver cannot work well underground, but the train passes in an open sky track at least once a day, the system can synchronize with UTC in that moment and then it keeps time using internal real time clock until next synchronization. Two Ultravolt 40TF-CDCD (40 kV/40 V 0 Hz ÷ 1 MHz, 0.25%) resistive-capacitive compensated dividers have been adopted to scale down the voltages v_{P}, and v_{F} which nominal amplitude is 1500 V. Open loop Hall effect current transformers have been used for the currents. They have openable magnetic core, that facilitate the installation. Two different models have been used, the HOP 2000 and the HOP 800 from LEM with 2000 A and 800 A of primary nominal current respectively.

The former has been used for i_{P} and i_{F}, whose amplitudes can reach 1000 A. The latter instead is used for i_{A}, i_{RA} and i_{RB} as they reach significantly lower amplitudes (600 A for i_{RA} and i_{RB}, less than one hundred of ampere for i_{A}). Both models feature an accuracy better than 2% and a flat frequency response from DC to 10 kHz. The measurement system and the transducers are battery powered in order to allow a continuous monitoring of the train signals, even when the pantograph is not in contact with the catenary. The data acquisition system has been located in the low voltage cabinet. The voltage divider related to the pantograph voltage measurement and the current transducer related to the auxiliary service current have been installed in the high voltage cabinet. The other transducers are located under the train in proximity of the traction cabinet. All the transducers adopted have been metrologically characterized at INRIM laboratories to guarantee traceability. The a detailed calibration description is provided in section 2.2.2.

2.3.4 DC Energy flows computation

The analysis of the DC power and energy flows are obtained applying the Kirchhoff's current law to the circuit shown in Fig. 2.13.

$$i_{\mathrm{P}} = i_{\mathrm{A}} + i_{\mathrm{F}} \tag{2.15}$$

$$i_{\mathrm{F}} = i_{\mathrm{R}} + i_{\mathrm{T}} \tag{2.16}$$

where i_{R} is the current that flows in both the rheostats:

$$i_{\mathrm{R}} = i_{\mathrm{RA}} + i_{\mathrm{RB}} \tag{2.17}$$

while i_T is obtained as:

$$i_\mathrm{T} = i_\mathrm{F} - i_\mathrm{R} \tag{2.18}$$

Based on the provided equations, the overall balance of the energies is the following:

$$E_\mathrm{P} = E_\mathrm{A} + E_\mathrm{T} + E_\mathrm{L} + E_\mathrm{D} \tag{2.19}$$

where E_P is the energy absorbed at pantograph, E_A is the energy absorbed by the auxiliary systems, E_T is the energy absorbed by traction system and E_L is the energy dissipated by the input filter, E_D is the energy dissipated by the braking rheostats. Each of these quantities is presented in the following equations:

$$E_\mathrm{P} = \int_{t_1}^{t_2} v_\mathrm{P}(t) \cdot i_\mathrm{P}(t) \cdot dt \tag{2.20}$$

$$E_\mathrm{A} = \int_{t_1}^{t_2} v_\mathrm{P}(t) \cdot i_\mathrm{A}(t) \cdot dt \tag{2.21}$$

$$E_\mathrm{L} = \int_{t_1}^{t_2} (v_\mathrm{P}(t) - v_\mathrm{F}(t)) \cdot i_\mathrm{F}(t) \cdot dt \tag{2.22}$$

$$E_\mathrm{T} = \int_{t_1}^{t_2} v_\mathrm{F}(t) \cdot (i_\mathrm{F}(t) - i_\mathrm{R}(t)) \cdot dt \tag{2.23}$$

$$E_\mathrm{D} = \int_{t_1}^{t_2} v_\mathrm{F}(t) \cdot (i_\mathrm{RA}(t) + i_\mathrm{RB}(t)) \cdot dt \tag{2.24}$$

where t_1 and t_2 are the beginning and the end of the considered time interval (2.20-2.24). During traction, coasting and stop phases ($i_\mathrm{T} \geq 0$) i_R (so E_R) is equal to zero because the rheostats are not involved in any operation. E_A plays a marginal role; typically the energy absorption is constant and in most of the cases is negligible with respect to E_T. The same goes for E_L; it is always a small percentage of E_T. As explained in Chapter 1, the motors generates energy during the braking stage; from the electrical point of view, this means that i_T becomes negative, so does E_T. It can be helpful define the braking energy as follows:

$$E_\mathrm{BR} = -E_\mathrm{T} \tag{2.25}$$

and the energy re-injected to the grid as:

$$E_\mathrm{IN} = -E_\mathrm{P} \tag{2.26}$$

Considering eq. 2.25 and eq. 2.26, eq. 2.19 can be written as;

$$E_{\mathrm{BR}} = E_{\mathrm{A}} + E_{\mathrm{L}} + E_{\mathrm{D}} + E_{\mathrm{IN}} \tag{2.27}$$

During a regenerative or mixed braking, E_{BR} is recovered by the auxiliary systems on-board train; any surplus of energy can be injected (E_{IN}) in the supply system if there are some other loads nearby able to use this energy at that very moment. In the absence of other trains in the traction phase or other loads, the injection of energy causes an increase in the line voltage at the point of contact with the pantograph. To prevent this voltage increase from reaching levels that jeopardize the safety of the system, the control system on board the train increases the amount of energy dissipated (E_{D}), consequently lowering the amount of the one injected into the grid E_{IN}. This means that the amount of energy recovered indeed relies on the availability of the line to receive it. The latter is a phenomenon with no univocal quantification in literature but is known as the "receptivity" of the line. The goal of installing an RSS is to improve receptivity. In the paper [3], the authors propose a parameter, L_{u} that is the Line Unavailability seen from the point of view of the train. It is defined as:

$$L_{\mathrm{u}} = 100 \cdot \left(\frac{E_{\mathrm{D}}}{E_{\mathrm{BR}}} \right) \tag{2.28}$$

This parameter can be used as an index of the unavailability of the line in absorbing energy, considering that the greater the L_{u} is, the lower the receptivity is. Obviously, L_{u} is not constant over time; it is therefore interesting to analyze this parameter as a function of the braking time t_{BR}, that means by evaluating it through the average braking power ($\bar{\mathrm{P}}_{\mathrm{BR}}$) and the average power dissipated ($\bar{\mathrm{P}}_{\mathrm{D}}$) calculate as follows:

$$\bar{P}_{\mathrm{D}} = \frac{E_{\mathrm{D}}}{t_{\mathrm{BR}}} \tag{2.29}$$

$$\bar{P}_{\mathrm{BR}} = \frac{E_{\mathrm{BR}}}{t_{\mathrm{BR}}} \tag{2.30}$$

and thus eq. (2.28) can be rewritten as

$$L_{\mathrm{u}} = 100 \cdot \left(\frac{\bar{P}_{\mathrm{D}}}{\bar{P}_{\mathrm{BR}}} \right) \tag{2.31}$$

Therefore, L_{u} is not dependent to the duration of braking.

As previously reported, the effect of installing an RSS must improve the efficiency of the system by causing a sharp decrease in the L_u parameter. To analyze this change, we need to consider a statistic of L_u, representative of all the working conditions, with the RSS running, and compare it with the statistic representative of the value of L_u when RSS is not running.

2.3.5 Experimental results of Metro Madrid campaign

Since October 2019, a measurement campaign has been performed for 18 days by monitoring, in a continuative way, a train operating only on the line 10B covering in a repetitive and comprehensive way all the working conditions of the line in terms of traffic density and time slots. Information about 350 roundtrip journeys have been acquired and over 500 GB of data have been stored. Almost in half of the monitored time the RSS was active, while in the other half it was not operating (121 and 111 working hours respectively). In both the situations all the working conditions are covered in a similar way, so statistical analyses can be performed obtaining comparable results.

In Fig. 2.17 the traction current obtained by eq. (2.18) is reported as example of a typical journey form Hospital Infanta Sofia to Tres Olivos.The time intervals corresponding to the ten movements of the train between consecutive stations (subtracks) are highlighted: it is possible to recognize the acceleration stages leaving from the stations (big positive current spikes) and the braking stages approaching to the next stations (big negative current spikes). After the braking, the train stops (I_T goes almost to zero) for a while in each station before leaving again.

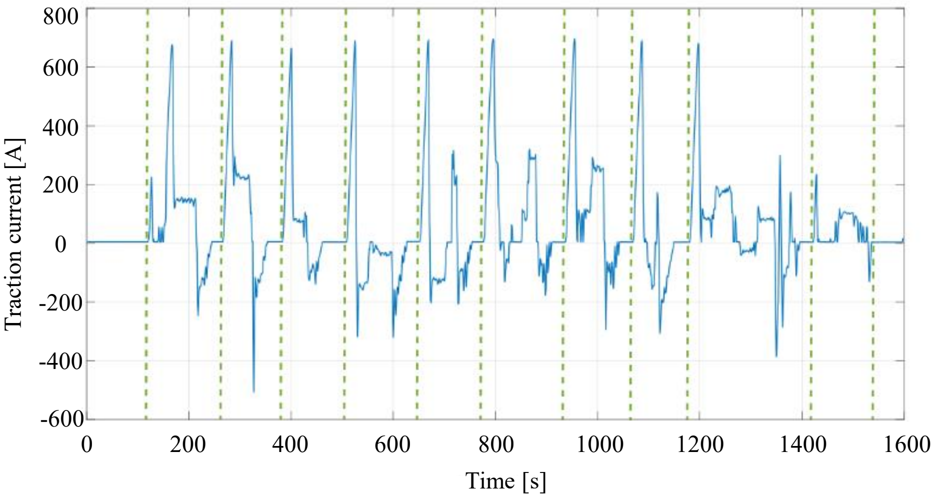

Fig. 2.17 Traction current (i_T) during a one-way trip.

The movement of the train was not always regular and sometimes the train driver had to brake before approaching the station, probably either approaching a bend or, alternatively, due to the presence of another train that had not yet left the next station (see Fig. 2.17 sub-track 4 – 8, starting from the first green dashed line). In the last part there is a speed limitation that consequently limits the current absorption.

The train tries to inject energy in the supply system during all the braking events but as previously described, the energy actually fed in the catenary firstly depends on the presence of a contemporary absorption (traction) of some other trains that are nearby. If this favourable condition does not occur, the regenerated energy should be transferred to the RSS. When the supply line has not the capability to absorb all the generated energy, the excess part must be dissipated on-board the train by the rheostats. This depends on the state of the other trains (e. g. other regenerative braking at the same time) or from the general dynamic state of the supply line (e.g. distance from regenerative substation or distance from other trains). The lack of receptivity of the supply line was detected by an excessive increment of the feeder voltage that triggers the on-board dissipation.

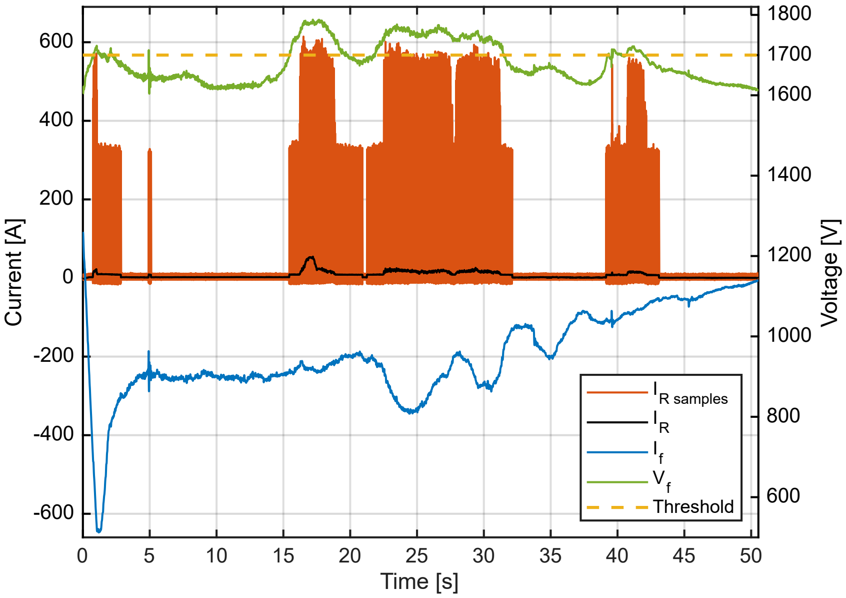

Fig. 2.18 Main signals during the most regenerative braking.

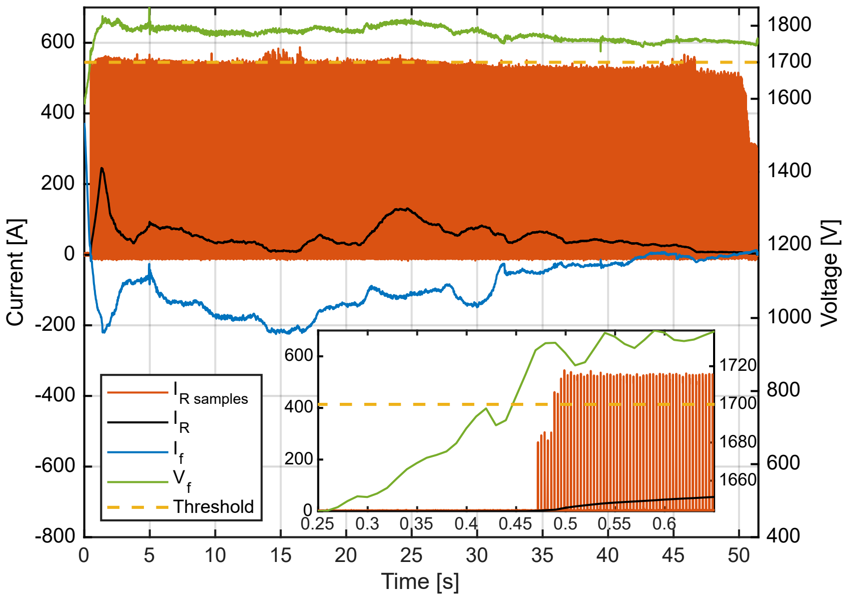

Fig. 2.19 Main signals during the most dissipative braking.

About 6951 braking events were identified and analysed; Fig. 2.18 and Fig. 2.19 report two examples of braking events to show the time evolution of the main electrical signals involved. These two events, even if with similar duration, are very different form an energetic point of view: the first one is the most regenerative, while the second one is the most dissipative among that provided by the measurement campaign.

The reported values are averaged over $\Delta t = 10$ ms that is enough for dynamic of almost all signals, except for i_{R} that, as previously stated, is a chopped current at 300 Hz. Therefore, for this signal, both the current sampled at 50 kHz and its average value over 10 ms are reported (red and black line respectively). Both figures confirm the expected control system behaviour: when (v_{F} overcomes the threshold of 1700 V (dotted yellow line), the chopper starts the dissipation in the braking rheostats (i_{R} samples $\neq 0$, red line). It can be noticed that, even if the peak levels of current are nearly constant (i_{R} samples red line), the average value of i_{R} (black line) is not constant, because it depends on the duty-cycle of the chopper. This is not appreciable with instantaneous values graph. The black line shows how the amount of energy changes in agreement with braking effort and line receptivity.

Fig. 2.18 provides an intense braking (E_{BR} = 5.11 kWh) in which the energy has been almost all injected (E_{IN} = 4.60 kWh). In fact, i_{F} always assumes negative and large values while i_{R} always maintains low values (less than 20 A). So that only a small amount of energy is dissipated on board while most of the energy is injected into the line. The details about this event, including the amounts of involved energies, are reported in the first row of Table 2.5 where the information about the four braking events with the highest amount of E_{IN} are reported. Fig. 2.19 reports a braking with medium effort (E_{BR} = 3.17 kWh) in which the energy has been almost all dissipated on-board (E_{D}= 2.53 kWh). Please note that just after the start of braking (at second 0.4) v_{F} exceeds the threshold and it keeps over that level till the end of the event.

i_{R} assumes large values peak value of 250 A) while i_{F} always maintains low values (peak value of -220 A). This is the consequence of a low line receptivity, maybe due to the simultaneous braking of another train. The details about this event including the amounts of involved energies are reported in the first row of Table 2.5 where the information about the four brakings with the highest amount of E_{IN} are provided.

Some considerations can be done comparing Table 2.5 and Table 2.6. Firstly, it can be noticed that for all the cases of high reinjected energy, the RSS is active. On the other hand, all the most dissipative braking events happen when the reversible part is switched off, coherently with what can be expected. Moreover, looking at the

Table 2.5 The most regenerative braking events of the campaign.

Date	**Time**	**Duration [s]**	**Reversible Substation**	**Circulating trains**	**E_{IN} [kWh]**
7-oct	18:57	50	ON	11	4.55
11-oct	11:13	50	ON	9	4.55
15-oct	06:23	50	ON	6	4.60
15-oct	06:36	87	ON	8	4.59

Table 2.6 The most dissipative braking events of the campaign.

Date	**Time**	**Duration [s]**	**Reversible Substation**	**Circulating trains**	**E_{IN} [kWh]**
19-oct	07:54	37	OFF	7	2.17
19-oct	12:07	40	OFF	7	1.99
21-oct	01:09	50	OFF	3	2.24
21-oct	01:56	50	OFF	3	2.53

5th column of Table 2.6, the most regenerative braking events occur when there is a bigger number of trains with respect to those in Table 2.5. As expected, the line receptivity is not constant and can be related to the number of trains simultaneously present on the line, but the presence of the reversible part impacts as well. In fact, one of the most regenerative events occurs with only 6 trains (second row of Table 2.6); obviously, it could not only be due to the RSS, because there is a not negligible probability to have at least one of the other five trains accelerating simultaneously. A complete evaluation of the RSS impact cannot be performed by analysing single events. Only the statistical approach, described in the following, provides significant results.

2.3.6 Line receptivity analysis

As already stated before, the train was monitored with the RSS that, in the first half of time, is active, and in the other half is not operating. In the following, for sake of brevity the first condition will be referred as Reversible substation and the second as Conventional substation. In both the situations all the working conditions of the train are covered in a similar way, so statistical analyses carried out in the two periods provide comparable results. One of the advantages expected by the adoption

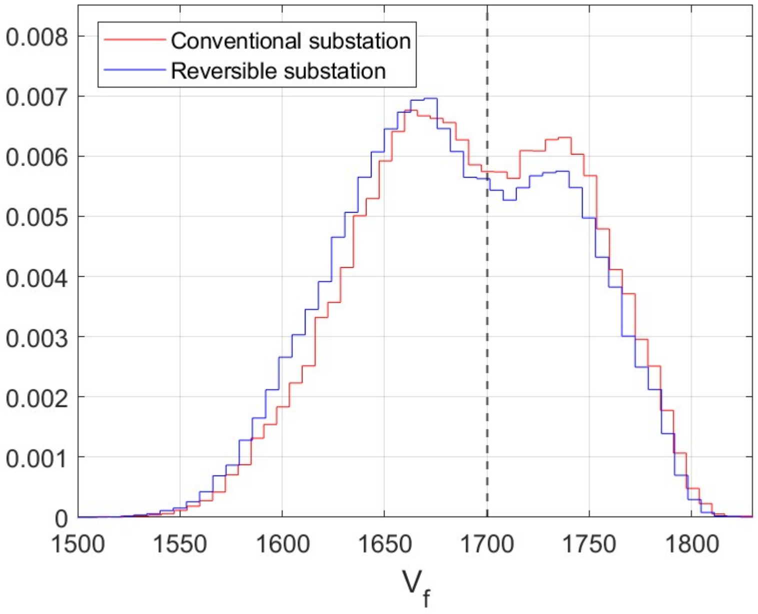

Fig. 2.20 Statistical analysis of the pantograph voltage by considering conventional and reversible substation.

of a RSSs is a more stable supply voltage [41]. To analyse this aspect, Fig. 2.20 provides a comparison of the different statistical distributions of v_F , obtained with conventional and reversible substation. This parameter was chosen, in place of v_P, because, as mentioned before, it is the control variable that manages the amount of dissipated energy in the on-board rheostats. More in details, two Probability Density Functions (pdf) are obtained considering the average voltage level during each braking event.

The two distributions shown in Fig. 2.20 have a bimodal behaviour with intersection in correspondence of the chopper intervention threshold (see black dashed line). There are very similar, and the expected improvement is not so evident. This could be due to several reasons: the limited amount of the power injectable in AC side, the presence of only one RSS over 5 substations, that entails a higher average distance between train and RSS, and the high level of the supply voltage that is really near to the threshold level of the braking chopper. Nevertheless, some improvement in voltage stability can be noted: there is a reduction of the mean value (from 1690 V to 1682 V) and of the 95th percentile value (from 1771 V to 1767 V). In practice, the presence of the RSS limits the occurrences of voltage level over 1700 V. Anyway,

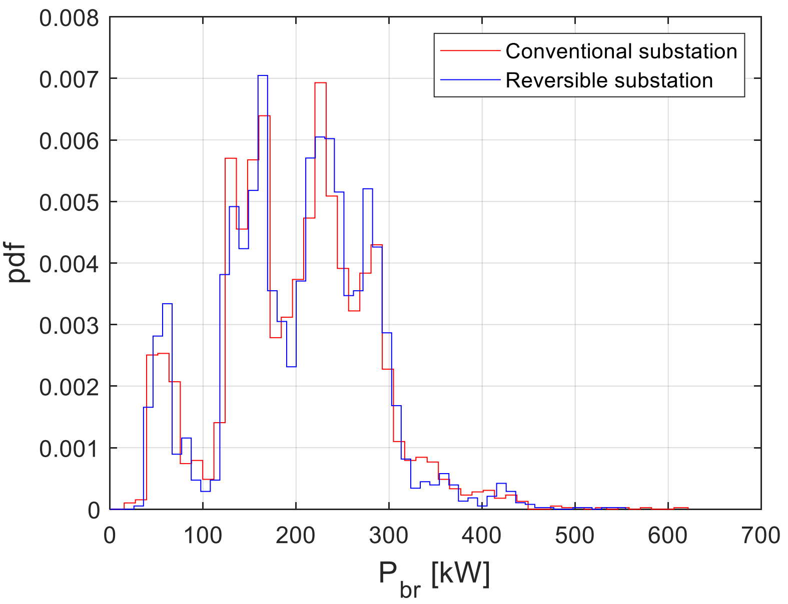

Fig. 2.21 Comparison of statistical analyses of braking power.

the similarity of the two distributions confirms the comparable working conditions of the two considered situations.

An important role in the energy recovery is played by the effective amount of the braking power. As previously said, this parameter is expected to be practically constant in the considered two supply conditions since it is not dependent on the presence of RSS. Furthermore, the presence of Automatic Train Operation (ATO) leads to expect a repetitive behaviour during braking. In fact, Fig. 2.21 provides a comparison of the different statistical distributions of P_{D} measured during the braking events, with conventional and reversible substation: the two pdfs almost completely overlap. The pdf shows three picks at 56 kW, 160 kW and 230 kW that represent the most common braking power efforts. The impact of the RSS is evaluated by some statistical analysis of L_{u}, the line unavailability to receive energy.

The measured values of L_{u} are analyzed by the pdf and the Cumulative Distribution Function (cdf) and by some synthetic indexes such as average, standard deviation and 95th percentile.

The first analyses have been conducted over all the working hours, considering separately all the braking events recorded when the RSS is ON (Fig. 2.22a) and OFF (Fig. 2.22b).The two distributions have a very similar behaviour but the presence of

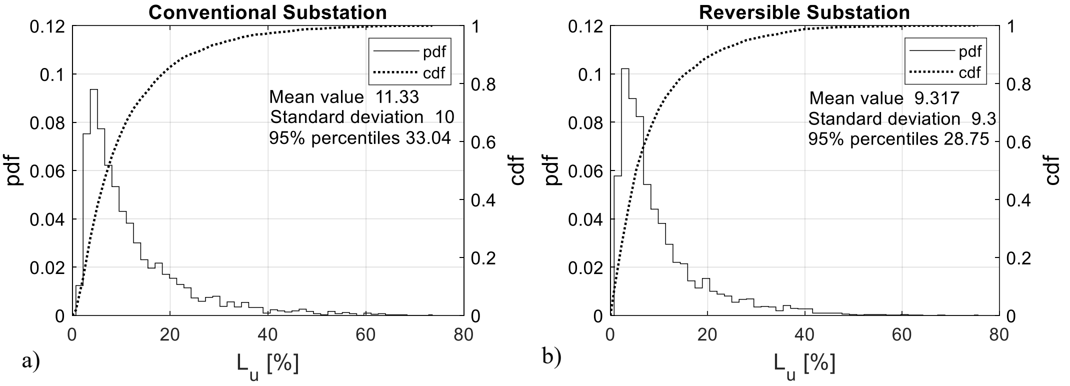

a) b)

Fig. 2.22 Line unavailability statistic by considering conventional substation (a) and RSS (b).

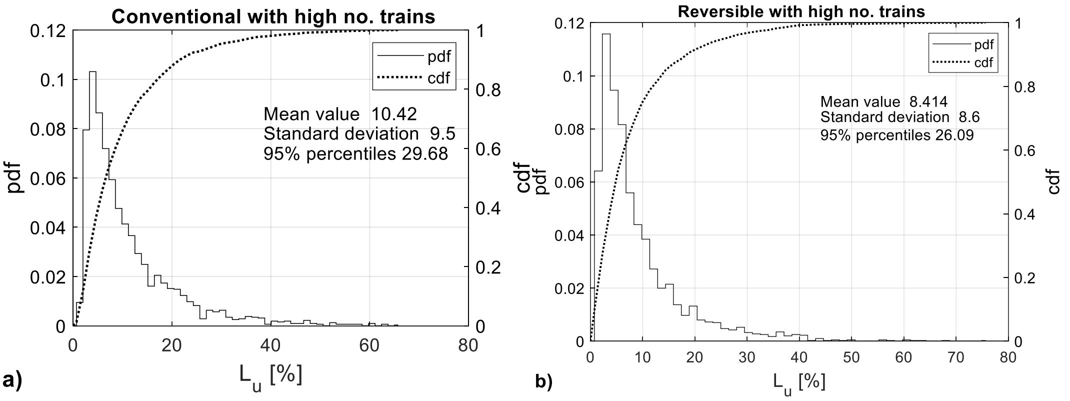

a) **b)**

Fig. 2.23 Line unavailability statistic with high number of trains ($\geq$9) by considering conventional substation (a) and RSS (b).

RSS produces a significant reduction of the synthetic statistical parameters associated with L_u. In particular, the average is reduced by about 20% and 95th percentile and standard deviation are reduced by about 10%.

To show how the different traffic conditions affect L_u, the same statistical analyses of Fig. 2.22 were performed over the braking events that occur in specific hours. In fact, using the timetable of Metro de Madrid it has been possible to know, at the different hours of each day, the number of trains that are contemporary in service. Therefore, comparative analyses were again performed but considering separately the braking events that happen in the time slots with high traffic (number of circulating trains $\geq$ 9) and with low traffic (number of circulating trains $\leq$ 3). The results are reported in Fig. 2.23 and Fig. 2.24, respectively. The shapes of distributions in Fig. 2.23 are very similar to those in Fig. 2.22 and the most probable values are those with low L_u amplitude (in both cases the 95th percentiles are about 30% and the

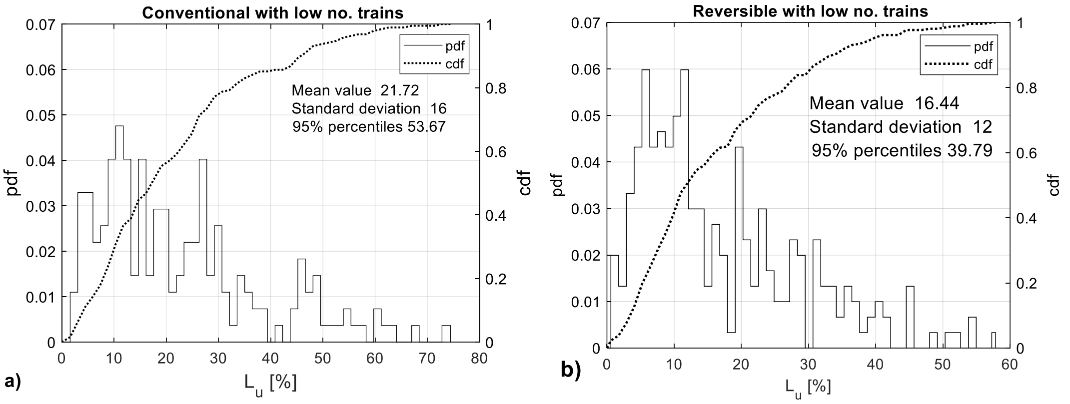

Fig. 2.24 Line unavailability statistic with low number ($\leq$3) of trains by considering conventional substation (a) and RSS (b).

most probable values are close to 5%). More different are the distributions shown in Fig. 2.24: Higher amplitudes of L_u are more probable (the 95th percentiles are over 40% with a more uniform distribution). This is an expected behaviour because the number of trains directly impacts on L_u: the greater the number of trains, the greater the receptivity of the line.

The presence of RSS in both situations (compare Fig. 2.23a with Fig. 2.23b and Fig. 2.24a with Fig. 2.24b) increases the probability to have lower values of L_u and, in fact, all synthetic indexes sensibly reduce their value. With high receptivity (Fig. 2.23 a and b) the difference between conventional and reversible is about 2% for the mean value and 3.6% for the 95th percentile, that is almost aligned with the results in Fig. 2.22.

With low receptivity (Fig. 2.24a and b) the difference between conventional and reversible is more remarked, it reaches about 5.3% for the mean value and 13.9% for the 95th percentile. It is interesting to note that with lower circulating trains (see Fig. 2.24), the effect of the RSS is more evident: the synthetic indexes reduction is much greater than in Fig. 2.23 and the shape of distribution in Fig. 2.24b becomes more similar to those in Fig. 2.22 and Fig. 2.23. This occurs because with a low number of trains during braking there is less chance that another train is accelerating at the same time and absorb the regenerated energy; therefore, energy recovery is much more reliant on RSS. To quantify with absolute values the impact of the RSS in the same situations considered in Fig. 2.22, Fig. 2.23 and Fig. 2.24, in Table 2.7

the corresponding average values of E_D are reported (first second and third column, respectively).

Table 2.7 Analysis of the Dissipated Energy.

Traffic conditions	**All**	**Train n.$\geq$ 9**	**Train n.$\leq$ 3**
Average E_D [kWh] Conventional	202	183	427
Average E_D [kWh] Reversible	159	145	296
Relative increment [%]	21.4	20.9	30.7

As it can be noticed from the first column, the presence of the RSS allows a reduction of 21.4% of the on-board dissipation (passing from 202 kWh to 159 kWh).

Nearly the same behavior was found with high number of trains (compare the first and the second column), because the line receptivity is kept high by the presence of many trains and the RSS has only a minor impact. On the contrary, the effect of RSS is very evident observing the values of the third column. In this case the relative increment reaches the 30.7 %. As noted in the Section 2.3.4, the voltage level is an important parameter involved in on board dissipation and thus with L_u level. The voltage level during all the identified braking events is considerably high compared with the nominal value of 1500 V, as it can be seen by the statistics of Fig. 2.20. This is a consolidated practice in railways systems. A higher voltage level allows to reduce Joule effect losses in train supply, but it is supposed also to limit the amount of energy that could be injected and thus increasing the line unavailability. In order to evaluate the influence that the voltage level could have on L_u, Fig. 2.26 and Fig. 2.25 show a scatter chart of L_u with respect to the ratio between voltage level during the braking (v_P) and nominal line voltage (V_N). In particular, the voltage has been determined for each braking event in correspondence of the peak injected current to emphasize the relation between voltage and L_u. This analysis was conducted in a similar way to what was done previously, so the results obtained with the grid supplied with the reversible substation are reported with reference to high and low number of trains in Fig. 2.26 a and b, respectively. Similarly, Fig. 2.25 shows results obtained with the grid supplied through the conventional substation.

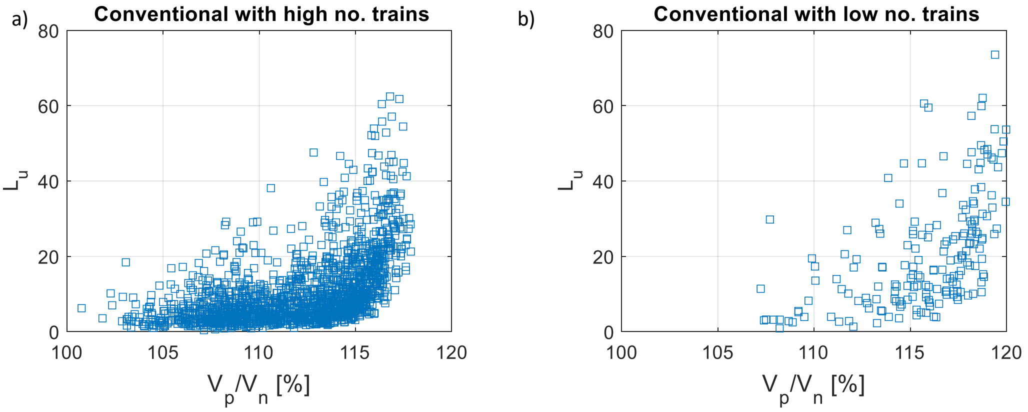

Fig. 2.25 Scatter chart of line unavailability versus measured voltage level with the grid supplied by a conventional substation, considering a high number of trains (≥9) a) and low number of trains (≤3) b).

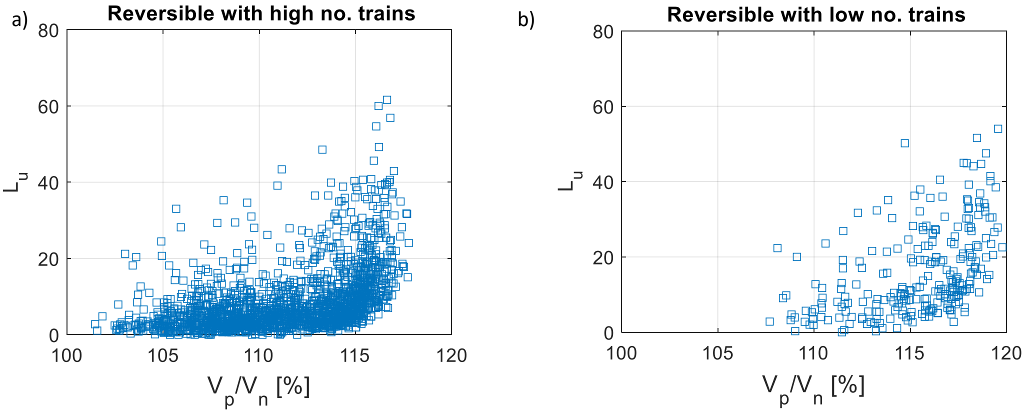

Fig. 2.26 Scatter chart of line unavailability versus measured voltage level with the grid supplied by the reversible substation, considering a high number of trains (≥9) a) and low number of trains (≤3) b).

It can be noted that there is no significant difference in charts when the number of train is high. In fact, these are the cases in which the reversible substation is less exploited because the main energy exchange is among trains and not between a train and the substation. The situation is different when a comparison is made between low number of trains and high number of trains running when the grid is powered by the conventional substation; in this case the dots move to a condition in which the voltage and the unavailability of the line are higher. The impact of the reversible substation is visible in Fig. 2.26b since, although the voltage level is higher with respect to the case of high number of trains, the L_u remains the same.

To simplify the comparison between the reversible and conventional case, an exponential interpolation of such a scatter has been performed. Even if the interpolation is not a good representation, because the data are quite scattered, the exponential could represent, theoretically, the relationship between L_u and the voltage level. The results are reported in Fig. 2.27 a and b respectively for low and high number of trains.

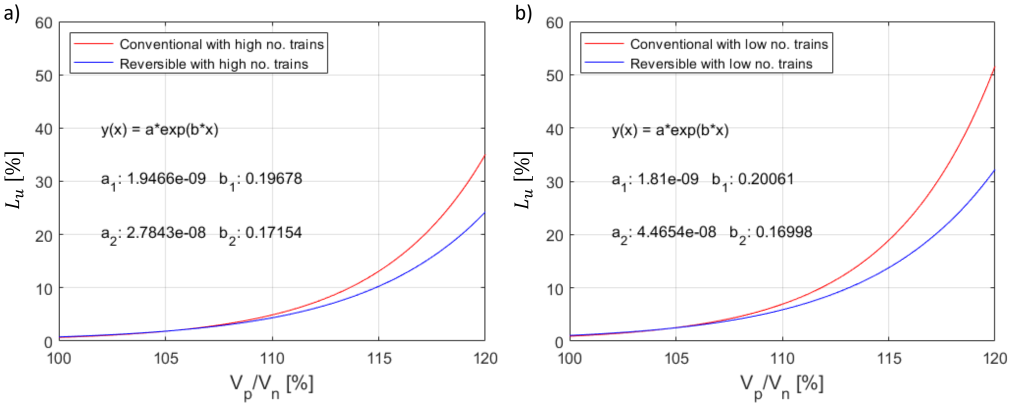

Fig. 2.27 Exponential fittings in correspondence of a low a) and high b) number of trains.

As it can be seen, they confirm the impact of the RSS in both cases. As expected, the difference between reversible condition and conventional one is greater in low receptivity than high. Moreover, for both conditions, at high voltage levels there is a greater impact of the RSS. The curves reported in Fig. 2.27 can be also used to analyse which would be the impact of a reduction of a supply voltage in terms of reduction of L_u. It is evident that with the presence of a RSS, higher levels of the supply voltage can be adopted without a sensible increment of L_u.

2.3.7 Energy flow analysis

In Table 2.8 the results of a comprehensive energy analysis of a week, in which the reversible unit is operating, is reported. As stated before, the measurements are conducted on single traction unit, so they should be doubled to have the values for all the train. At the pantograph, the absorbed ($i_\mathrm{P} \geq 0$) and the injected ($i_\mathrm{P} < 0$) energies are evaluated separately and reported together with the net amount of energy.

Table 2.8 Energy monitoring results in reversible conditions.

Working hours	**N of routes**	**Input energy (kWh)**			**Braking energy (kWh)**			**Auxiliary Services (kWh)**			**Input filter (kWh)**		
		Absorbed	*Injected*	*Net Absorbed*	*Generated*	*Dissipated*	*Net Recovered*	*Total*	*Braking Phase*	*Traction Phase*	*Total*	*Braking Phase*	*Traction Phase*
20:46	27	2266	-857	1408	985	65	920	206	54	151	46	5	41
20:44	26	2124	-816	1308	946	84	862	117	35	82	49	4	44
16:36	21	1626	-613	1013	703	52	650	134	33	101	34	3	30
12:45	16	1366	-549	817	624	45	578	79	25	54	30	3	27
04:38	6	471	-194	277	215	11	204	24	9	15	9	1	8
20:18	26	2264	-919	1344	1065	96	969	119	43	76	51	6	45
9:25	12	1037	-385	652	475	62	413	92	27	65	22	2	20
16:26	21	1680	-635	1044	754	77	677	141	54	88	34	4	31

The average value of the recovery factor was about 38%. During braking stage, as expected, most of the energy is recovered; nevertheless, an average amount of 9% of regenerated energy is dissipated on board. The auxiliary services have a minor impact on energy balance, and they just cover the 5% of the absorbed power. The loss in the input filter (2%) has low influence too.

It is possible to calculate the average flows of power, starting from the totals of energies in Table 2.8 and averaging over working hours (see Fig. 2.28). During absorption periods ($E_P \geq 0$), the single traction unit works as a load with an average power absorption of about 105 kW (blue arrows) and almost all the power goes for traction: $E_R = 0$, the auxiliary absorption and filter dissipation gives limited contribute.

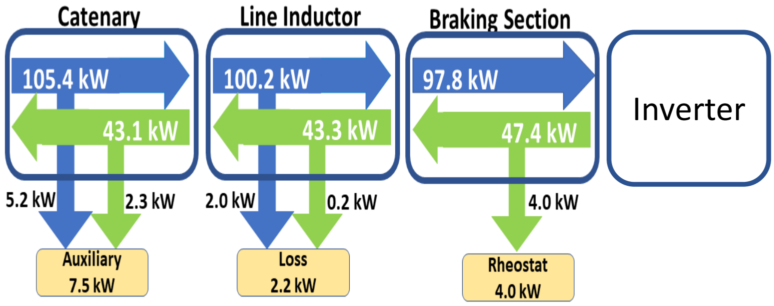

Fig. 2.28 Average energy flow over working hour for single traction unit.

During the braking, the energy flow is inverted (green arrows): E_T becomes negative (the energy is generated by the motor) and, as a consequence of the line receptivity, the energy is partially dissipated in the braking rheostats (9%) and partially reused (91%). It is interesting to note that the recovered energy is partially absorbed by auxiliary systems, partially dissipated in the filter and the rest of the energy is fed back to the catenary.

Chapter 3

Methodologies for the evaluation of pulsed braking energy

The current scenario, where a quarter of Europe's greenhouse gas emissions depend on the transport sector, must change. For this reason, the policy of the EU Commission is to promote the development of sustainable and intelligent mobility, [42], through huge investments for rail transport in urban areas. Consequently, an increase in energy costs for rail transport is expected so a more efficient energy management is mandatory.

The data obtained, not for billing purposes, shows that along a 120 km route, a train dissipates on average 200 kWh on the rheostats [9]. Considering that several trains of the same type travel on the same route, a consumption of 1 GWh per year is estimated for a single route; To give an idea of the amount of energy, just think that this value corresponds to the annual consumption of about 365 families. Having accurate knowledge of wasted energy is also valuable for insiders as, for example, it can help in the design, sizing and positioning of energy storage systems and / or reversible substations.

The energy dissipated during the braking phase on the rheostats is often estimated through indirect approaches. These techniques are based on the information of traction effort and the speed reduction in order to measure the mechanical braking power and, through the nominal performances, it is transformed into electrical energy; this is only a portion of the braking energy supplied by the inverters, therefore the surplus is the dissipated energy.

The reason for an indirect measurement is given by a considerable difficulty and a not negligible cost of a direct measurement considering the dynamics of the signals involved. The dissipation of energy occurs through semiconductor devices that switch current levels of the order of thousands of amperes and a few hundred hertz. They also have a high slew rate which introduces harmonic content that is certainly not contained. It is true that on-board the train there are already measurement systems for the analysis of voltages and currents in the inverter, but they do not have a sampling frequency such as to allow a reliable analysis of the power flows; in fact, these are used only for diagnostic reasons. In literature, it is possible to find documents that address the problem of measuring pulsed voltage and current [43, 44], and what is the cost for the required equipment.

This chapter presents two measurement methodologies for the measurement of power dissipated on braking resistors: the first is based on an offline algorithm which involves the measurement of the current, acquired with a high sampling frequency, and the compensation of the current transducer frequency response. As shown in section 3.2.6, it is impossible to apply this method online, which instead has exceptional performances. The second methodology presented is designed to be applied directly on board with the instrumentation already available with performances comparable to the ones of the offline method. This methodology can be a valuable tool for the railway operator to accurately determine di actual power dissipated on board rheostats avoiding high investments on measurement instrumentation. Before the presentation of the mentioned methodologies, a detailed description and the modeling approach of the rheostat circuit have been provided and measurement issue related to this type of measurement are exposed.

3.1 The braking chopper: description and modeling approach

As discussed extensively above, if the voltage rises beyond a threshold defined by the railway operator, the braking chopper modulates the voltage to power, in a controlled manner, a resistor called rheostat [45]. The functional diagram of the chopper is shown in Fig. 3.1; the duty cycle imposed on the GTO regulates the flow

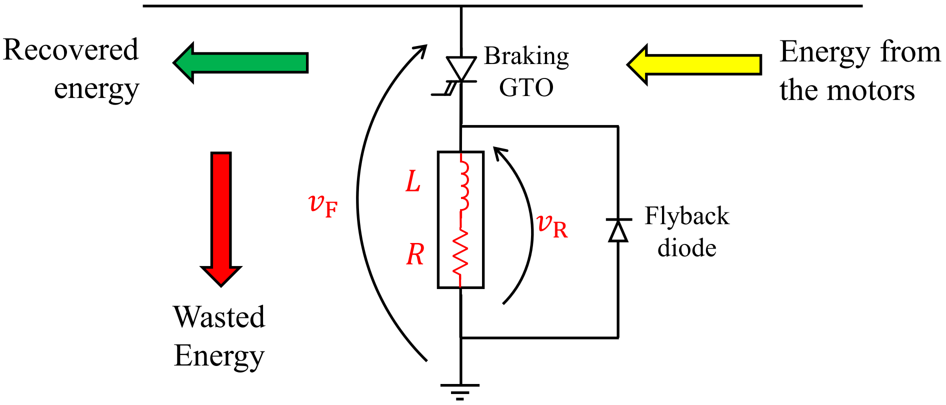

Fig. 3.1 Functional diagram of the braking chopper (GTO).

of current to the rheostat, represented in a circuital representation as a resistor in series with an inductance.

In order to avoid excessive complexity, the dissipation system model can be obtained by not considering the flyback diode (necessary to discharge the energy dissipated in the stray inductance and avoid overvoltages), and by replacing the GTO with a pulse generator [46] which switches between the voltage applied, $v_F(t)$ and zero. As reported in [47], when the GTO is open (off), the pulse generator $v_{GTO}(t) = v_F(t) - v_R(t)$ imposes a voltage equal to $v_F(t)$; in this way, according to Kirchhoff's law, the applied voltage the braking resistor is zero, as is the current $i_R(t)$.

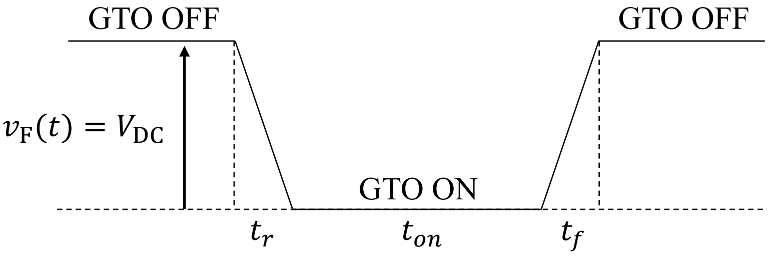

Fig. 3.2 Time characteristics of the voltage pulse generator simulating the voltage across the rheostat resistor.

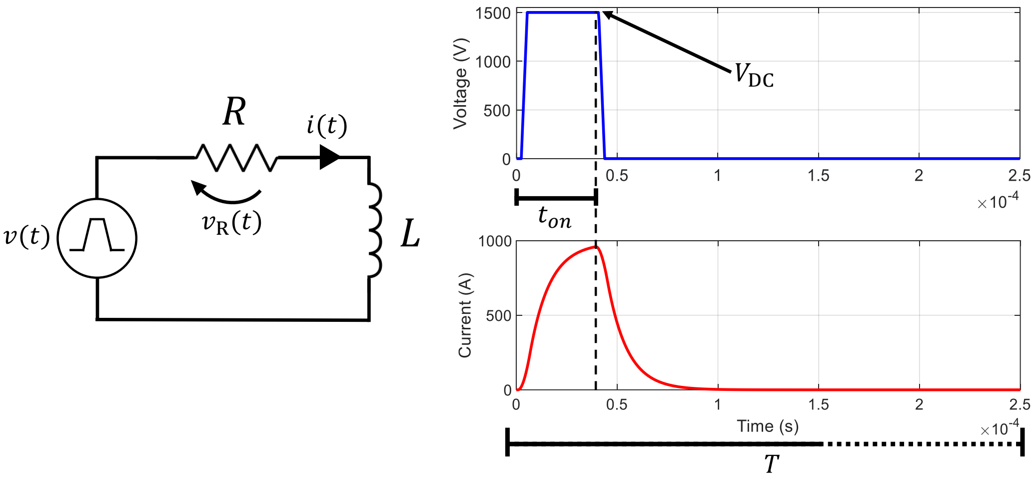

Fig. 3.3 Circuit for the model of braking rheostat pulse.

When the GTO is closed (on), the pulse generator imposes a zero voltage; consequently, the voltage $v_F(t)$ supplies the braking resistor. The simulated pulses generator allows for considering the on and off times of the GTO by introducing a rise, t_r, and fall time t_f. In Fig 3.2 the behavior of the GTO is shown, while in Fig 3.3 the circuit considered for the chopper operating model is provided.
The model of the current in braking rheostat, expressed in the Laplace domain is:

$$I_R(s) = \frac{V_R(s)}{R + sL} \tag{3.1}$$

Eq. 3.1 allows to estimate the transfer function that binds the voltage and the current that flows through the braking rheostat. The simulation was evaluated with the characteristic R and L values of the metropolitan train described in section 2.3.1; in this specific case, $R = 3\,\Omega$, $L = 36\,\mu$H, v_F has a peak value of 1.65 kV and the switching frequency is 300 Hz. Some example results provided by the simulation for different values of duty-cycle δ are provided in Fig. 3.4. In the case δ = 0.5%, the current is not able to reach the maximum value of 550 A due to the delay introduced by the presence of the stray inductance. For higher values of δ, the current reaches the steady-state within approximately 0.1 ms.

The average power dissipation is evaluated over the chopping period T, and it is based on the product of the chopped current i_R, and voltage at input of the braking chopper $v_R(t)$ which is constant and equal to V_{DC}. Neglecting the contribution of the finite slope in voltage commutation from 0 to V_{DC} and from V_{DC} to 0, the mean

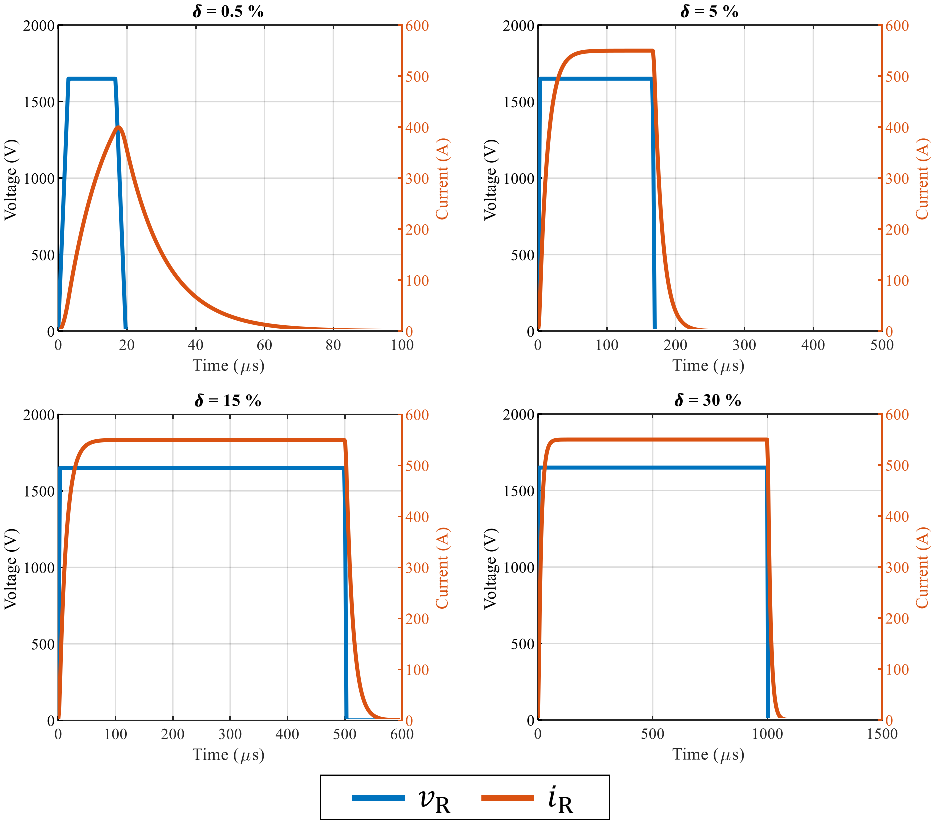

Fig. 3.4 Chopped voltage (blue) and current (red) in the braking rheostat for different values of duty-cycle

power $\overline{P}$ can be obtained as:

$$\overline{P} = \frac{1}{T} \cdot \int_0^T v_F(t) \cdot i_R(t)\, dt \approx \frac{V_{DC}}{T} \cdot \int_0^T i_R(t)\, dt \tag{3.2}$$

Two systematic errors are introduced with this approach:

- considering the DC voltage and not the chopped voltage, the dissipated power is overestimated and the latter is related to the duty-cycle;
- obviously, all the quantities are measured through transducers: the step response to a sudden change in amplitude introduces remarkable oscillations of measured quantity that must be taken into account.

3.1.1 The measurement issues

Measuring the power dissipated on the braking rheostat is not trivial task. As shown in chapter 2, our research group has experience about installing an accurate measurement system on board. The first encountered difficulty is to reach the right measurement points for the braking rheostat; typically chopper is integrated in traction cabinet that is not accessible. Moreover, the signals of interest are pulsed with high slew rate that produces high frequency content. Transducers with wide bandwith and digitizers with high sampling frequency are required.

Currently railway operators do not measure directly energy wasted during braking. They estimate it starting from available electrical and/or mechanical measured quantities. The EN50463 [20] standard prescribes the measurement of energy exchange only at the pantograph for billing. Furthermore it establish a clustering time of 5 minute, for this reason the majority of measurement instrumentation currently installed on-board trains, adopt a sample frequency of few tens of hertz. The characteristics of rheostat current and voltage are such as to require a sampling frequency in the order of tens of kilohertz. As stated before the chopper switches high current levels (thousands of amperes), varying the duty cycle. To get an idea of the required measurement bandwidth, take into account that the chopper's PWM pulses can last a few hundred microseconds (e.g. duty of 3% and chopper frequency of 300 Hz). The measurement system required to fulfill these specifications must have high performances, the cost-benefit ratio is such as to dissuade the railway operators from including it.

3.2 Offline methodology for the accurate evaluation of the power dissipated in braking rheostat

A single voltage pulse of duration t_1 and amplitude V_{DC} inside a burst of pulses, is expressed as:

$$v_{\mathrm{R}}(t) = \begin{cases} V_{\mathrm{DC}} & \text{for } 0 \leq t < t_1 \\ 0 & \text{for } t_1 \leq t < T \end{cases} \tag{3.3}$$

where T is the repetition time of the pulses. The braking rheostat is modelled as $R-L$ (with $\tau = L/R$) series circuit (see Fig 3.1). The current flowing through the

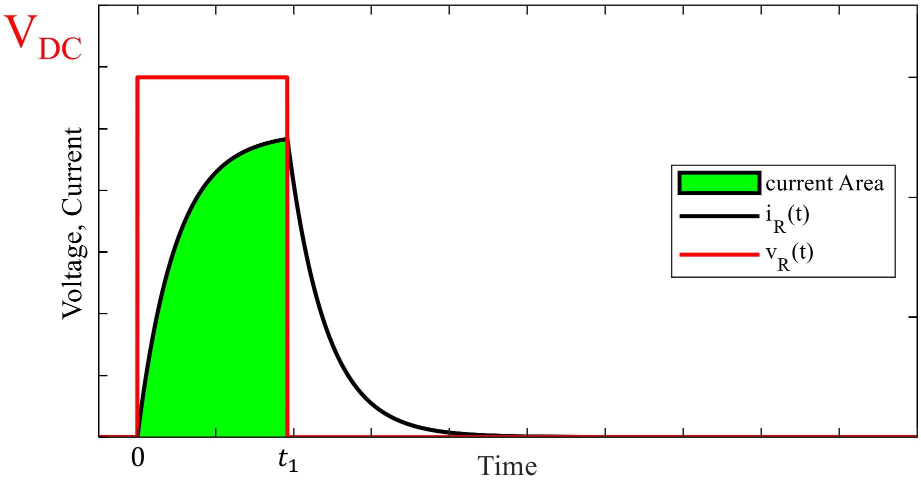

Fig. 3.5 Area below the current curve that correctly contributes to the mean power estimation

rheostat has the following exponential behavior:

$$i_{\mathrm{R}}(t) = \begin{cases} \frac{V_{\mathrm{DC}}}{R} \cdot (1 - e^{-\frac{t}{\tau}}) & \text{for } 0 \le t < t_1 \\ \frac{V_{\mathrm{DC}}}{R} \cdot (1 - e^{-\frac{t_1}{\tau}}) \cdot e^{-\frac{t-t_1}{\tau}} & \text{for } t_1 \le t < T \end{cases} \tag{3.4}$$

It is worthwhile noting that (see Fig 3.1), in practical application, t_1 is always less than $T/2$, so the current always reaches zero befor the following pulse. The correct mean power, P_{corr}, associated with the pulse and computed over a time-period T is:

$$\overline{P}_{\mathrm{corr}} = \frac{1}{T} \cdot \int_0^T v_{\mathrm{R}}(t) \cdot i_{\mathrm{R}}(t)\, dt = \frac{1}{T} \cdot \left\{ \int_0^{t_1} v_{\mathrm{R}}(t) \cdot i_{\mathrm{R}}(t)\, dt + \int_{t_1}^T v_{\mathrm{R}}(t) \cdot i_{\mathrm{R}}(t)\, dt \right\} \tag{3.5}$$

Since the voltage is zero for $t > t_1$, the second component is zero, and the power can be re-written as:

$$\overline{P}_{\mathrm{corr}} = \frac{V_{\mathrm{DC}}^2}{R} \cdot \left\{ \delta - \frac{\tau}{T} \cdot \left(1 - e^{-\frac{\delta T}{\tau}}\right) \right\} \tag{3.6}$$

where δ is the duty-cycle ($t_1 = \delta \cdot T$). Fig 3.5 shows the area below the current curve that contributes to the correct power estimation. Now the question is: what happens if we consider the voltage $v_{\mathrm{F}}(t)$ that has a constant behavior rather than the chopped voltage $v_{\mathrm{R}}(t)$? In this case, eq (3.4) applies, and the area below the current that contributes to the mean power is shown in Fig 3.6. The new mean power that is

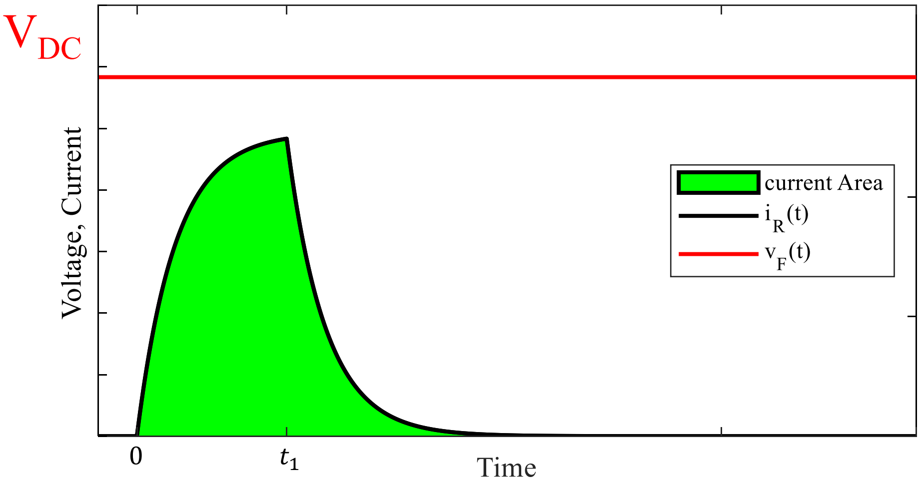

Fig. 3.6 Area below the current wave that contributes to the wrong estimation of the mean power

affected by a systematic error is now:

$$\overline{P}_{\text{wrong}} = \frac{1}{T} \cdot \left\{ \int_0^{t_1} v_{\text{R}}(t) \cdot i_{\text{R}}(t)\, dt + \int_{t_1}^{T} v_{\text{R}}(t) \cdot i_{\text{R}}(t)\, dt \right\} \tag{3.7}$$

Which is equal to:

$$\overline{P}_{\text{wrong}} = \overline{P}_{\text{corr}} + \frac{1}{T} \cdot \left\{ \int_{t_1}^{T} v_{\text{R}}(t) \cdot i_{\text{R}}(t)\, dt \right\} \tag{3.8}$$

Given that the voltage $v_{\text{F}}(t)$ is considered constant and equal to V_{DC} and introducing the definition of $i_{\text{R}}(t)$, (3.4), Equation (3.8) becomes:

$$\overline{P}_{\text{wrong}} = \overline{P}_{\text{corr}} + \frac{1}{T} \cdot \frac{V_{\text{DC}}}{R} \cdot (1 - e^{-\frac{t_1}{\tau}}) \cdot e^{-\frac{t-t_1}{\tau}} \tag{3.9}$$

The difference between the wrong power and the correct power is

$$\overline{\Delta P} = \frac{V_{\text{DC}}^2}{R} \cdot \left(1 - e^{-\frac{\delta t}{\tau}}\right) \cdot \frac{\tau}{T} \cdot \left(1 - e^{-\frac{T}{\tau} \cdot (1-\delta)}\right) \tag{3.10}$$

It is possible to account for this effect by introducing a correction coefficient. Considering that, under real circumstances, the quantity $v_{\text{F}}(t)$ is not constant, the corrected measured values becomes:

$$\overline{P}_{\text{corr}} = \left[\frac{1}{T} \int_{k\cdot T}^{(k+1)\cdot T} v_{\text{F}}(t) \cdot i_{\text{R}}(t)\, dt \right] \cdot K_{DC}(\delta);\ with\, k = 0, 1, 2\, ... \qquad (3.11)$$

Table 3.1 provides the values of the correction coefficient K_{DC} for different values of duty-cycle, defined as the ratio between $\overline{P}_{\text{corr}}$ and $\overline{P}_{\text{wrong}}$. The values were obtained for a time period of the chopped signal equal to $T = 1/300$ Hz, a rheostat resistance $R = 3.4\ \Omega$ and $L = 36\ \mu$H.

Table 3.1 Correction factor K_{DC} for different chopper duty-cycle δ.

$\delta(\%)$	**K**$_{\text{DC}}$
0.7	0.633
2	0.850
4	0.923
8	0.961
10	0.969
15	0.979
30	0.990

3.2.1 Frequency characterization of current sensors

In the application described in this section, the current transducer is used under conditions much different from those of common use. For this reason, it is fundamental to know the behavior of the sensor under actual operating conditions; that is, with a pulsed current with amplitude of 500 A and at frequency of 300 Hz [48]. In order to be able to measure such a pulsed current a LEM HOP 800 sensor was selected, which is an open loop Hall effect sensor designed for measurements of DC, AC and pulsed currents. The current range of the sensor is 800 A root-mean-square (RMS), the maximum attenuation in the 10 kHz band is -1 dB, and the nominal voltage isolation is 2 kV. The primary and secondary circuits are galvanically separated. The sensor loop has an openable core, which simplifies the installation on-board the train. Fig 3.7 shows a schematic representation of the HOP 800. Table 2 presents the main nominal characteristics of the sensor. It can be simulated by reconstructing and modeling the frequency response with a transfer function at currents similar to those

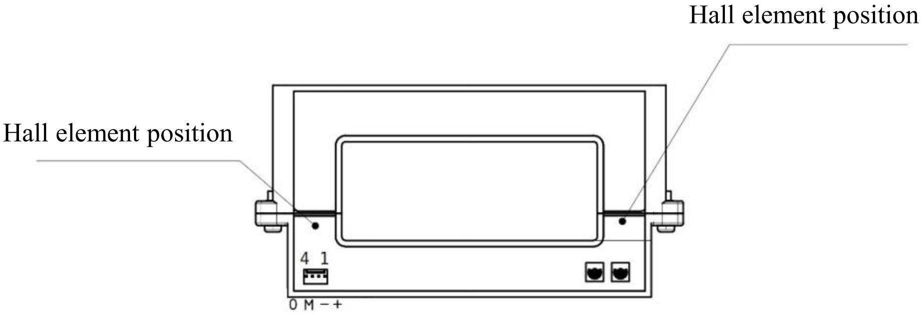

Fig. 3.7 Schematic representation of the HOP current sensor.

during a real measurement campaign. The actual frequency response was accurately estimated at the INRiM labs using a reference current transducer LEM ITZ Ultrastab, with excellent linearity within 1 to 10 parts in 106 (parts per million, ppm).

Table 3.2 Summary of the main specifications of the LEM HOP 800 current sensor.

Parameter	**Value**
Primary nominal RMS current	800 A
Output voltage	± 4 V
Supply voltage (±5%)	12 ... 15 V
Accuracy	$\leq \pm$ 2%
Slew rate	50 A/μs
Voltage insulation	2000 V
Frequency bandwidth (-1 dB)	DC ... 10 kV

It guarantees an overall accuracy at nominal current, 125 A in this case, at +25 °C better than 12 ppm. Moreover, it has a wide frequency bandwidth from DC up to 500 kHz and it is based on closed-loop fluxgate technology. The output of this transducer is a current, that was measured using a broadband 1 A, 100 kHz 7320 Guildline shunt. The frequency dependence of the shunt varies from essentially zero at power frequencies to less than 10 ppm up to 10 kHz. For the current generation a Clarke-Hess Model 8100 trans-conductance amplifier has been used. The six overlapping ranges of the amplifier, 2 mA, 20 mA, 0.2 A, 2 A, 20 A, and 100 A, provide output currents with distortion less than -60 dB up to 10 kHz (typically 20 kHz) and less than -40 dB to 100 kHz at all current ranges. The input signal for the trans-conductance amplifier was generated using a National Instruments

5422 digital-to-analogue converter. The NI 5422 is a waveform generator with the following features: sampling frequency up to 200 MHz, 16-bit resolution output channel, full scale range 12 V (peak-to-peak) for a 50 Ω load up to 80 MHz, DC offset up to ± full scale and a bandwidth of 80 MHz [49]. A National Instruments PXIe-6124 was synchronized to the generator and used to measure the voltage to characterize the HOP sensor. The NI 6124 is a multi-functional simultaneous sampling data-acquisition device, with a 16-bit analog-to-digital converter and a sampling rate up to 4 MSa/s per channel. Fig 3.8 shows the block diagram of the setup used to characterize the current sensor. For specific frequencies in the range from 47 Hz to 40 kHz the gain has been evaluated 30 times with an averaging time of 1 s.

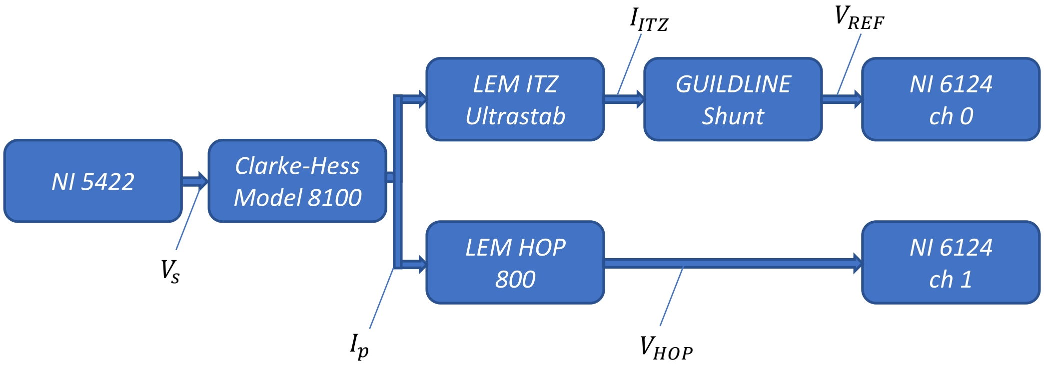

Fig. 3.8 Scheme of the set-up for the frequency characterization of the current sensor.

The gain for the i-th frequency, $G_{\text{dB}}(f_i)$, expressed in dB, can now be defined as follows:

$$G_{\text{dB}}(f_i) = 20log_{10}\left(\frac{I_{\text{HOP}}(f_i)}{I_{\text{ITZ}}(f_i)}\right) = 20log_{10}\left(\frac{K_{\text{HOP\_DC}} \cdot K_{\text{ch1}} \cdot V_{\text{HOP}}(f_i)}{K_{\text{ITZ}} \cdot K_{\text{GUI}} \cdot K_{\text{ch0}} \cdot V_{\text{REF}}(f_i)}\right) \quad (3.12)$$

where $I_{\text{HOP}}(f_i)$ and $I_{\text{ITZ}}(f_i)$ are the magnitude of the phasors of the primary current I_p, at frequency f_i, measured by the HOP sensor and the ITZ sensor respectively. The current I_{HOP} can be written as the product of the voltage measured by the acquisition system, $V_{\text{HOP}}(f_i)$, multiplied the channel gain, K_{ch1}, and the gain of the HOP transducer in stationary conditions, $K_{\text{HOP\_DC}}$. In the same way, the current measured by the reference transducer can be written as the product of the channel gain, K_{ch0}, the reference shunt gain, K_{GUI}, and the gain of the reference transducer, K_{ITZ}, multiplied by the voltage read by the acquisition system, $V_{\text{REF}}(f_i)$.

Although the transconductance amplifier has the capability to reproduce signals up to 500 kHz, the generation of the current is limited by the circuit connected to it. With an inductive load, increasing the frequency corresponds to an increase in the impedance and therefore an increase in the voltage required by the amplifier for generating the output current. The compliance voltage for this amplifier is 7 V. In order to minimize the impedance, the first tests were carried out with twisted cables as shown in the Fig 3.9 a.

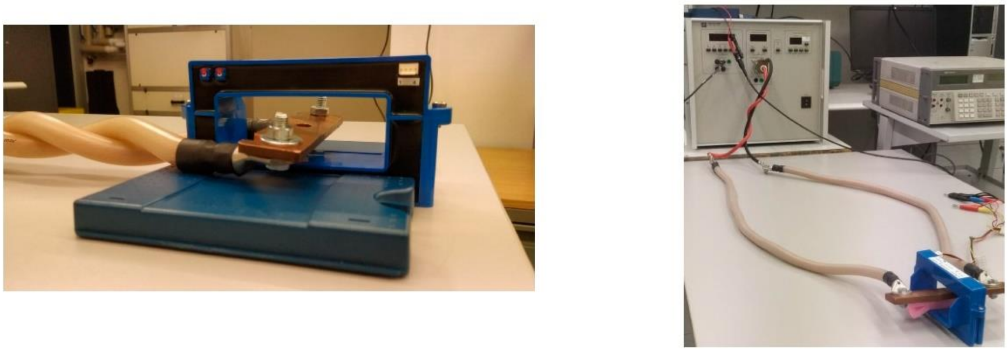
a) b)

Fig. 3.9 Pictures describing the two different primary cable arrangements: twisted cables close to the magnetic yoke of the HOP sensor a); supply cable far from the magnetic yoke of the HOP sensor b).

The result of this characterization shows that, in this configuration, the accuracy of the instrument is highly out of specification. This effect is due to the position of the Hall sensing elements in the current transducer which are influenced by the magnetic field produced by the cables in the vicinity.

Subsequently, by reducing the maximum test frequency, tests were carried out with non-twisted cables, as shown in Fig 3.9 b. The effect of the position of the primary conductor on the transducer scale factor has been investigate and described in [50]. This activity was limited to the position of the primary conductor rather than the effects of a current flowing close to the hall sensor. Moreover, a limited frequency band was analyzed.

Once the frequency characterization has been obtained, it is possible to proceed with the search for the poles and zeros that define the transfer function of the current sensor. By following the approach already presented in [51], the transfer function of the current sensor was fitted by the relation between the output current I_{HOP} and the input current I_p that best approximates the actual frequency behavior of the scale factor in the Laplace domain:

$$\frac{I_{\mathrm{HOP}}(s)}{I_p(s)} = \frac{(s-\omega_{01})\cdot(s-\omega_{02})}{(s-\omega_{p1})\cdot(s-\omega_{p2})} \tag{3.13}$$

The function is constituted by two zeros and two poles. The model allows for the estimation of the correction factors as a function of the duty-cycle that were applied to the power and energy estimated by the on-board locomotive measurements, in order to compensate for the systematic errors. Further, in this case it is possible to account for systematic errors by introducing a correction coefficient. The correction coefficient representing the sensor distortion and the limited sampling frequency can be defined as the ratio between the integral of the measured current squared and the current flowing through the rheostat squared:

$$K_{\mathrm{HOP}} = \frac{\int_0^T i_p^2(t)\,dt}{\int_0^T i_{\mathrm{HOP_Z}}^2(t)\,dt} \tag{3.14}$$

The integrals are numerically computed by implementing the trapezoid rule.

The two arrangements of the primary conductor provide considerably different frequency behavior, in particular around 10 kHz [52]. As can be seen by Fig 3.10 the effect of different primary cable arrangement is very high. The frequency behavior is compliant with the datasheet of such commercial sensor if the forward and return cables of the primary circuit of the sensor are kept far from the yoke. In fact, for case with the cables far from the yoke, the gain is about -1 dB at 10 kHz, as declared in the datasheet. The frequency bandwidth in the twisted cable configuration is considerably lower than rated, i.e., about -1 dB at 2 kHz.

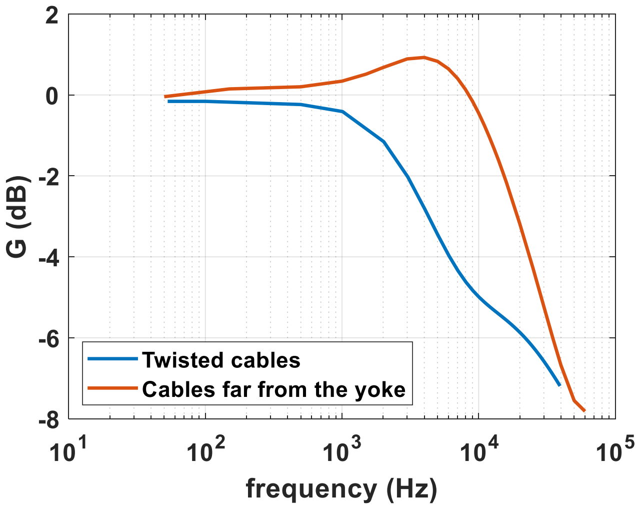

Fig. 3.10 Frequency behavior of the current sensor gain for two different arrangements of the primary conductor.

The function that approximates the frequency behavior of the current sensor has been tailored considering the behavior obtained with the cables far from the yoke of the magnetic circuit of the sensor (red curve in Fig 3.10). It can be deduced that an overshoot occurs around 5 kHz. Such behavior can be reproduced by a couple of two complex and conjugate poles. Moreover, one can note that the slope of the measured frequency dependence is lower than the expected 40 dB per decade produced by the two poles; this is taken into account by introducing a zero at about 3 kHz that reduces the slope and allows a better fit in the frequency range between a few kilohertz to 10 kHz. The description of the fit function Gfit, in the Laplace domain, is based on Equation (3.13) described as follows:

$$G_{\text{fit}} = \frac{(s-\omega_{01})\cdot(s-\omega_{02})}{(s-\omega_{p1})\cdot(s-\omega_{p2})} \tag{3.15}$$

$$\begin{gathered}
\omega_{01} = -2\pi\cdot 4.3\cdot 10^3; \\
\omega_{02} = -2\pi\cdot 20\cdot 10^3; \\
\omega_{p1}, \omega_{p2} = -\sigma\cdot\omega_p \pm j\omega_p\cdot\sqrt{1-\sigma^2}; \\
\sigma = 0.91, \omega_p = 2\pi\cdot 6.3\cdot 10^3;
\end{gathered} \tag{3.16}$$

A comparison between the fit functions and the measured frequency dependence of the sensor gain is provided in Fig 3.11. The fit agrees with the measurement data within 0.5 dB up to 10 kHz.

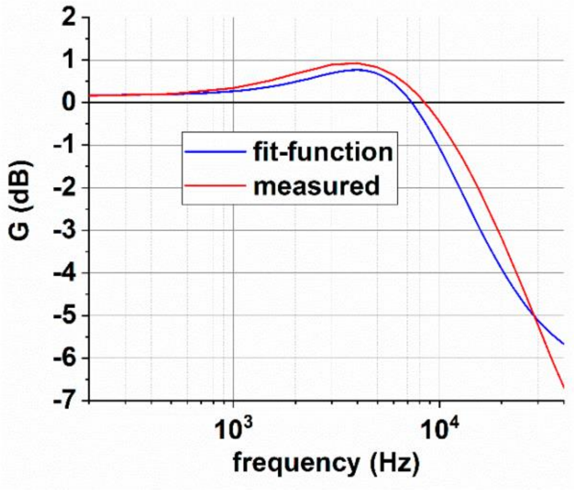

Fig. 3.11 Comparison between frequency function of the identified fit-function and the measured one.

3.2.2 The actual current flowing in the braking rheostat

Using the transfer function of the braking rheostat and the current sensor, it is possible to compare the time behavior of the simulated-actual current, i_{sim}, flowing in the braking rheostat, the distorted signal provided by the current sensor, i_{HOP}, its digitization, i_{HOPZ}, and the samples acquired on-board the locomotive, i_{measured}. Fig. 3.12 provides a comparison among such quantities for two different vales of the duty-cycle δ of the braking chopper: $\delta = 0.9\%$ that is the minimum recorded value (Fig. 3.12a) and $\delta = 15\%$ (Fig. 3.12b).

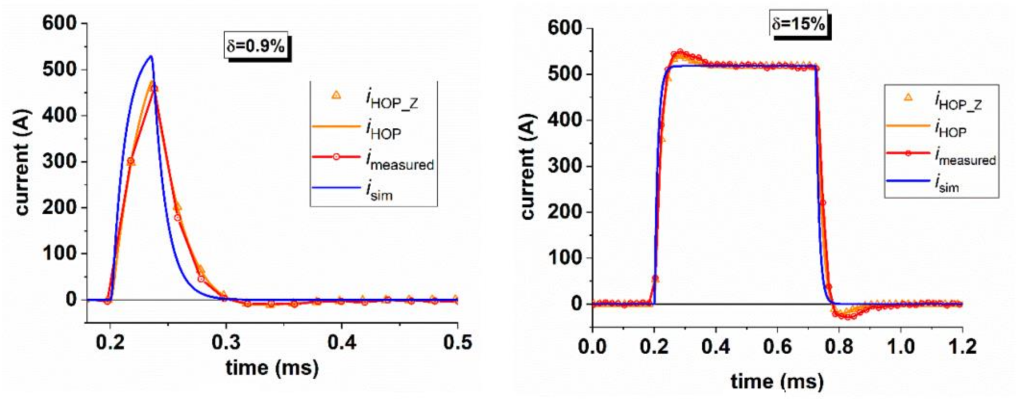

a)

b)

Fig. 3.12 Comparison between the actual current flowing in the rheostat, the distorted signal provided by the current sensor and the digitization effects for a duty-cycle of 0.9% a) and 15% b).

For low duty-cycle, the distortion introduced by the current sensor is much more evident, the peak value of the actual current is not detected. For higher duty-cycle, the overshoot on the signal provided by the sensor, shown in Fig. 3.12b, is the effect of the two complex poles. The good overlap between the measured current and the signal provided by the simulation demonstrates the accuracy of the frequency characterization of the current transducer.

3.2.3 Sampling effects in the dissipated power/energy estimation

The sampling mechanism, in particular for pulses with a low duty-cycle, can dramatically affect the area underneath the sampled curves. Moreover, the position of the first sample following the onset of the pulsed signal can provide different results in terms of the area estimation and thus provide different power estimation. A demonstration of the size of this effect is shown in Fig 3.13a for a duty-cycle of $\delta = 0.9\%$. The effect in the time domain of a different position of the first sample is provided in Fig 3.13b. In particular, the figure shows the position of the samples that provide the lowest and biggest deviation between the area underneath the actual current wave and the sampled signals.

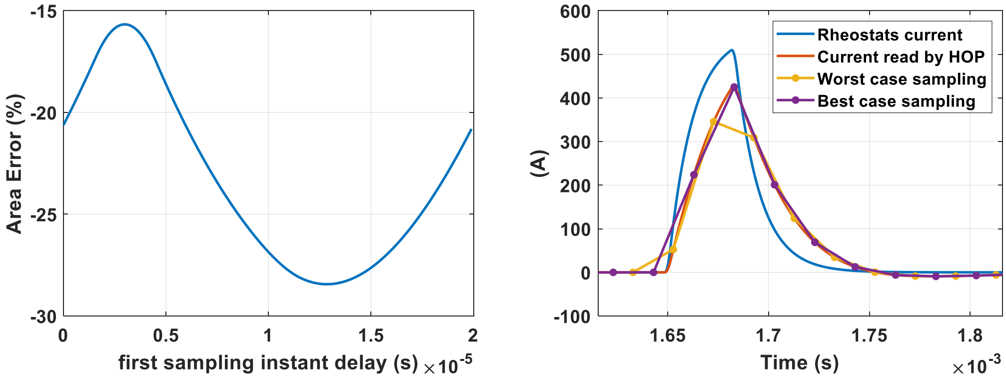

a) b)

Fig. 3.13 Impact of the position of the first sample following the current pulse for a duty-cycle of $\delta = 0.9\%$ a). A comparison between signals obtained by sampling the current information provided by the current transducer with a different position of the first sample b).

3.2.4 Methodology for accurate estimation of the dissipated power

As shown in the previous section, the systematic deviations due to the voltage-and-current measurement method can be accounted for by correction factors. So, the full measurement model now becomes:

$$\overline{P}_{\mathrm{corr}} = \left[\frac{1}{T} \int_{k\cdot T}^{(k+1)\cdot T} v_{\mathrm{F}}(t) \cdot i_{\mathrm{R}}(t) \cdot dt \right] \cdot K_{\mathrm{DC}}(\delta) \cdot K_{\mathrm{HOP}}(\delta); \text{ with } k = 0, 1, 2, \ldots \quad (3.17)$$

As shown in the previous section, the error is dependent on the value of the chopper duty-cycle δ. However, there is no direct information on duty-cycle because the chopped voltage is not measured. So, the duty-cycle should be estimated using the current measurements, but there is a difference between the duty-cycle measured on current and measured on voltage because of the distortions introduced by the stray inductance of the rheostat and by the current sensor. In particular, the duty-cycle of the chopped current is always higher than the chopped voltage duty-cycle (see Fig 3.4). Thanks to the model of the braking rheostat that provides the current behavior by applying a pulsed voltage of known duty-cycle, the relation between the duty-cycle of the chopped current, δ_{I}, and the duty-cycle of the chopped voltage, δ_{V}, applied to the rheostat can be identified. The relation between δ_{V} and δ_{I} is shown in Fig 3.14) for the lowest values.

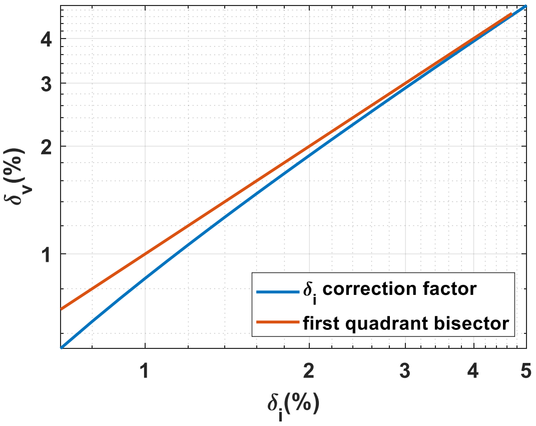

Fig. 3.14 Duty-cycle δ_V versus δ_I. The first quadrant bisector is shown for indicative purposes only.

This relation is fitted using the ad hoc function:

$$\delta_V = a \cdot \sin(\delta_I - \pi) - b \cdot (\delta_I - 10)^2 + c \tag{3.18}$$

where a, b, and c are equal to 4.253, 0.2636 and 26.36, respectively. Equation (3.18) has been carried out by the black-box approach, exploiting the optimization algorithms provided by Matlab software.

The procedure that provides the corrected power dissipated by the braking rheostat is summarized in Fig. 3.15. The measured chopped current is processed in order to determine the duty-cycle δ_I for a specific period T and to calculate the power dissipated by the rheostat P. From this, it follows that the minimum time for the estimation of the duty-cycle and the relative correction of the dissipated power is a single period of the chopped signal, in this case 3.34 ms. In order to reduce the impact of a single outlier on the estimated power, such time-interval can be enlarged of an integer number of times.

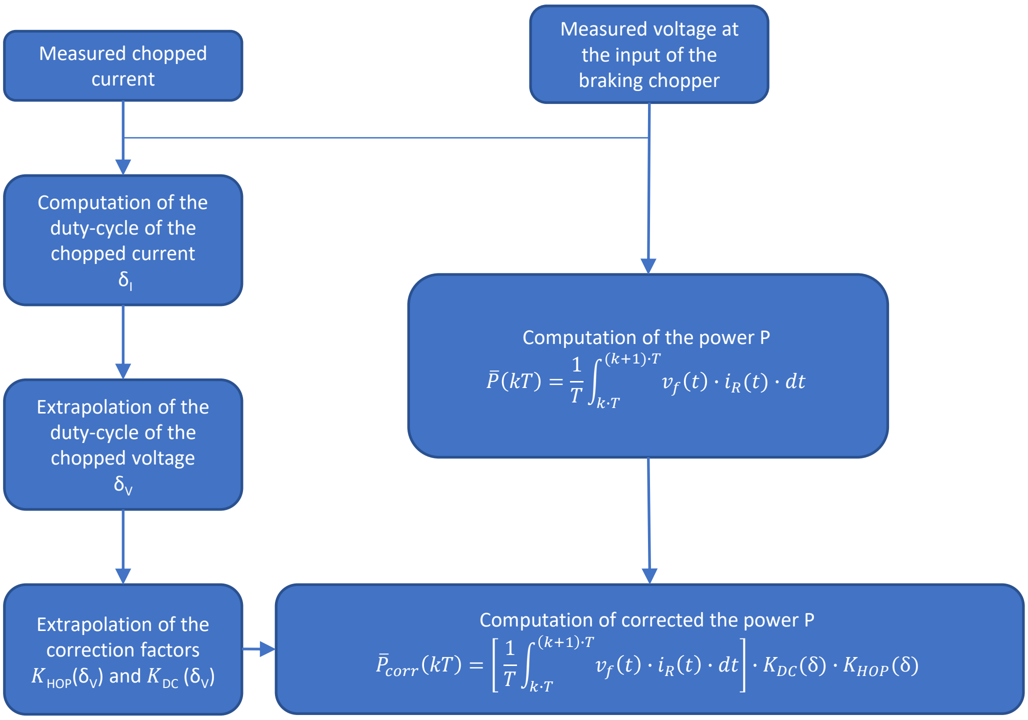

Fig. 3.15 Procedure for the estimation of the correct power dissipated by the braking rheostat.

3.2.5 Estimation of the correction coefficient as a function of the current duty-cycle

The correction coefficient K_{HOP}, defined in Equation (3.14), strongly depends on the duty-cycle of the chopped voltage signal. In detail, K_{HOP} is high with a low duty-cycle, where the distortion effect introduced by the current transducer is higher. Such effect is also evident in Fig 3.16.

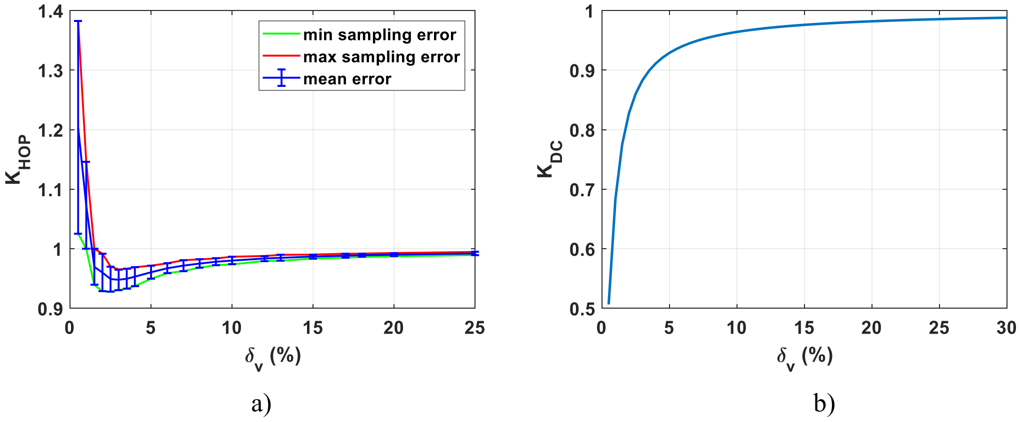

Fig. 3.16 Correction coefficient K_{HOP} versus the chopper duty-cycle δ_{V} a). Correction coefficient K_{DC} versus the chopper duty-cycle δ_{V} b).

The value of K_{HOP} depends on the position of the samples in time with respect to the position of the pulse. This information is not deterministic but random; as a consequence, for each duty-cycle a distribution of possible values of K_{HOP} is found by varying the temporal position of the samples. This procedure provides a bandwidth of possible values of K_{HOP} for each duty-cycle value. Fig 3.16a describes the behavior of K_{HOP} as a function of the duty-cycle and the error bars indicate the bandwidth of possible values. The correction coefficient K_{DC} that compensates for the error in the definition of the power dissipated by the rheostat is significant for low duty-cycle and tends to unity with increasing duty-cycle, as shown in Fig 3.16b. Some values of the two correction coefficients and their product with the associated interval of maximum variability due to the position of the samples in time with respect to the pulse onset position is provided in Table 3.3.

Table 3.3 Correction coefficients K_{HOP} and K_{DC}, and their product with the associated interval of maximum variation due to the sampling effect.

$\delta_V(\%)$	$\mathbf{K_{HOP}}$	$\mathbf{K_{DC}}$	$\mathbf{K_{DC} \cdot K_{HOP}}$
0.7	1.124	0.633	0.711 ± 0.064
2	0.960	0.850	0.816 ± 0.027
8	0.975	0.961	0.937 ± 0.007
10	0.980	0.969	0.950 ± 0.006
15	0.987	0.979	0.966 ± 0.003
30	0.993	0.990	0.983 ± 0.002

3.2.6 Application of the methodology to measured data

The proposed procedure is applied to a single electrical braking event recorded during a commercial route of a train operating on line 10 B of Metro de Madrid [6]. The braking event lasts for about 10 s. The DC voltage at the input of the chopper is 1780 V on average (see Fig 3.17a).

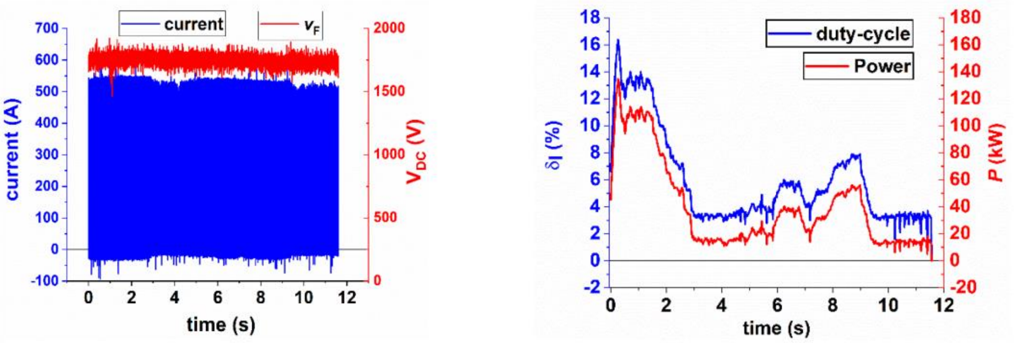

a) b)

Fig. 3.17 Dissipative electric braking taken as test for the proposed correction procedure a). Time behavior of the dissipated power and the current duty-cycle b).

The time behavior of the two input parameters of the methodology proposed for the correction, δ_I and the power P have been calculated by means of the formula shown in Fig 3.15, over a time window of 20 ms (six periods of the chopped signal). Such integration time allows to reduce the impact of a single outlier on the estimated quantities without losing the information on their dynamic variations. The variation of these quantities with time is shown in Fig 3.17b. The dissipated power is higher at the beginning of the braking, increasing to a maximum of 160 kW; after a couple of seconds the power decreases to about 40 kW. Two power peaks of 60 kW and 80 kW are reached at about 6.5 s and 8.5 s. As can be seen from Figure 18b, the power behavior with time follows the behavior of the duty-cycle δ_{I}, computed from the chopped current. The maximum value of δ_{I} of about 15% is reached in the first instant of the braking event, whereas the minimum is about 1.8%. The time behavior of δ_{I} and the analytical function Equation (3.18) allow the estimation of the duty-cycle of the chopped voltage and, as a consequence, the time behavior of the correction coefficients K_{DC} and K_{HOP}, which is shown in Fig 3.18a. As can be seen, the weight of the combined correction coefficients ($K_{\mathrm{DC}} \cdot K_{\mathrm{HOP}}$) ranges from about 0.95 to 0.75. The value of K_{HOP} provided here refers to the mean value. A comparison between the power before the correction, P, and the values obtained after the application of the correction P_{corr}, is reported in Fig 3.18b. The same figure provides the behavior of the percent deviation Δ between the two powers computed as:

$$\Delta = \left(\frac{P}{P_{\mathrm{corr}}} - 1 \right) \cdot 100 \tag{3.19}$$

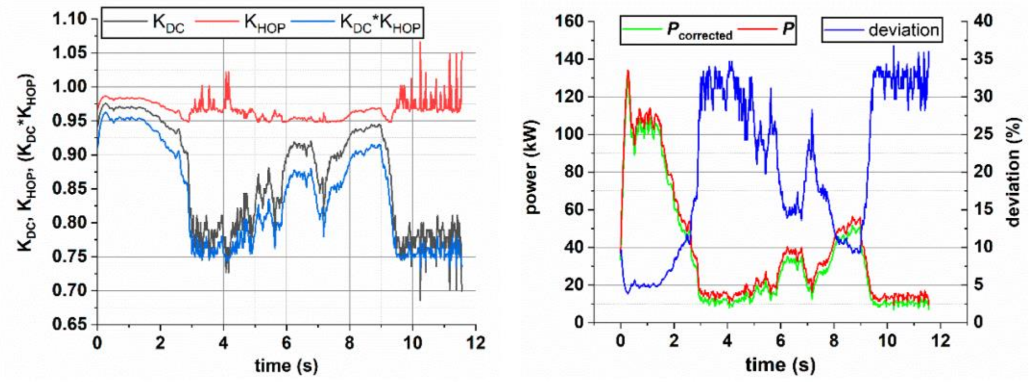

a) b)

Fig. 3.18 Time behavior of the correction coefficients a), the power P, the corrected power P_{corr}, and their deviation b).

The deviation between non-corrected and corrected power ranges from 5% to about 34%; as expected, the deviation is higher for lower power. The considered braking is characterized by an average power dissipation, for a single rheostat, of about 35.8 kW.

As described in Subsection 3.2.5, the correction factor K_{HOP} is characterized by a range of possible values for each duty-cycle value (Fig 3.16a). Such random behavior propagates into the power estimation. The impact of the correction factor on the power is about 11% with an associated range of values of $\pm 2\%$.

To give evidence of the impact of the correction on the measured power, a collection of values for the two power magnitudes and their deviation is provided in Table 3.4. The table also provides the interval of variability (±var) associated with the corrected power P_{corr} and, as a consequence, to the deviation due to the variability on K_{HOP}.

Table 3.4 Correction coefficients K_{HOP} and K_{DC}, and their product with the associated interval of maximum variation due to the sampling effect.

$\delta_{\text{I}}(\%)$	**P (kW)**	**$\mathbf{P_{corr}}$ (kW)**	$\Delta(\%)$	**±Var(%)**
3	13.8	10.3	34	4.3
7.4	54	49	10.2	1.0
10.6	84.2	79	6.6	0.65
16.4	134	129	3.9	0.37

3.3 Online methodology for measuring accurately the wasted energy

In [43] the problems of measuring pulsed voltage and pulsed current are exposed, which increase the cost of the necessary equipment. Measuring dissipated energy with an adequate level of accuracy is too expensive for railway operators who often refrain from measurement and prefer estimation based on mechanical quantities, affected by high uncertainty.

A cost-effective solution to measure energy dissipated on board with an adequate level of accuracy is needed. But, at the time of writing no article specifically addresses these energy measurement needs. The present section provides a technique to exploit already installed measurement systems and other information available to the train control system to quantify the energy wasted during braking correctly; the technique reveals easy to implement for already operating traction units. This new finding consists of neglecting two specific measurement issues, successively correcting the approximated result with a numerically determined function; this last reveals to be constant in most cases.

The reliability of the method has been investigated by performing a comparison with the rigorous approach for the braking energy estimation proposed in [47].

3.3.1 Simplified approach for the estimation of the braking rheostat energy

What it is proposed here is an alternative online method for estimation of the wasted energy that can be used directly on board the train, more accurate than those currently implemented by railway operators. To identify a way that allows simple calculations and the use of quantities already available or easily measurable, it is possible to intentionally neglect the charge and discharge transient of the inductance. By ohm's law, an approximated estimation, E_a, of dissipated energy, can be calculated as:

$$\begin{aligned} E_\mathrm{a} = \int_0^T \frac{v_\mathrm{R}(t)^2}{R}\,dt &\approx \int_0^{t_\mathrm{on}} \frac{V_\mathrm{R}^2}{R}\,dt + \int_{\mathrm{t_{on}}}^T 0\,dt \\ &= \frac{V_\mathrm{R}^2}{R}\int_0^{t_\mathrm{on}} dt = \frac{V_\mathrm{R}^2}{R}\cdot\delta\cdot T \end{aligned} \tag{3.20}$$

where T is the period of the square wave applied to the rheostat, R is the rheostat resistance, V is the amplitude of the high level of v_R, t_on is the time in which the GTO is on, and $\delta = t_\mathrm{on}/T$ is the duty-cycle. Note that V_R can be considered equal to the measured quantities v_F neglecting the voltage drop across GTO.

This approach is extremely simplified with respect to the nature of the signals analysed, since the voltage is considered constant for the entire pulse period and it completely excludes the presence of the inductance, which does not allow the current to follow the behaviour of the voltage instantaneously. The presence of inductance reduces the energy dissipated by the single pulse (see Fig. 3.5), reducing the effectiveness of the duty cycle like it is slightly lower than the actual one. So it is possible to define an equivalent square pulse with a slightly lower duty cycle that dissipates the same energy as the real pulse. This can be expressed by introducing a positive quantity ξ to be subtracted from δ in the approximated eq.3.20 obtaining:

$$E(\delta) = \frac{V^2}{R} \cdot (\delta - \xi) \cdot T \tag{3.21}$$

Knowing that the real pulse reference energy can be expressed as:

$$E_{\mathrm{REF}}(\delta) = \int_0^T v_\delta(t) \cdot i_\delta(t)\, dt \tag{3.22}$$

By equating eq.3.21 to eq.3.22 it is possible to quantify ξ:

$$\frac{V^2}{R} \cdot (\delta - \xi(\delta)) \cdot T = E_{\mathrm{REF}}(\delta) \tag{3.23}$$

where ξ is a quantity to be subtracted to δ in order to compensate overestimation and to equal the reference energy. ξ can be derived from eq. 3.23 as:

$$\xi(\delta) = \delta - \frac{E_{\mathrm{REF}}(\delta) \cdot R}{V^2 \cdot T} \tag{3.24}$$

of course ξ is a function of δ. It is possible to evaluate E_{REF} numerically from the circuital simulation described in section 3.1, in discrete form:

$$E_{\mathrm{REF}}(\delta) = \sum_{\mathrm{k}=1}^{N} v_\delta[k] \cdot i_\delta[k] \cdot t_{\mathrm{s}} \tag{3.25}$$

where t_{s} the simulation time-step and, N is the number of points in a period, note that the dependency from δ is implicit in $v_\delta[k]$ and $i_\delta[k]$. Using (3.25) in (3.24) ξ has been numerically evaluated, its behaviour with respect to delta is shown in Fig. 3.19. As it can be seen, for $\delta \geq 2\%$, ξ is practically constant, it can be assumed independent from δ and equal to its asymptotic value ξ^*:

$$\xi(\delta) \approx \xi^*. \tag{3.26}$$

The proposed method can be synthesized as:

$$E(\delta) = \frac{V^2}{R} \cdot (\delta - \xi^*) \cdot T \tag{3.27}$$

where ξ^* is the constant asymptotic value, in the specific case 0.263%.

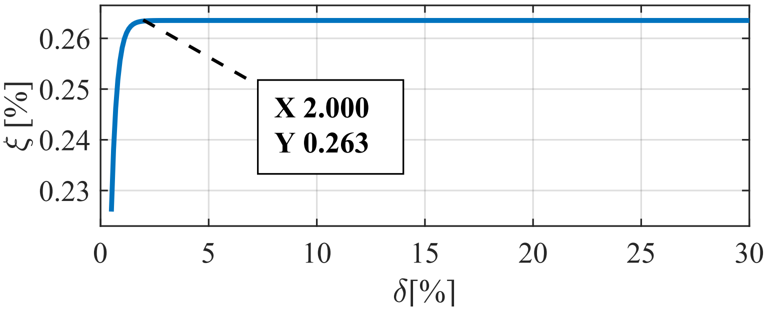

Fig. 3.19 ξ variability over δ

To evaluate the performance of the proposed method, the error has been calculated as:

$$\varepsilon(\delta) = 100 \cdot \frac{E(\delta) - E_{\mathrm{REF}}(\delta)}{E_{\mathrm{REF}}(\delta)} \tag{3.28}$$

(3.28) was evaluated by varying δ from 0.5% to 30%, with a 0.1% step. The results are depicted in Fig. 3.20 in red with $\xi = \xi^*$ and in blue with $\xi = 0$. The blue curve represents the error made, completely neglecting inductance transient; it reveals to be unacceptably high for a wide range of δ. The red curve shows that the proposed

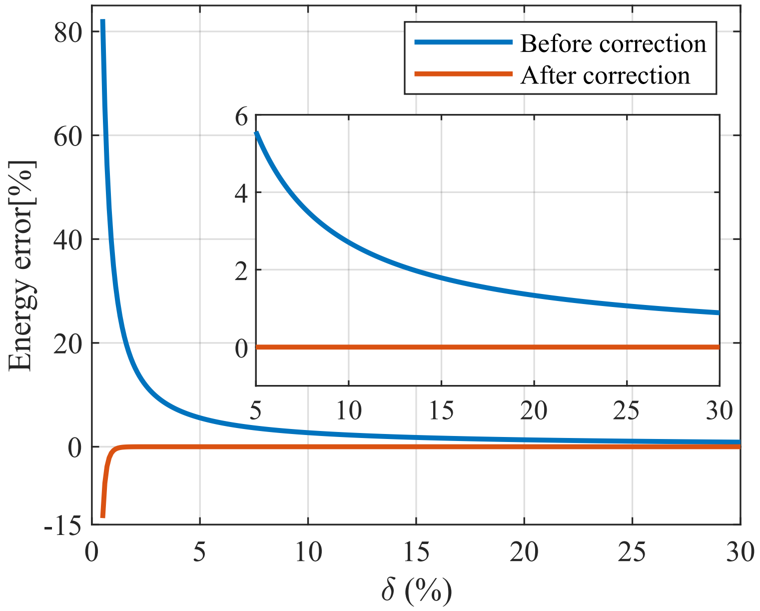

Fig. 3.20 Energy measurement error before and after the correction though ξ

method, still maintaining the simplicity of implementation, allows compensating for the error, reducing it practically to 0 for $\delta > 2\%$.

It is important to highlight that the proposed method eq. 3.27 is very simple to implement, it bypass the problem of measurement point, because it rely only on the measurement of the inverter voltage (v_F). In fact, the duty cycle is a quantity known, usually imposed by the chopper control circuit, and R can be considered constant for the required level of accuracy. The cost-effectiveness of the method is very high, it doesn't require expensive large bandwidth transducers because it does not require the measurement of pulsed signals. Moreover, the inverter voltage measurement is often already implemented in the train control unit, reducing its implementation to a matter of software.

For the best accuracy of the proposed method, it is necessary to know the value of R by characterizing the braking resistor, the obtained value must be first used in the simulation to get an accurate value of ξ^*, then must be used in (3.27).

Insertion of current sensors: an improvement to the method

An aspect that limits the accuracy of the proposed method is that the chopper current can heat the braking rheostats by the Joule effect, and the resistance of the rheostat R varies with temperature [53]. Up to this point, R has been considered constant, but to achieve better performances, the variation of R must be taken into account, measuring currents. Usually current measurements are not implemented by the train management systems; moreover, as mentioned before, the measurement of the chopper current is not a trivial task. In fact those currents have sharp edges and high frequency contents with simultaneously high levels of amplitude. This implies the adoption of expensive high performance current probes and even more expensive digitizer with sufficiently high sample rate. Instead, it is possible to identify a single sample per pulse that represent an estimation of the average current during the pulse itself. This can be achieved by adopting a low-cost analog peak detector, with a step response tuned on the time behaviour of the chopper signal, taking only one sample per chopper pulse. The chopper control circuit can trigger sampling after an opportune delay following the switch activation.

Defining the measured peak current as:

$$\hat{I} = V_\mathrm{R}/R \tag{3.29}$$

and using this quantity in the eq.3.27, a new formula for pulse energy evaluation is obtained:

$$E(\delta) = \frac{V_\mathrm{R}^2}{R} \cdot (\delta - \xi^*) \cdot T = V_\mathrm{R} \cdot \hat{I} \cdot (\delta - \xi^*) \cdot T \tag{3.30}$$

With this approach, the variations in the resistance value are taken into account because are reflected in the variations of $\hat{I}$

3.3.2 Application of the simplified energy estimation method to real test cases

In order to apply the proposed methods to real test cases from the afore mentioned measurement campaign, the input quantities for (3.27) and (3.30) must be estimated. Not all the quantities are directly available from measurement data. In particular, only voltage was measured directly, duty cycle and resistance are derived. In the following the calculation for each of the input parameters is explained in detail. Furthermore, statistics of the values obtained allow to evaluate the variability of the input quantities.

Inverters voltages measurements

The v_F and v_HF are measured directly as explained in section 2.2. Analyzing the rheostats currents i_RA and i_RB, it has been possible to identify all the chopper pulses over all the Italian measurement campaign (Section 2.2). A total of 7’866’069 pulses were collected and analyzed. For each pulses the average value of v_F and $v_\mathrm{F} - v_\mathrm{HF}$ has been determined. In Fig. 3.21 are depicted the PDF (Probability Density Function) of these two quantities as results of the conducted statistical analyses. As it can be seen from the figure, the two distribution are very close, with a little difference in the mean value. The variability of the voltages of the rheostats is due to the variability of the line voltage, which is divided almost equally on the two inverters. As you can see, the average value coincides with half of the chopper intervention threshold,

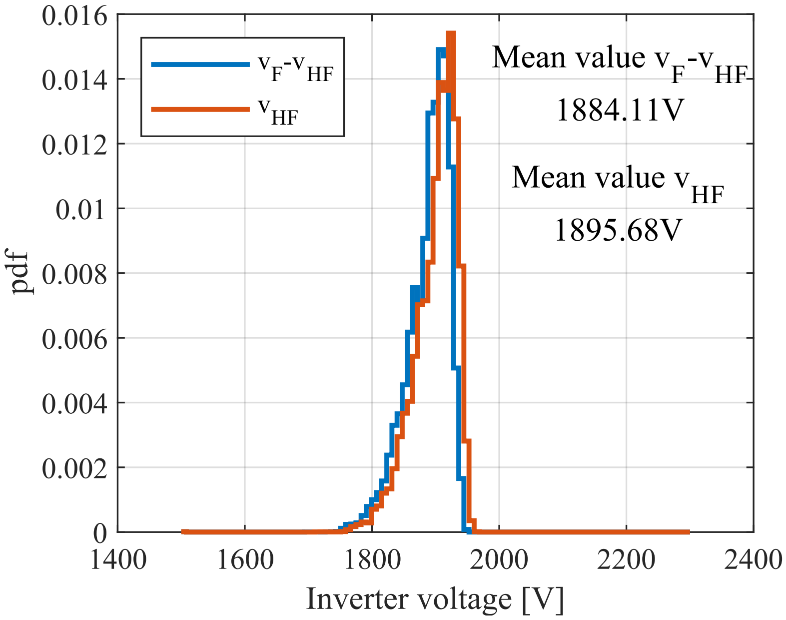

Fig. 3.21 Statistical analyses of the voltages applied to the inverters.

moreover voltage never overcomes 1950 V, in fact, as stated before, above 3.9 kV, purely dissipative braking is applied to avoid further voltage increase.

Duty-cycle estimation

As mentioned before, duty cycle should be known because it is imposed by the chopper. Unfortunately this information was not available at time of writing. For this reason it has been necessary to develop a technique to estimate the duty cycle.

A known duty cycle δ has been imposed to the same RL model of section 3.3.1. On the simulated signal, the duty cycle has been estimated, applying the Matlab *midcross* function. Obtained result obviously slightly differs from the imposed δ. Varying imposed δ in the range of interest, i.e. from 0.5% to 45%, with a 0.1% step, a set of results has been obtained. Then, adopting a curve fitting tool, an interpolation function has been obtained:

$$\delta = f(\delta_s) \tag{3.31}$$

where δ_s is the value of the duty-cycle estimated with the *midcross* method. This function (3.31) can be used to compensate *midcross* estimation. At this point, it has been possible to apply *midcross* interval estimation and successive curve fitting

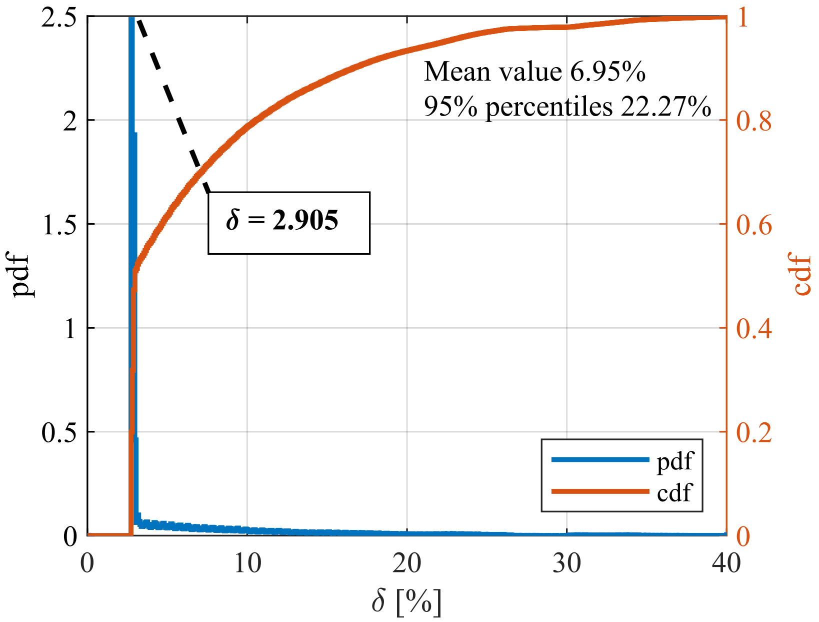

Fig. 3.22 Statistical analyses of the chopper duty cycle on the whole campaign.

compensation on the real measurement data for each chopper pulse. In Fig. 3.22 the PDF and the CDF (Cumulative Distribution Function) of the obtained results are reported. As it can be noted the duty never goes under 2%. This makes the assumption (3.26) always valid for the case of study. ξ is a constant amount equal to ξ^*, and the error due to this assumption is always 0.

Estimation of rheostats resistance and current

For the application of eq. 3.27 it is essential to accurately know the resistance value of both the rheostats. For the eq. 3.30 instead an estimation of $\hat{I}$ is needed.

The rated values of resistance for the considered locomotive are declared for 1.52 Ω with an accuracy of ± 5% in all operating conditions (see Table 2.1). Since it is not possible to metrologically characterize the rheostats positioned on board the train, the resistance values were calculated from the voltage signals v_{F} and v_{HF} and from the current signals i_{RA} and i_{RB}.

The resistance R_B was obtained by making the ratio between v_{HF} and i_{RB}, for each single pulse, in correspondence of current maximum value. The same is done for R_{A} considering i_{RA} and the voltage obtained as the difference $v_{\mathrm{F}} - v_{\mathrm{HF}}$.

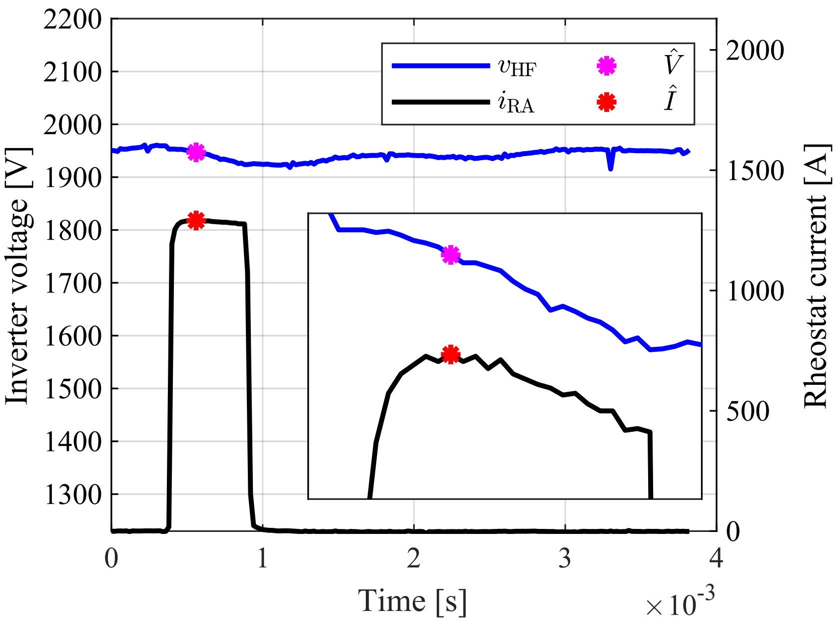

Fig. 3.23 Measurement points for the Resistance evaluation

When the GTO is turned on, a transient on the RL circuit starts. As long as the transient is not extinguished, there is a voltage drop across the stray inductance that reduces the current in the rheostats.

Taking advantage of the very wide bandwidth of Rogowski coils, which do not give rise to overshoot when a current step occurs, it can be assumed that just after the peak current the transient is extinguished, therefore this current is a good estimation of $\hat{I}$, the steady state value for this pulse. Moreover the resistance value for this pulse can be calculated as the ratio between voltage and current in correspondence of this point. Another transient on the voltage occurs when the GTO reopens the RL circuit and the current is supplied by the inductance that closes the circuit on the flyback diode.

In order to clarify the explained procedure, Fig. 3.23 shows the development of v_{HF} and i_{RA} signals for a pulse in which the points used for the resistance measurement are marked with asterisks, $\hat{V}$ and $\hat{I}$ for voltage and current respectively. Note that the current may not reach its steady state value, in case of short duration pulses. To avoid this problem only pulses with a duty cycle greater than 5% were considered for the resistance estimation.

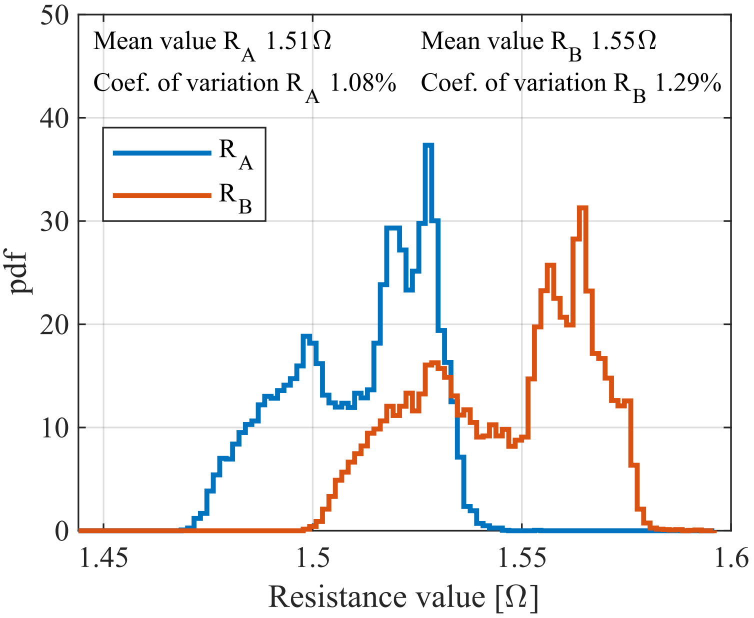

Fig. 3.24 Statistical analyses of the R_A and R_B values on the whole measurement campaign

For each rheostat Fig.3.24 shows the PDF together with the mean value and the CoV (Coefficient of Variation, defined as the ratio between the standard deviation and the mean value). The classes on which the statistics are made are 100 and uniformly distributed, for values ranging from 1.52 -5 % to 1.52 + 5 %.

The adoption of estimated mean value for R_A and R_B in the application of (3.27), greatly reduce the error on measurement of energy dissipated by the rheostats. The statistic shows how the values are concentrated in a very narrow range of occurrences, in particular the CoV is just over 1%, thus considerably less then the rated 5%. Therefore this greatly reduces the impact that resistance variation has on the performance of first method proposed eq. 3.27. Of course on the second method there is no impact due to the variation of R_A and R_B, thanks to the estimation of $\hat{I}$.

3.3.3 Comparison with reference estimation system

In order to assess metrological performances of the proposed methods the wasted energy estimation has been compared with a reference estimation system already presented in this thesis. The reference method is based on the determination of correction coefficient that allow to compensate the frequency response of the transducer and the previously described issue due to stray inductance.

According to [47], the reference energy for each pulse can be written as:

$$E_{\text{REF}} = \sum_{\text{k=1}}^{N} \frac{v_{\text{INV}}[k] \cdot i_{\text{R}}[k]}{fs} \cdot K_{\text{DC}}(f(\delta_s)) \cdot K_S(f(\delta_s)) \tag{3.32}$$

where:

- $v_{\text{INV}}[k]$ is v_{F} for R_{A} and $(v_{\text{F}} - v_{\text{HF}})$ for R_{B};
- $i_{\text{R}}[k]$ is $i_{\text{RA}}[k]$ or $i_{\text{RB}}[k]$;
- $K_{\text{DC}}(\delta)$ is a correction coefficient that compensate the error made by considering constant and non-pulsed voltage across the rheostats;
- $K_S(\delta)$ is a correction coefficient to compensate the transducer frequency response;
- $f(\delta_s)$ is the duty cycle estimated with eq. 3.31;

The expanded relative uncertainty with a confidence level of 99% of the reference method is estimated as 0.20%.

The energy measured for each individual pulse using eq. 3.27 and (3.30) can be compared to the E_{REF} trough:

$$\varepsilon_1 = 100 \cdot \frac{E - E_{\text{REF}}}{E_{\text{REF}}}, \quad \varepsilon_2 = 100 \cdot \frac{\hat{E} - E_{\text{REF}}}{E_{\text{REF}}} \tag{3.33}$$

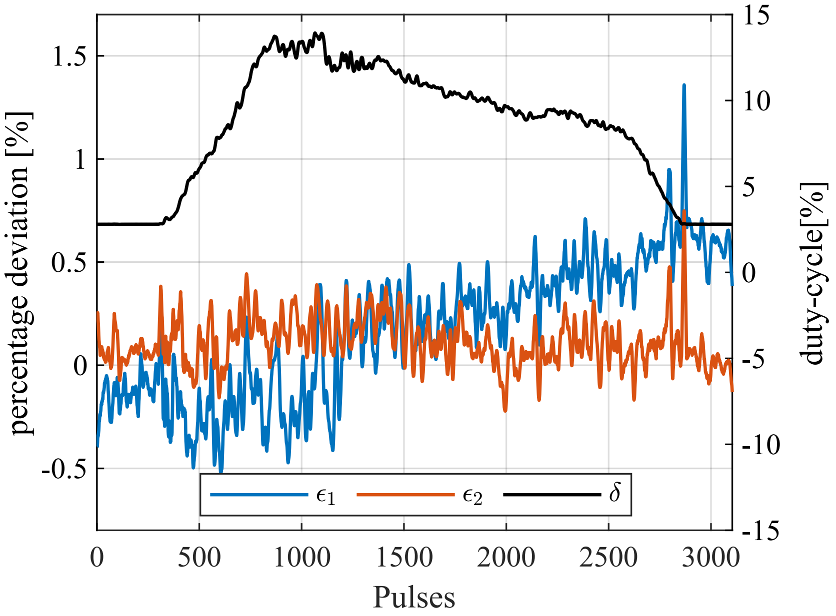

Fig. 3.25 Application to the railway journey from Bussoleno to Susa

For sake of brevity only 2 out of 78 routes from the measurement campaign have been selected to show the performances of the two methods. On the route from Bussoleno to Susa, there is only one braking arriving in Susa; Fig. 3.25 shows the results obtained on this braking. The percentage deviation ε_1 is depicted in blue, and ε_2 in red, calculated as eq. 3.33 for each chopper pulse, moreover the duty cycle estimated is reported in black. It can be seen that both method performs very well in this braking: the deviations maintain limited to 1.48% for the first method and 0.86% for the second; evaluating the deviations on the total braking energy, ε_1 is 0.14% instead ε_2 is 0.12%; finally the standard deviation computed over all the pulses is 0.34% for ε_1 and only 0.14% for ε_2. The heating effect on the rheostat can be appreciated, in fact the resistance increases during the braking, and, as a consequence, the ε_1 increases as well. As can be expected, the method eq. 3.30 is independent of the variations of R, the error of the latter has a lower variability.

In order to analyze this temperature effect on a longer journey with multiple braking, Fig. 3.26 shows the results obtained on the route from Alessandria to Voghera. The two deviations (ε_1, ε_2) and the duty cycle (δ) are depicted with the same colors. Note that obviously the train is not in braking stage for all the route, because the x axis is not directly the time, those three quantities are plotted versus

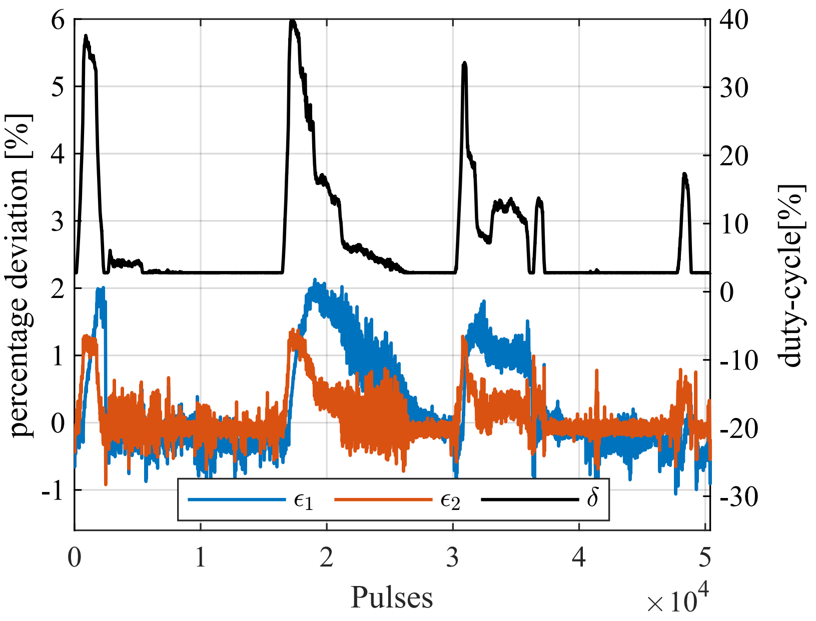

Fig. 3.26 Application to the railway journey from Alessandria to Voghera

the pulses, for this reason only the braking are reported, one after the other. On this route it is possible to see what happens during high dissipative braking, the duty cycle is greater than 30% multiple times. From the chart is evident that an increase in the duty cycle is followed, with some delay, by an increment in ε_1. The delay is due to the thermal transient of the braking rheostat. In the monitored locomotive the resistance has a variability of 1.08 %, which includes the thermal effect, already shown in Fig. 3.24. In fact the standard deviation of results obtained on pulses is 0.70%, moreover the error on the total braking energy is 0.69%.

As regards the second method, the performances are better (maximum error on single current pulse is slightly over 1%, standard deviation is 0.33%), nevertheless, for more dissipative braking ($\delta > 30\%$), ε_1 increases proportionally to duty. This is due to the fact that the current i_{RA} is not constant during the single pulse as it can be noted from Fig. 3.23. More in details i_{RA} decreases as the filter capacitance is discharging (v_{HF} decreases). Moreover the current decreases also because the rheostat is heating by Joule effect (thus the resistance is increasing). During the pulse with big duty cycle, the estimation made with $\hat{I}$ has a worst accuracy, but considering the statistical distribution of Fig. 3.22 it can be concluded that this condition is unlikely to occur, thus it has little impact on average error.

Chapter 4

PQ events experienced on board trains

The power quality issue is a relatively new topic in the railway world [54–60]. The grown interest is driven by technical and economic issues. The technical issues arise from the need to have a railway system even more sustainable, reliable and with high resilience. The economic issues are triggered by the liberalization of the railway market that has introduced two actors in the railway system: the infrastructure manager and the railway companies. The quality of the power exchanged between the two actors have economic and fiscal consequences. In this scenario, widespread monitoring of the railway and metro system performed both on-board and in supply substations can be not only a valuable tool for a much more predictive diagnosis of the entire railway electric system but also an economic tool to promote trains and supply system even more efficient [61].

On the other hand, the railway and metro networks supplied by DC systems are experiencing an important technical improvement. The need of maximizing the recovering of the energy generated during the electric braking of the trains has stimulated the development and implementation of new technical solutions to collect and reuse this extra energy. However, these techniques can lead to a worsening of PQ conditions by generating transient reversal of power flows [37, 6].

For these reasons, measurement tools for the monitoring of the ripple in terms of amplitude and frequency and algorithm for the detection and classification of transient events are the base for the monitoring of the power quality in order to perform the predictive maintenance, to assess the impact of the new supplying architecture in terms of compliance with the EMC limits and to verify the energy efficiency improvement.

The scientific research on the PQ in railway system is mainly oriented towards the AC railway supply systems. Mariscotti has provided a relevant contribution to the PQ in both DC railway and distribution grids [54–56]. Suarez et all [57] have analysed the over-voltages produced by the braking rheostat for specific light trains with DC traction motors. Pons et all [58] have contributed to the investigation on over-voltages occurring at the Tram network of Torino (Italy). Diez et all have analysed the power quality of the Medellin metro system with the aim of cataloguing the over-voltages according to their nature [59]. An interesting review paper has been published by Kaleybar et all [60].

The research activity here presented enlarge the typology of PQ events found in the huge amount of data provided by the measurement campaigns performed both on-board railway and metro traction unit and in a railway substation. This chapter presents an identification of PQ metrics for DC systems and present, with a collection of transient events detected on board the Trenitalia E464 electrical locomotive for commuter service operating at 3 kV DC (see section 2.2) and on-board the S9000 electro-train operating on the lines of the Metro de Madrid network supplied at 1.5 kV DC (see section 2.3).

4.1 Identification of PQ metrics for DC systems

Power quality is a well-addressed topic in conventional AC 50/60 Hz power systems and many procedures, algorithms and measurement systems were presented in the international standards and widely discussed in the scientific literature. A less explored research field is the assessment of the power quality in the railway traction supply systems, in particular with reference to DC and 16.7 Hz systems. It is therefore necessary to extend the definitions used for AC PQ measurements and of the standard measurement procedures (e.g. IEC 61000-4-7) for some of the main power quality indexes, which are well defined and widely used for conventional power systems, for them to be used in all railway traction supply systems. The table below shows rated voltage values for different railway systems as defined by EN50163:

Table 4.1 Summary table of metrics

Lowest non-permanent voltage	**Lowest permanent voltage**	**Nominal voltage**	**Highest permanent voltage**	**Highest non-permanent voltage**
U_{min2}	U_{min1}	U_n	U_{max1}	U_{max2}
V	V	V	V	V
400	400	600	720	800
500	500	750	900	1000
1000	1000	1500	1200	1950
2000	2000	3000	3600	3900

In general, a minimum sampling frequency of 5 kHz is recommended for all measurements. The choice of this frequency enables to measure up to at least the 50th harmonic in both 50 Hz and 16.7 Hz systems.

All the significant PQ index with the relative definition and description are reported in the following:

Magnitude of the supply Voltage

Mean value for 200 ms, 3 s, 10 minutes.

Overvoltage

The definitions for overvoltage are provided by the standard EN 50163. A summary of these definitions is given by the graph and table below. Three different zones have been highlighted; zone C, D and E. Zone C, which describes the admissible long-term overvoltage, start from an event duration of 20 ms (DC) or one cycle (AC) and stops at 1 s. The overvoltage limit curve is defined by the following formula:

$$U = U_{max2} \cdot t^{-k} \tag{4.1}$$

For a duration between 1 second and 300 seconds, the maximum allowed voltage is U_{max2} while for higher time duration the overhead contact voltage must not be higher than U_{max1}. The quantities U_{max1},U_{max2} and U_{max3} are referred to as the

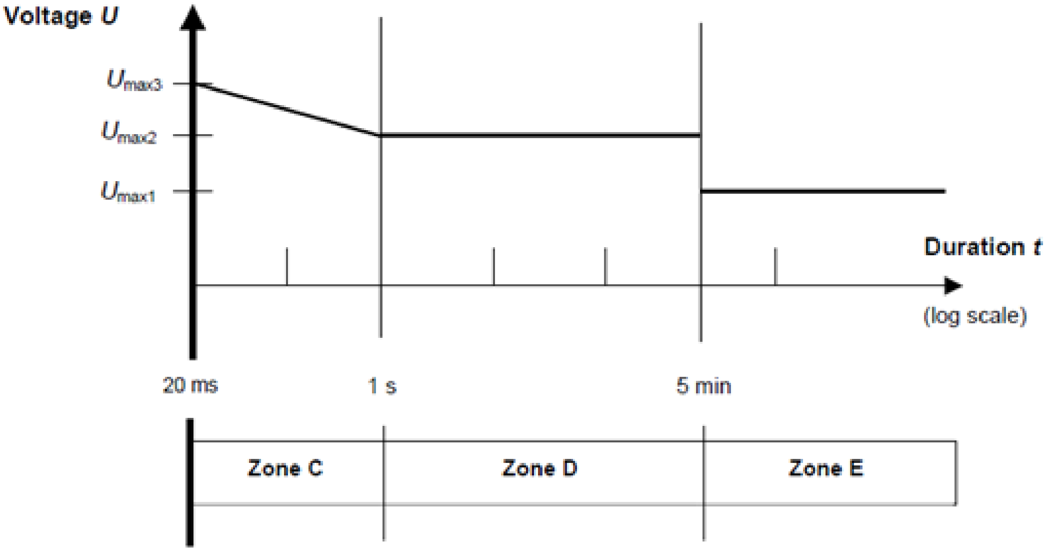

Fig. 4.1 Admissible overvoltage as a function of the time duration

highest permanent voltage, highest non-permanent voltage and highest long term overvoltage, respectively, and their values along with those for the constant *k* can be found in the tables below.

Overvoltages			
Nominal voltage U_n (V)	750	1500	3000
Coefficient k	0.0611	0.0676	0.0673
U_{max1} (V)	900	1800	3600
U_{max2} (V)	1000	1950	3900
U_{max3} (V)	1270	2540	5075

Table 4.2 Overvoltage limits

Undervoltage

The lowest permissible permanent and non-permanent voltages are given in the tables below.

Undervoltages			
Nominal voltage U_n (V)	750	1500	3000
U_{min1} (V)	500	1000	2000
U_{min2} (V)	500	1000	2000

Table 4.3 Undervoltage limits

Ripple

Ripple is the variation of voltage about the steady state value during steady state electric system operation. “Ripple amplitude is the maximum absolute value of the difference between the steady state and the instantaneous DC voltage.”

Steady state DC voltage is the time average of the instantaneous DC voltage over a period not to exceed one second.

Voltage interruption

An interruption is characterized by the complete loss of supply voltage. In the world of real measurements, the voltage is never exactly zero. Therefore, a threshold voltage V_{th} must be defined below which the supply voltage counts as interrupted for duration of time tint. The threshold voltage is set to 1% of nominal amplitude.

Table 4.4 Voltage interruption threshold for DC systems

DC system	$\mathbf{V_{th}}$
750 V	7.5 V
1500 V	15 V
3000 V	30 V

A voltage interruption can be:

- Short, if it last less than 2 seconds;
- Temporary, if it last between 2 seconds and 2 minutes;
- Sustained, if it last more than 2 minutes.

Voltage dip/swell

These begin when the supply level falls/rises below/above a certain threshold V_{th} and ends when the voltage rises/falls above/below the dip/swell threshold plus the hysteresis voltage V_h. (The purpose of this hysteresis is to avoid counting multiple events when the magnitude of the parameter oscillates about the threshold level). The window size for evaluating the supply level for dips/swells is 1 cycle or less. Characterize: duration and the minimum/maximum voltage magnitude during the event. By also inspecting the current signal it is possible to identify network interruptions (see https://ieeexplore.ieee.org/abstract/document/8897765)

Table 4.5 Voltage dip/swell threshold for DC systems

Nominal voltage	$\mathbf{V_{th}-/V_{th}+}$	$\mathbf{V_h}$ **(2% of nominal voltage)**
750 V	500 V / 900 V	15 V
1500 V	1000 V / 1800 V	20 V
3000 V	2000 V / 3600 V	40 V

Voltage impulse

This is a sudden high peak event that raises the voltage levels in either a positive or a negative direction. Impulses are categorized following zone B of Fig A.1 of EN 50124-2.

Causes:

1. Operating overvoltage as a consequence of reconfigurations of traction or main power supply network or ESD events
2. Arc event during traction/braking stage (DC)
3. Insertion, disinsertion of auxiliary loads in rolling stocks (DC).

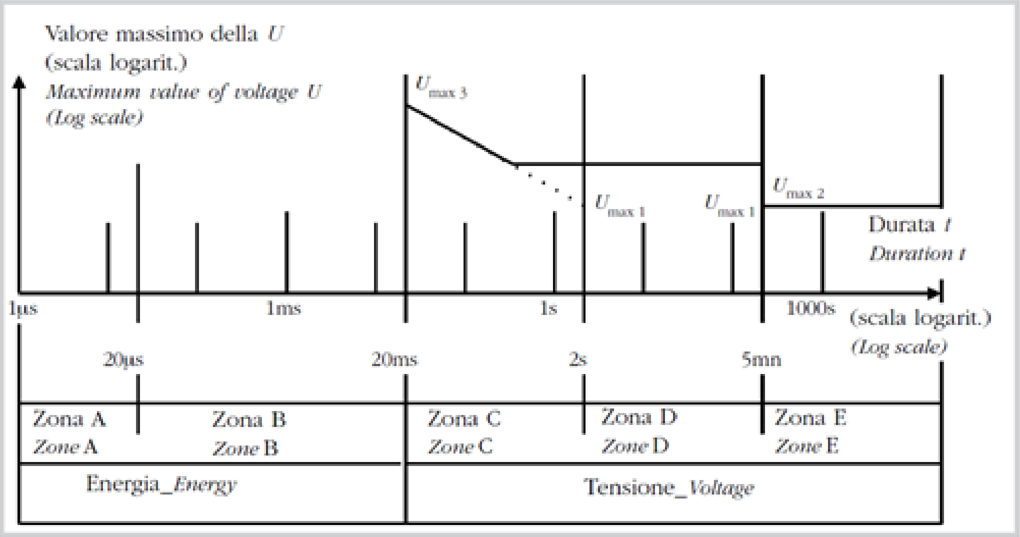

Fig. 4.2 Admissible overvoltage as a function of the time duration

Oscillatory transient

Sudden change in the steady-state condition of a signal’s voltage or current, oscillating at the natural system frequency. In AC, oscillatory transients usually decay to zero within a cycle. Causes:

1. Catenary resonances
2. Arcing phenomena

Spectral distortion

Distortion of the waveform by frequencies other than the fundamental (for AC) or by frequencies in general (for AC and DC). Integration time = 200ms No harmonic content but spectral pollution: sum of all the spectral components (V_h), up to a specified frequency index (h_{max}), and the reference value (V_{ref}), current accordingly. For the DC harmonic current, the algorithm is based on the limits defined by RFI and summarized in the following figure.

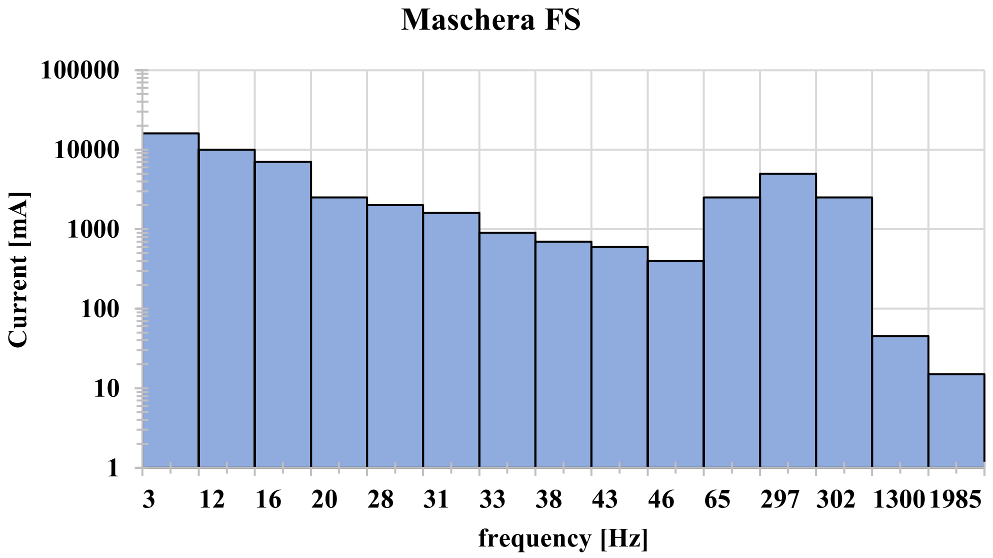

Fig. 4.3 Distortion limits defined by RFI

4.2 Collection of PQ events experienced on-board trains

From a deep analysis of data provided by the Piedmont and Madrid measurement campaigns, numerous interesting events and trends have been detected. For each of these is provided the measurement method and a brief description.

To give an idea of real analysed waveforms, Fig. 4.4 shows the voltage at pantograph and the corresponding absorbed current, measured on board the Italian train operating in a 3 kV DC system, during 5 minutes of Voghera to Alessandria route (25/01/2019,17:37).

As it can be seen from the figure, the level of voltage varies from a maximum of about 3708 V to a minimum of 3265 V and it is strongly related to the absorbed current that goes from a minimum of -430 A to a maximum of 1123 A. Negative currents are associate to regenerative braking. The mean voltage over the whole 320 s intervals is 3520 V, that is slightly lower than the maximum permanent voltage for this traction system (see Table 4.2); at each consistent increment of absorbed current, the voltage drops remarkably. As soon as the brakes were activated to reduce the train speed (time 66-72 s), the voltage increases, suddenly passing from 3265 V

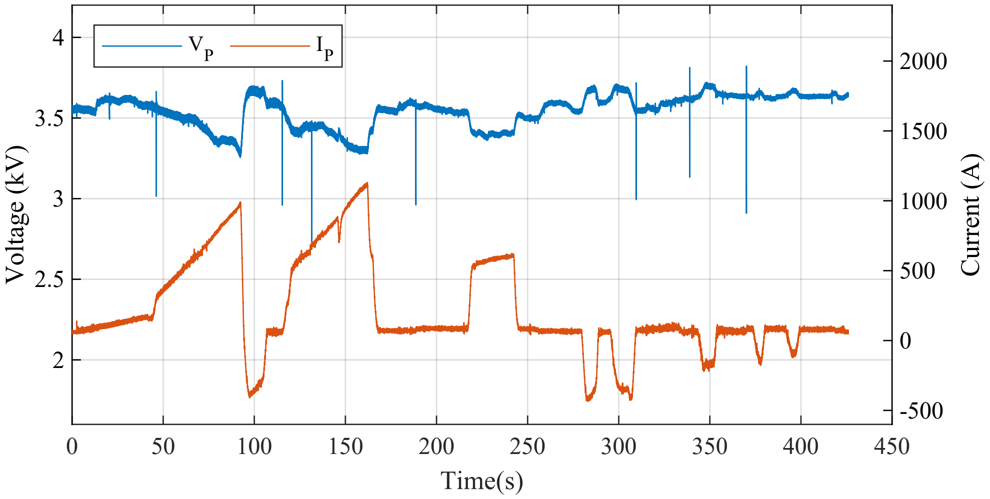

Fig. 4.4 Ordinary operating condition of a train in DC 3 kV supply system

to 3690 V. It is worthwhile noting that those harsh reported conditions have to be considered normal operating conditions for the railway systems.

4.2.1 Magnitude of the supply voltage

The first task of a PQ monitoring is the assessment of the supply voltage magnitude during different datetimes and different days, when no other PQ event applies. The statistical analysis of magnitude measured over “200ms” (e.g. 95 % probability weekly values, expressed in volt) gives information about the level of stress of all the devices supplied and it can be used for predictive maintenance purposes. Fig. 4.5 shows the statistical analysis of the supply voltages during all the monitored hours for the Italian campaign.

It is evident that all the most expected values are quite above the nominal value of 3 kV and the average value is even greater than U_{max1}. The standard deviation is few percentages of the mean values (about 120 V). The 95% percentile is close to 3.8 kV. The first class of histogram reports the occurrence of all the values less or equal to 2500 V. This is a comprehensive behaviour that can be used for the maintenance of the train, but it is interesting to show also the statistics of single route to highlight specific issues.

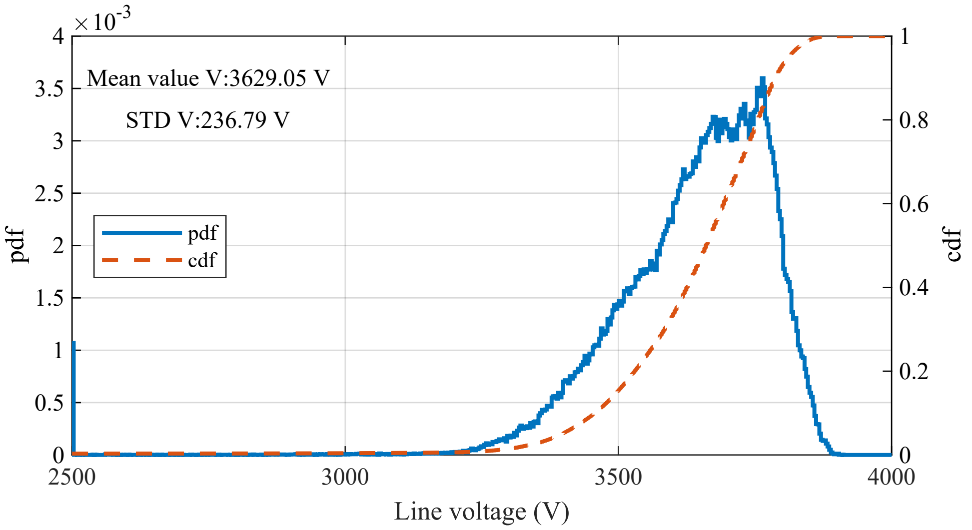

Fig. 4.5 Statistical analysis of supply voltage over all routes

Fig. 4.6 shows the results obtained for the route, with the greatest (a) and the lowest (b) standard deviation. The supply system of route from Alessandria to Savona (see Fig. 4.6a) seems to be somewhat undersized for rail traffic in the analysed period and this reflects on a lower average value and on a large variation of the supply voltage. Instead, the impact of absorption is very limited in the route from Novara to Domodossola (see Fig. 4.6b).

This is also the route with the highest mean value, that is higher than U_{max1}. If this situation persists over time, it would probably be necessary to change the configuration of the system to reduce the voltage level that is maintained at an unnecessarily high level. The route with the lowest mean value is reported in Fig. 4.7. This is a route with high difference in altitude between the two stations (about 1000 m) so large current absorption characterize this journey and this impacts on the average voltage. During the route 6 (Fig. 4.8) the greatest number of occurrences of voltage level below 2.5 kV was found. According to standard [17] the above-mentioned voltage levels are permitted.

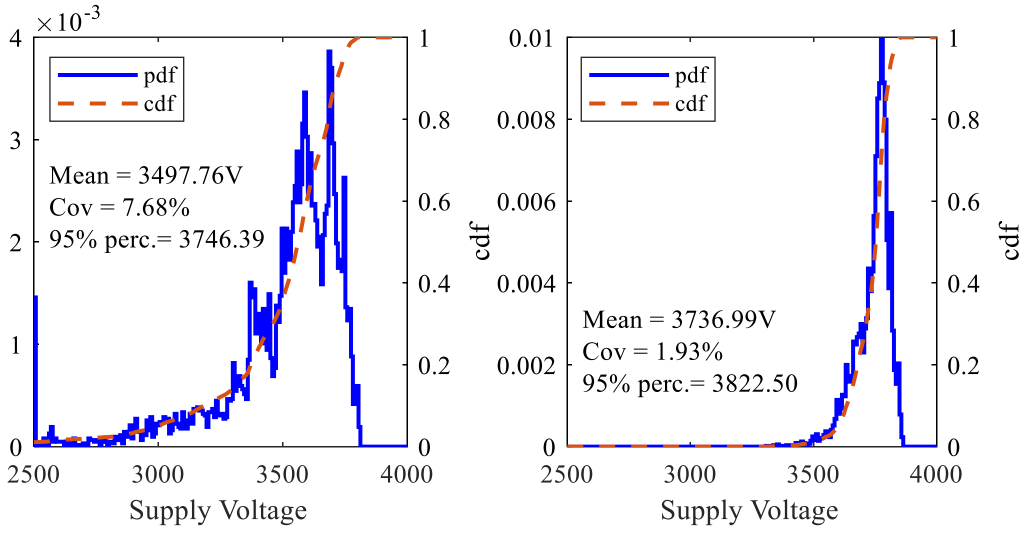

a) b)

Fig. 4.6 Statistical analysis of supply voltage on routes with the maximum a) and minimum b) voltage deviation

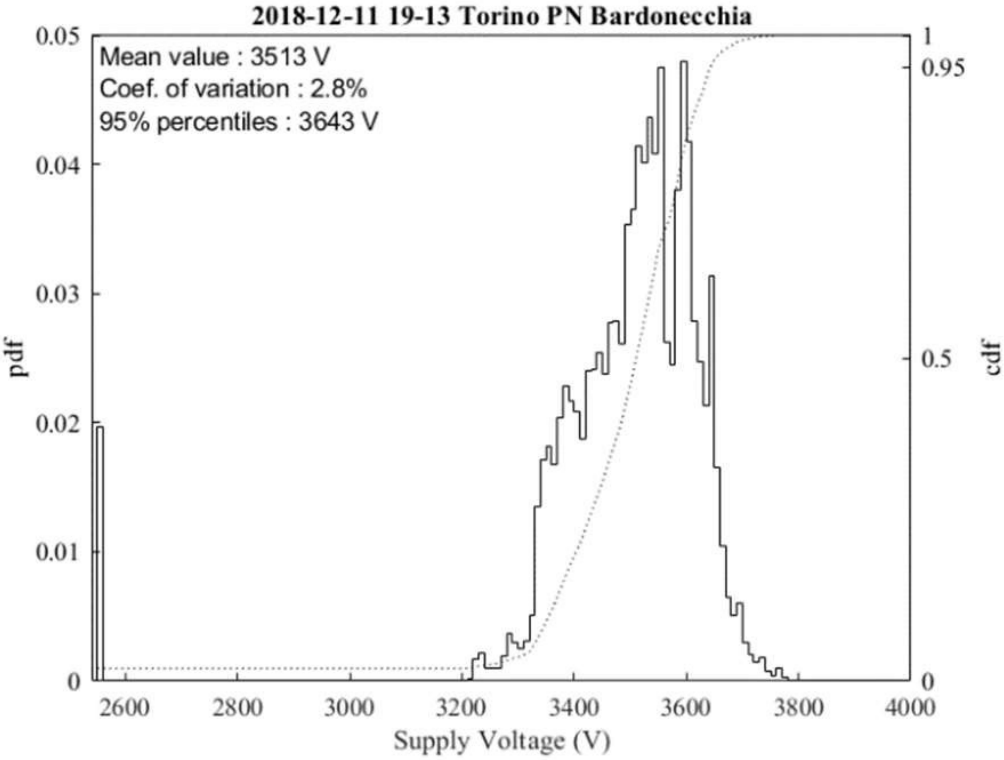

Fig. 4.7 The route with the lowest mean value

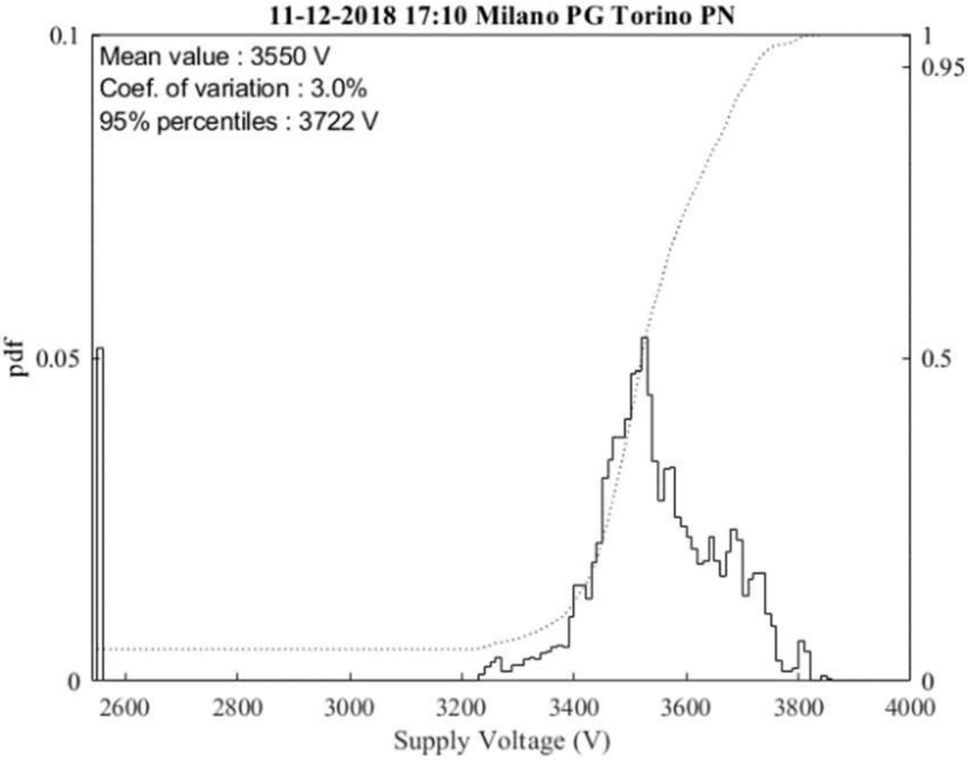

Fig. 4.8 the greatest number of occurrences of voltage level below 2.5 kV

Nevertheless, the availability of data recorded in different journeys on the same route allows performing a statistical analysis. The analysis, even though performed on limited samples, highlighted that the low voltage events are present in only one journey. The reasons of this behaviour could be a high current absorption from other trains or the out of service of a substation or both. This case demonstrates the importance of a continuous widespread power quality monitoring system that could help the infrastructure manager in detecting possible weakness of the supply system.

4.2.2 Voltage interruption

Ten interruption events were detected in the monitored period classified with the duration, T_d, as reported in Table 4.6.

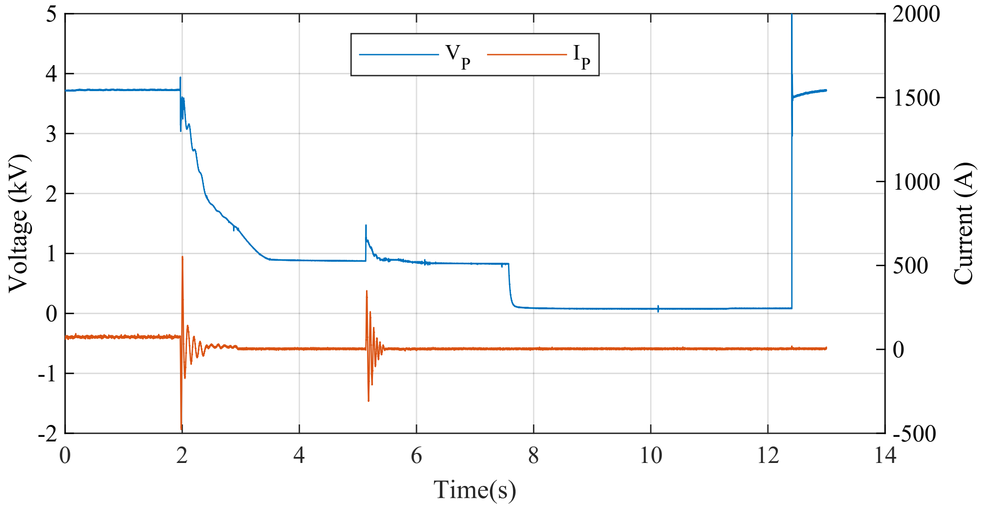

Fig. 4.9 Interruption during Acqui Terme - Alessandria route

Table 4.6 Voltage interruption tabled for time duration T_d

Duration, T_d,[s]	<10	10-60	60-180	>180
Number of occurrences	4	5	0	1

In the following, two of them will be reported and their main features discussed. In Fig. 4.9, it is apparent the voltage reduction that is not related with current absorption: the voltage drops under U_{min2} reaching the values of about 900 V. This event happens during a train stop because before the event the absorbed current is only that required by auxiliary systems (around 70 A). Note that the sudden voltage variations (at time 1 s and 4 s) induce a harsh oscillation on the current probably due to a resonance induced by the train second order input low pass filter. The second event is more interesting because there is no absorbed current before and after the voltage pulse. For this reason, the current oscillations can be considered not influenced by the load and caused only by the rapid voltage variation. Such a transient oscillation of the current from -304 A to +345 A is to be consider the normal behaviour of system. After about 5 s, a complete disconnection of the voltage applies, probably due to the protection breaker in the substation.

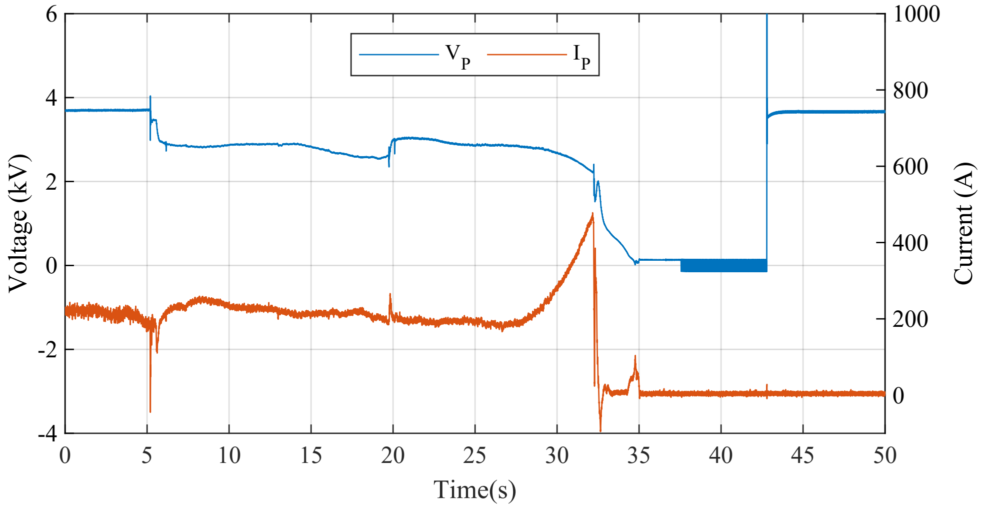

Fig. 4.10 Interruption during Alessandria - Savona route

In Fig. 4.10, at time 15 s, the voltage drops from 3700 V to 2900 V (time 15 s to 20 s) showing a weakness or overload of the supply line. Anyway, the level was not under U_{min1}, but, when the train accelerates absorbing about 480 A, the voltage suddenly drops again, causing a further reduction and then an interruption. This level of current was the same already reached before the event, (time 0-5 s), without significant voltage drops, confirming that the required electric power is no more available on the supply line.

4.2.3 Voltage ripple

Several analyses on the supply voltage ripple have been performed on both the railway and metro test cases. The analysis was performed considering successive periods of 200 ms duration.

For the railway 3kV DC system, an important event of power quality is the presence of the 300 Hz tone introduced by the hexafase AC/DC converter present in the substation. For the analysis of this tone a Fast Fourier Transform (FFT) operation was performed on successive periods of 1s duration. Fig. 4.11 shows the behaviour of the 300 Hz ripple along the Bardonecchia-Torino line; a greater amplitude is detected in the Bardonecchia station and decreases gradually towards the Torino station.

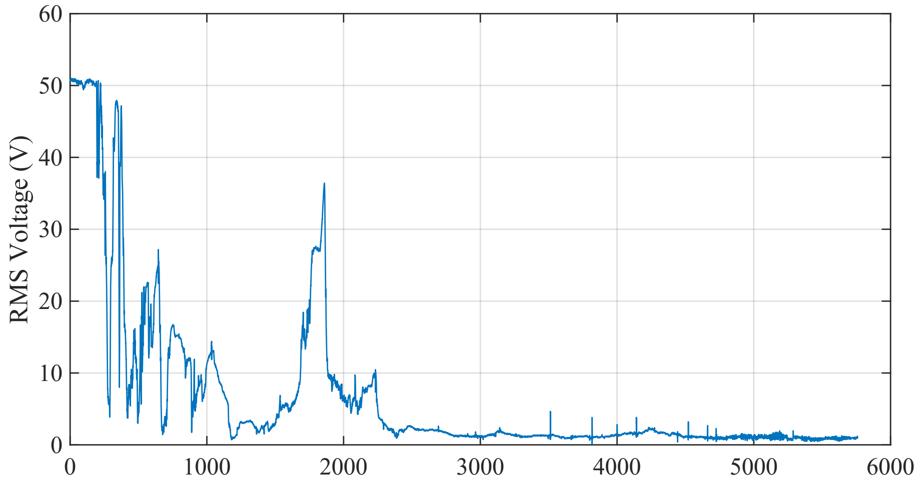

Fig. 4.11 300 Hz component of the route Bardonecchia - Torino

For the monitoring on metro system, this was performed on the line of Madrid 10B during a whole day with about 23 round-trip journeys recorded. In particular, the average values over one minute of the rms of the AC ripple are provided in Fig. 4.12. Compared the Italian railway case study, the ripple has a more stable behavior over time but is greater. It goes from 55 V to a peak value of 190 V. Since the ripple is a combination of several frequency tones superimposed to the DC component a frequency content analysis has been performed considering a time interval for the analysis of 200ms and averaged each second. The spectral analysis has been conducted considering the harmonics in a range that goes from 50 Hz to 3 kHz to evaluate the effect of the 12-pulse rectifiers installed in the substations that supply the line. An important PQ parameter is the presence of the 2400 Hz tone (see Fig 4.13a). In particular, the amplitude of the 2400 Hz tone as percentage of the DC component during the day is reported. Except for the first five hours in which the train is not yet travelling the line 10 B, it can be noted a time periodicity of the ripple. In fact, each peak around the 0.3 % occurs in a time-interval of about 49 minutes (see Fig 4.13b).

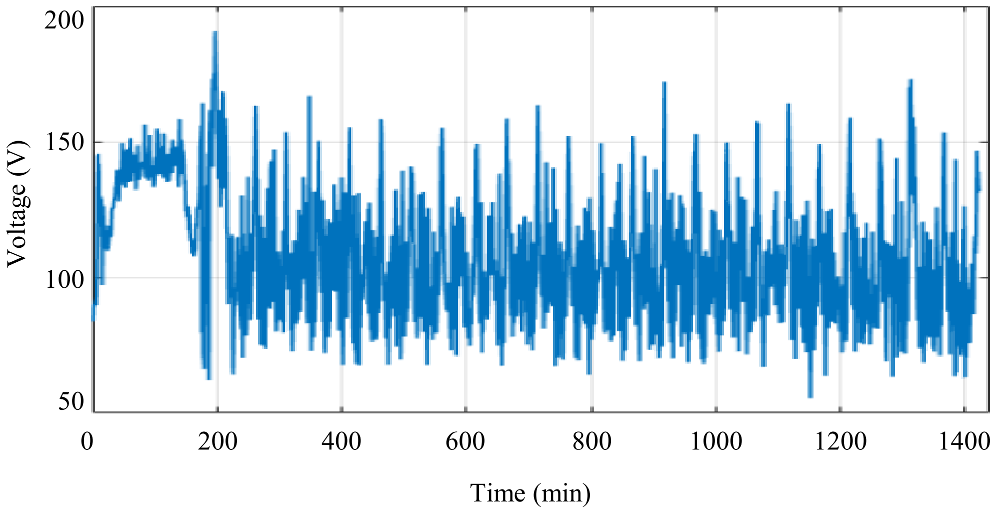

Fig. 4.12 rms voltage ripple for a day

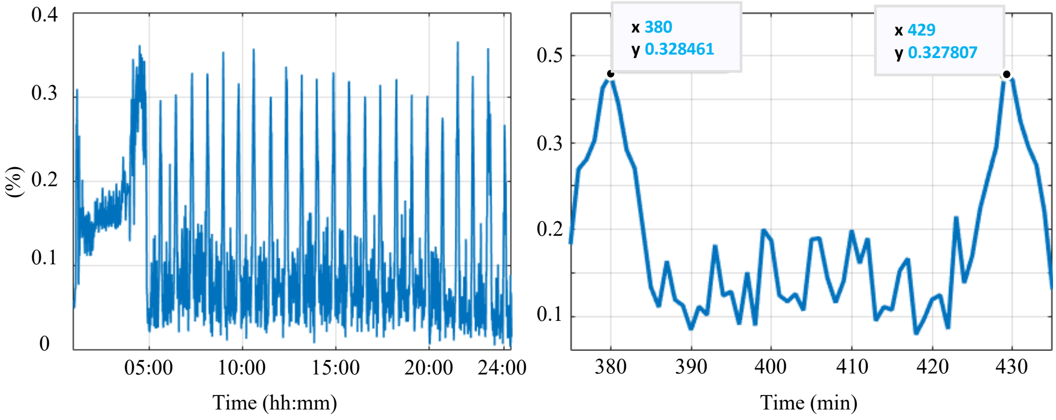

a) b)

Fig. 4.13 Behavior of ripple tone at 2.4 kHz for a working day a), with a zoom on single track time interval b)

Since the train is controlled through an ATO (Automatic Train Operation), the driving profile and the duration of each roundtrip journey is nearly the same and so the path traveled by the train as well. This is confirmed observing the traction current between two peaks of the 2400 Hz tone.

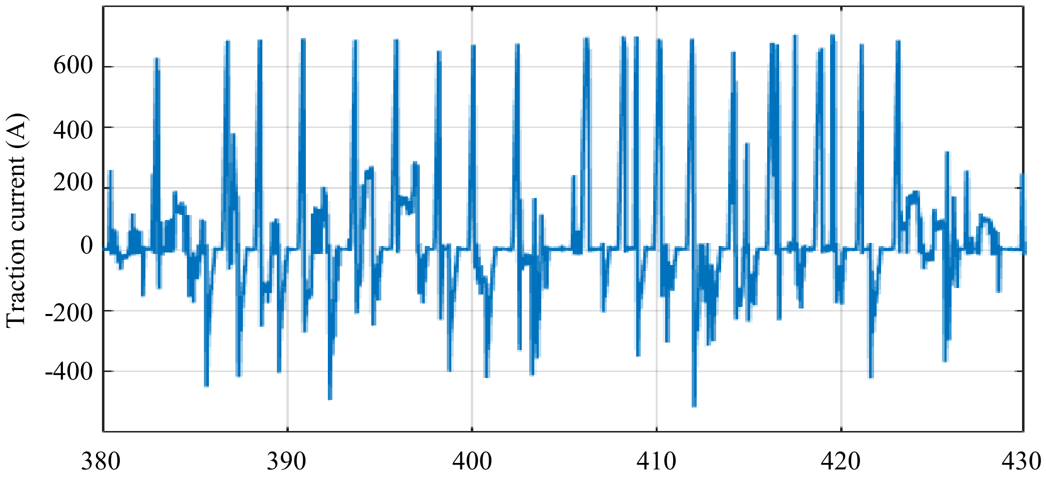

Fig. 4.14 Current behaviour of a round trip journey. The time from 380 min to 430 min corresponds to the same station

In fact, comparing Fig 4.13a, between minute 380 and 430 (see Fig 4.13b), with Fig 4.14b, in which is shown the traction current in the same time interval, it can be noted that the two peaks of the 2400 Hz component occur in correspondence of the same substation. It possible to argue that this PQ disturbance was originated in a specific substation so what before appears as time periodicity was instead a spatial periodicity: the level increases as the train is approaching to a specific station.

4.2.4 Voltage swell

In railway and metro systems, the voltage swell is a PQ phenomenon that can be attributed not only to the quality of supply: as explained before (see 1.1.1) the electric braking allows to recover the energy produced during the braking by delivering such energy to other trains or DC loads by means of the overhead contact line. This provokes a voltage increase (swell), which is higher at the pantograph of the braking train, so the voltage decreases along the line moving towards the load. The amplitude of the swell depends on the equivalent distance between the source and the load. To mitigate such overvoltage, a braking rheostat is connected in parallel with the traction units that become generator during the braking. A chopper modulates the amplitude of the current shunted by the rheostat in order to control the voltage level increase.

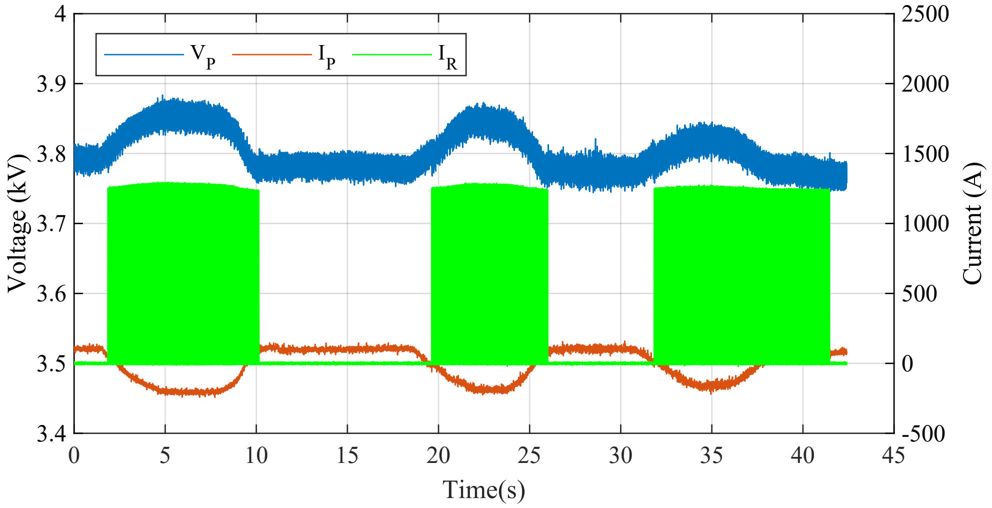

Fig. 4.15 Example of voltage swell due to the dynamic braking

An example of the electric quantities at the input of the traction unit during a braking is provided in Fig 4.15. Before the braking, the voltage experienced at pantograph was of about 3.5 kV while the absorbed current was of 1250 A. The driver suddenly sets a sharp braking; the voltage dramatically increases of 370 V; the voltage swell has an increase of 30% of the rated voltage (3 kV). Fig 4.15 also shows the chopped current shunted by the on-board braking rheostats that mitigates the swell.

Fig 4.16 reports the classification of the maximum voltage versus the duration of all the recorded swell events. The total number of events was 1989, but only 225 last more than 5 min and the maximum voltage reached is greater than U_{max2} in only 23 events. Almost all the events refer to stops at stations or braking events. For swell understanding, it is useful to see the corresponding current shape to distinguish between different situations: the stop at station is characterized by a nearly constant low current absorption for certain long time, the braking is characterized by negative current.

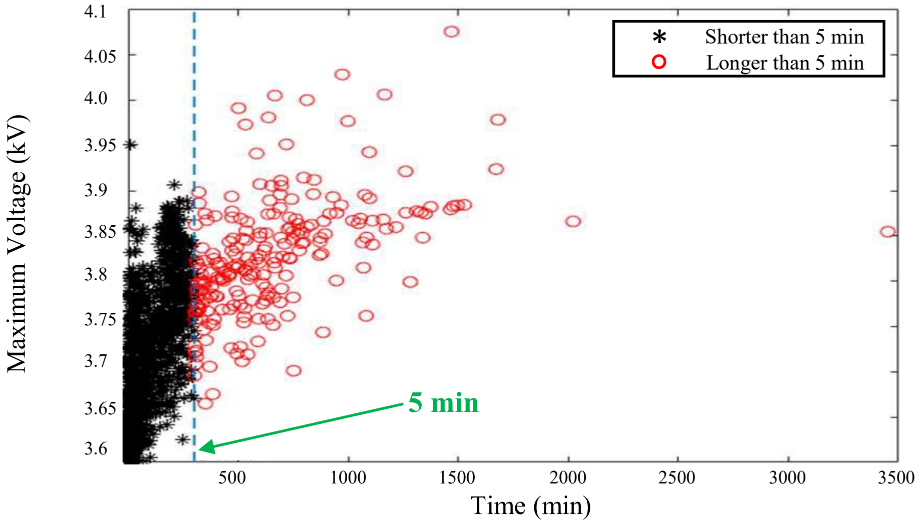

Fig. 4.16 Duration and amplitude of all detected swell

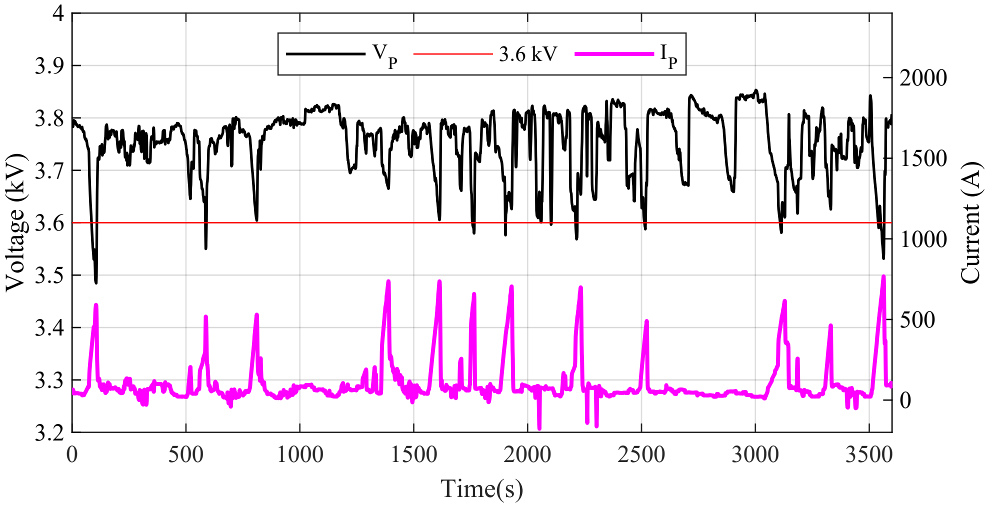

Fig. 4.17 Example of swell introduced by the supply system

Fig. 4.17 reports a swell event due a supply line overvoltage and not due to braking or presence of substation. The voltage for a quite long-time interval (about an hour) stay above U_{max1} even during the maximum of current absorption.

4.2.5 Voltage distortion

In [62], the distortion is evaluated by Fourier series expansion: each group of M samples forms a time window on which Descrete Fourier Transform (DFT) is performed; the window width T_N determines the frequency resolution $f_C = 1/T_N$ (i.e. the frequency separation of the spectral components) obtained in the analysis. Therefore, the window width T_N must be an integer multiple N of the fundamental period T_1 of the system voltage: $T_N = NT_1$. The sampling rate is in this case $fs = M/(N \cdot T_1)$ (where M = number of samples within T_N). The adopted window width is 10/12 (50/60 Hz systems) fundamental periods ($T_N \approx 200$ ms in both cases). To improve the assessment accuracy, the obtained spectral components are grouped obtaining reliable pollution indexes (harmonic and interharmonic subgroups) and deriving cumulative pollution index: THD, THDG [62]. The basic frequency ranges for measurement include components in signals (currents or voltages) up to the 40th harmonic order (approximately 2 kHz).

Obviously, the same approach can be used in motoring traction supply system at 50/60 Hz. Normal periodic disconnections, due to the neutral sections, prevent the adoption of an aggregation time interval longer than 3 s. Moreover, a flagging procedure has to be adopted to avoid calculating distortion in non-stationary conditions.

In DC there is no basic periodicity to consider, so it is meaningless to talk about harmonic and interharmonic pollution. Nevertheless, it could be useful to refer, also in this case, to 200 ms for time window. Therefore, it is possible to obtain components, groups and comprehensive indexes in similar way to that adopted in other systems but, in this case, it is more appropriate to speak generically about spectral pollution, including all the components. To this aim, as an extension of THD (defined in [62]), an index of Total Spectral Distortion (TSD) can be defined as ratio between the r.m.s. value of the sum of all the spectral components (Y_h), up to a specified frequency index (h_{max}), and the reference value (Y_{ref})

$$TSD_{\gamma} = \sqrt{\sum_{h=1}^{h_{max}} \left(\frac{Y_h}{Y_{ref}} \right)^2} \tag{4.2}$$

where the symbol Y should be replaced, as required, by the symbol I for currents or by the symbol U for voltages. The nominal value of voltage or current should be adopted as reference value, to avoid excessive fluctuation in the index value generated by the remarkable variability of the DC mean values.

Although there is no basic periodicity, even in DC system it is useful to have a specific index to monitor separately the pollution around 50 Hz. In fact, the presence of this component is particularly feared by the managers of the DC railway system as it directly affects signaling systems. For this reason, there is already present a specific monitoring device that alarms and disconnects the system when the level of 50 Hz spectral component reaches a prescribed limit level. To this aim, the eq. 4.2 should be modified to include only spectral components that are located at frequencies near to the multiples of 50 Hz. For formal definition, reference should be made to harmonic subgroups reported in [62].

For all the traction supply system, a not trivial task is to define the compatibility/immunity thresholds. However, there are already some amplitude levels for harmonic currents defined to ensure compatibility. Traditionally, the vehicle shall not exceed certain limits of harmonic current versus frequency (harmonic envelope). The harmonic envelope is normally defined with respect to signalling equipment [63] (see section 4.1).

The TSD_U has been calculated with a normalization to a nominal value $U_{ref} = 3000\ V$. Fig. 4.18a reports the statistical analysis of the TSDU over the entire measurement campaign. It is apparent that the level of distortion is quite low (below 0.55%) for most of time. Only in infrequent situations, distortion reaches remarkable values. To emphasize this aspect, Fig. 4.18b shows the worst measured statisticb for a single journey where the TSD_U level reaches some percentage.

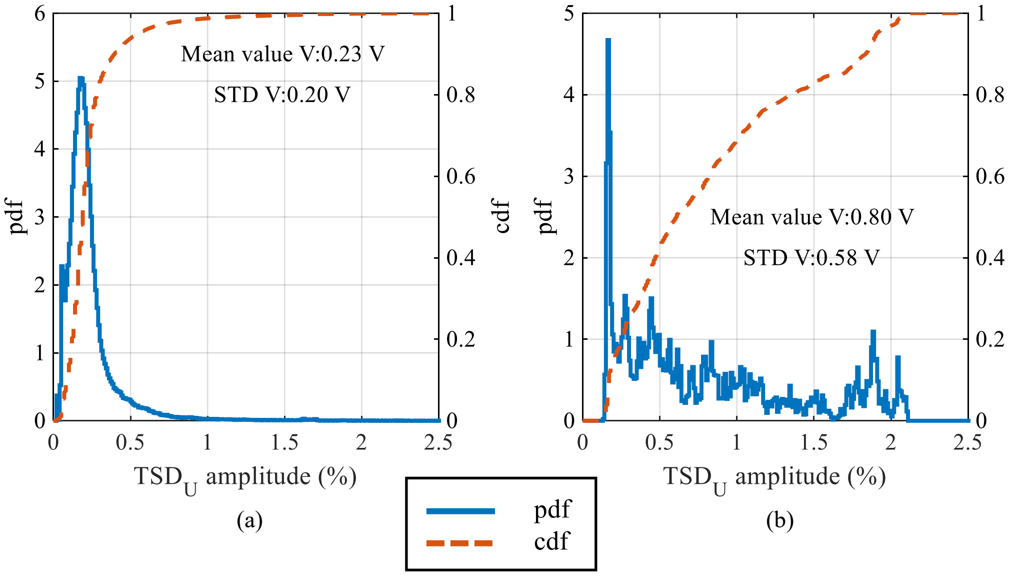

(a)

(b)

Fig. 4.18 TSD_U statistical analysis on the whole Italian measurement campaign (a) and the statistical analysis of the worst case recorded for a single journey.

Voltage transient

Fig. 4.19 provides an example of the amount of such fast transient events detected on one journey on the line Bardonecchia – Torino. As can be seen, voltage deeps of hundreds of volts occurs, in some case, even deep of one thousand of volt is detected. The reason of such events is under study. A correlation between some of these fast oscillation on the voltage at the pantograph with the current absorbed by the train has been found.

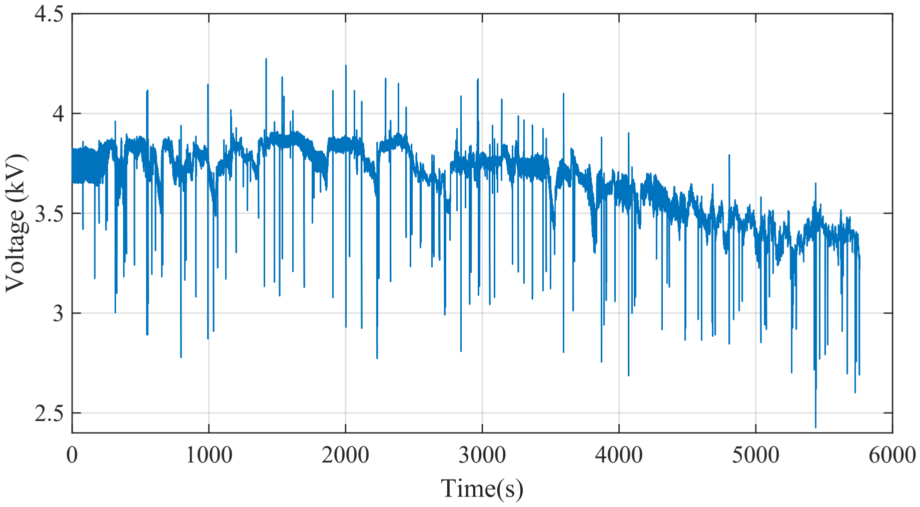

Fig. 4.19 V_P recorded during the Bardonecchia – Torino journey.

Fig.4.20 shows the occurrence of the transient oscillation on the voltage at the pantograph of about 1 kV of peak-to-peak of magnitude in correspondence of a step on the total current absorbed by the train of about 10 A – 15 A. This behavior could be introduced by the insertion of a filter of an electrical burden installed on board one of the coach carried by the locomotive.

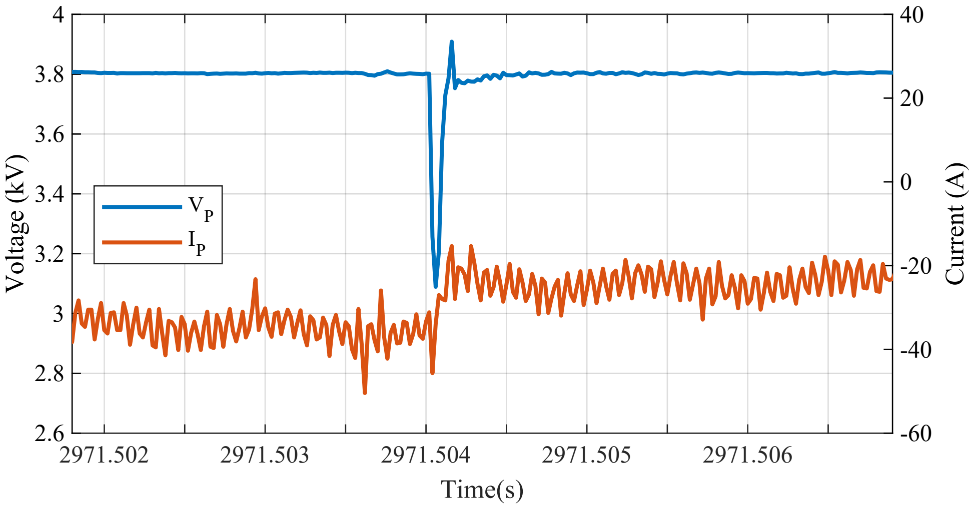

Fig. 4.20 Voltage and current at the pantograph during a fast transient event.

4.3 Electric arcs experienced on DC trains

Electric arcs are still nowadays an unavoidable by-product of the current collection by sliding contact in electrified transportation systems and are particularly intense for dc traction supplies. The power level is significant: up to several MW per sliding contact in railways with overhead contact line, lower in metros with third rail distribution that share at least one sliding shoe per coach. The power transfer from the OCL to the carbon blade of the pantograph during train movement occurs through a contact section of a few square millimetres. As soon as the current collection mechanism worsens due to imperfection of the geometry, defects on surfaces, temporary detachment, debris, oxidation, arcing occurs with air ionization and plasma conduction. The temperature increases to the melting point of materials and only train movement and air convection avoid the degeneration into an extended irreversible damage of surfaces or complete overhead contact line breakage.

Arc intensity and duration depends on several parameters characterizing the train: its speed, the intensity of the dc current, the traction or braking condition. DC railways in general (so encompassing all the metro, light railways, tramways, etc. using a dc supply) undergo more intense arcing due to two factors: the supply is a dc voltage of significant amplitude (between 600 V and 3000 Vdc nominal), and current intensity can be an order of magnitude larger than ac railways. DC arcs in electrified transports have been characterized in the literature in terms of voltage-current relationship [40, 64, 65], typical waveforms and their spectra [66, 55], and interaction with the traction line impedance and locomotive filter [54, 56], exploiting them also for network impedance estimate [67].

In general, arcs are well known as a source of high-frequency noise potentially affecting the quality and availability of telecommunication and signaling systems [40, 68].

The presence of arcs at the pantograph-overhead contact line interface (and similarly at the sliding shoe-third rail one) during traction is responsible for a first direct effect: the reduction of the available pantograph voltage V_P , since the arc voltage V_{arc} necessary for current conduction in plasma is in series with the line voltage V_l. Such reduction may in general cause a temporarily reduced train performance. Oppositely, arcs during braking increase the pantograph voltage due to the reverse flow of pantograph current [69], causing possible overvoltage issues.

Then, the arc conduction of the pantograph current I_P under a non-negligible voltage drop V_{arc} is responsible for a simple ohmic power loss, given by the product of the two quantities In addition, the electric arc as a broadband transient signal triggers the transient response of the traction network and train, causing the appearance of oscillations at the respective resonant frequencies, determined by the resonant filters at substation and onboard, and by the resonant modes of the line at higher frequency [54]. These components may disturb onboard metering and control [54], as well as signaling circuits connected to the track through the coupling of the return current [55, 70]. A not so obvious consequence can be identified during regenerative braking: when arcing occurs, due to the direction of flow of I_P, the value of V_P is further increased and larger than the pre-arc line voltage. Dissipative braking by means of the braking chopper feeding onboard resistors can in this case start due to momentarily excessive pantograph voltage, increasing conducted emissions and power losses.

At the detachment of the pantograph from the catenary (or equivalently of the sliding shoe from the third rail) an electric arc may establish through one or more plasma columns that allow the flowing of the current through the air gap. The electric arc is maintained as long as the combination of air gap and available voltage is compatible with current conduction; in other words the electric arc requires a minimum voltage that depends on the pantograph current intensity I_P and gap width.

Electric arcs as broadband transients can excite line resonances up to several tens of kHz (see Fig. 4.21), as shown in [54] using a parametric distributed-parameter model of the traction line and analyzing the components of the recorded electrical quantities. So, they are a relevant excitation source to probe the high-frequency portion of the line impedance and its resonance modes [67].

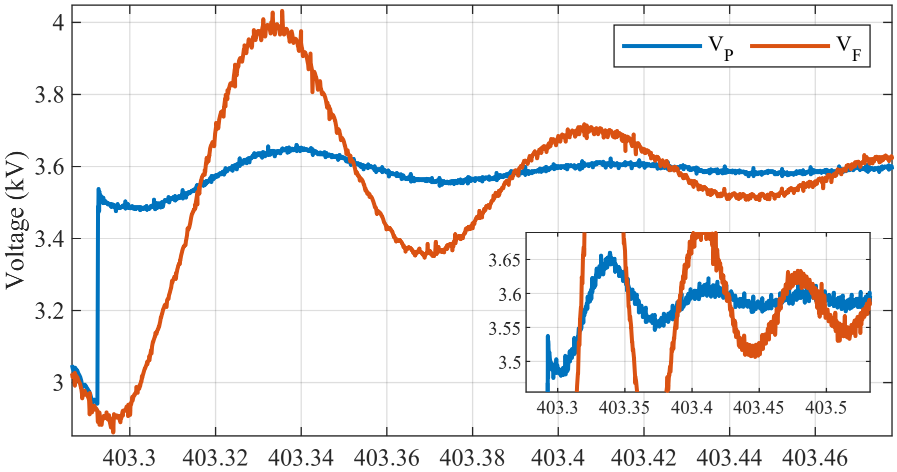

Fig. 4.21 Oscillations of the voltage V_P and V_F triggered by the re-establishment of the pantograph-to-line contact

The onboard LC filter is also excited by transients occurring at the pantograph interface, as well as by step loading during travel. Filter transient response occurs usually in the 12-25 Hz interval, determined mainly by the inductance and capacitance values of the onboard LC filter, although coupling with line and substation impedance (the latter featuring a similar LC output filter) can slightly modify the response. The large-value series inductor during the transient response behaves as a high impedance current source imposing an oscillating current in the I_P waveform and flowing along the line section. This behavior was analyzed in [54], identifying the conditions for the flow of current back to the substation through the rectifier diodes when positively biased by other trains pulling traction current within the same supply section. The absence of this condition prevents the flow through the otherwise reverse-biased rectifier diodes and causes anticipated arc quenching; at the successive I_P oscillation the arc can re-ignite if the pantograph detachment condition holds.

4.3.1 Arc event during traction

Two arc events are analyzed in terms of dissipated energy. The first event is shown in Fig. 4.22. The event is characterized by a voltage reduction of about 300 V and the absorbed current, because of the superposed filter oscillation, goes from 200 A to 0 A (arc quenching).

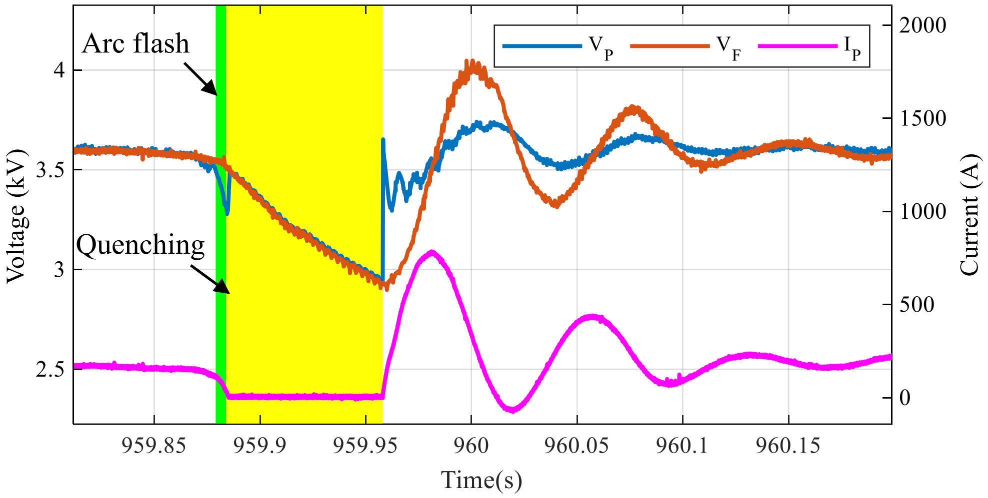

Fig. 4.22 Arc event during a traction phase and consequent quenching

The arc duration is about 14.9 ms while the quenching phase lasts for about 70 ms. At the end of the quenching the contact between the pantograph and the overhead contact line is re-established with a very fast increase of V_P, reaching again approximately the same amplitude before the arc event (about 3.6 kV). This voltage step, characterized by a slew rate of about 14.8 V/μs, triggers the filter oscillation at about 15 Hz. The average power dissipated by the arc, computed over its duration (14.9 ms) is 6.2 kW, corresponding to an energy of 93 J. For what concerns the active power associated with the oscillation phase, Table 4.7 summarizes the results for each of the first three oscillation periods: the active power terms are calculated by considering V_P and I_P and separating them into a dc and an ac component, assigning to the arc phenomenon those terms that include at least one ac component. The table also provides the dc power that the locomotive should have absorbed if the arc event had not occurred.

Table 4.7 Active power related to the 15 Hz oscillation (kW)

Calc. power term	period 1	period 2	period 3
full V_P x full I_P	1167	854	694
V_P (a.c. component) x full I_P	20.3	3.09	2.6
full V_P x I_P (a.c. component)	495.6	177.5	197.4
V_P (d.c. component) x I_P (d.c. component)	673.2	673.2	673.2

4.3.2 Arc event during braking

Fig. 4.23 shows the electric arc event during a regenerative braking where the energy is subdivided into a part of recovered energy used to supply other loads along the line and into a remaining part of energy dissipated by the braking rheostats. As previously mentioned, during the braking phase the arc voltage V_{arc} is negative; therefore, the voltage measured at the pantograph, V_P, will be larger than the line voltage V_l. In Fig. 4.23 the arc flashing phase, highlighted in green, is characterized by a voltage impulse of about 450 V rising in about 10 ms. In the same time span, the current decreases to zero, arriving at the arc quenching phenomenon, highlighted in grey.

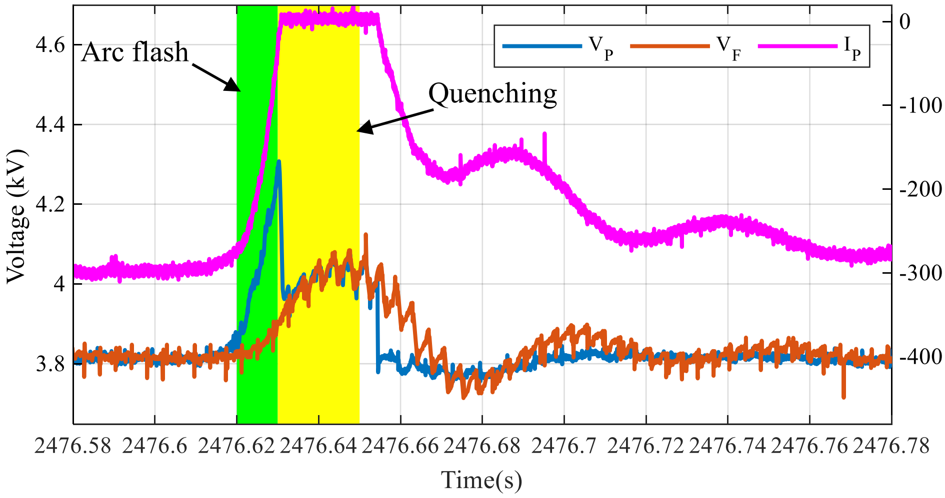

Fig. 4.23 Arc event during regenerative braking: details of arc flash and arc quenching with damped 15 Hz oscillation;

For about 25 ms, as for the arc during the traction phase examined in previous section, the current is zero and the voltage upstream (V_P) and downstream (V_F) of the filter are equal. As can be seen in Fig. 4.24, in this interval not only the braking type changes from mixed to purely dissipative, but the train control system increases the duty cycle of the chopped rheostatic current to counteract the increase of V_P.

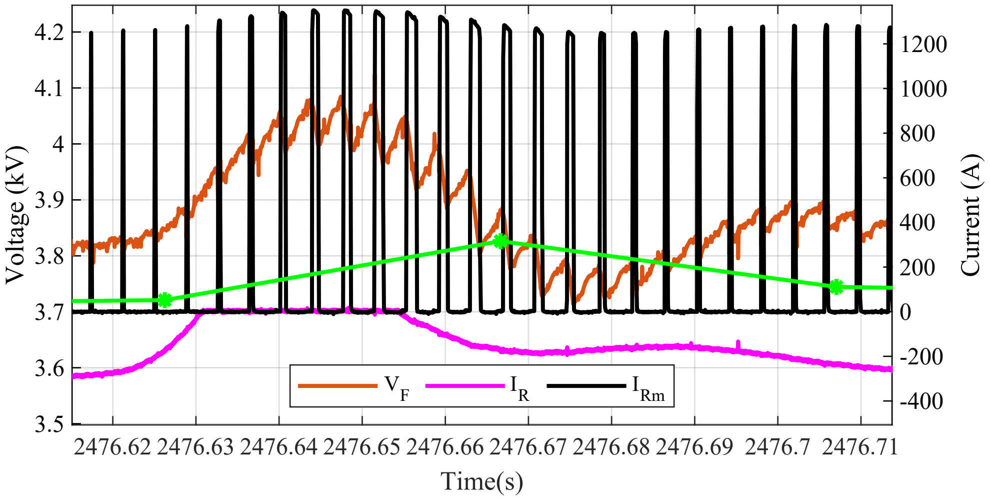

Fig. 4.24 Arc event during a braking: waveform of the dissipative braking chopper control superposed to voltage and current waveforms

In the phase following arc quenching, the pantograph voltage quickly returns to the line voltage, triggering the low frequency oscillation of the filter.

4.3.3 Methodology for the electric arc detection

Starting from the data obtained from the various measurement campaigns, it was possible to develop and verify a technique for the detection of electric arcs. The detection system exploits the conducted effects produced by the arc events to the railway supply system. This approach allows the use of the voltage and current transducer system already installed on-board the train for energy measurements or protection purposes. A consistent number of arc event can produce: fast degradation of the collector strip, increase of arc events, decrease of power quality and accidents. A methodology able to count the arc events without installing any other device on the train roof apart from the already installed voltage and current transducers can help the monitoring of the state of both the pantograph and the overhead contact line. A wide dissemination of such tool on-board every train associated with a data collection system can provide a valuable contribute in the predictive maintenance of devices involved in the sliding contact.

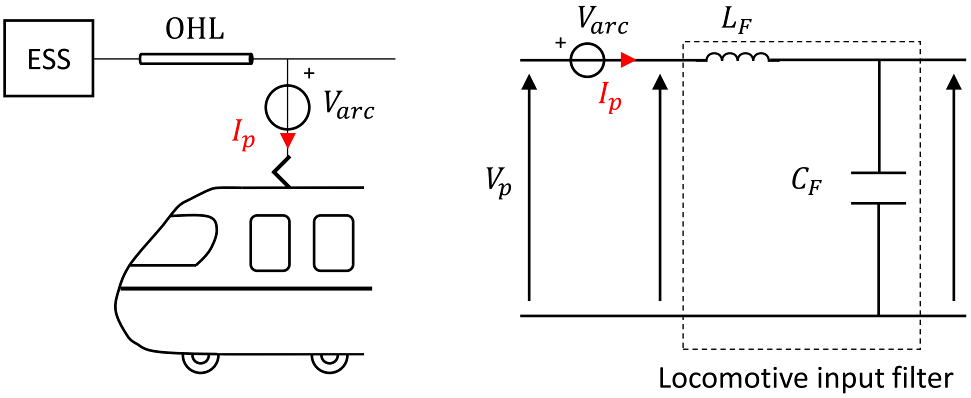

Fig. 4.25 Simple model of the arc occurring at pantograph that allows the understanding of the conducted phenomena produced by the arc

When a detachment between the pantograph shoe and the overhead contact line occurs in presence of a current flux, an electric arc arises between the two electrodes of the sliding contact. Despite the complexity in the physical description of an electric arc, for our purpose, such event can be easily described, in a circuital model as an arbitrary voltage generator that imposes an arbitrary pulsed voltage waveforms between pantograph shoe and overhead contact line. The Fig 4.25 provides a simple circuital description for arc events during the absorption (positive) or generation (negative) of current, the latter can occur during a braking stage. Fig 4.25 also shows the low pass input stage filter of the locomotive commonly present in DC locomotives. This filter plays an important role in the comprehension of the electrical conducted effects triggered by the arc.

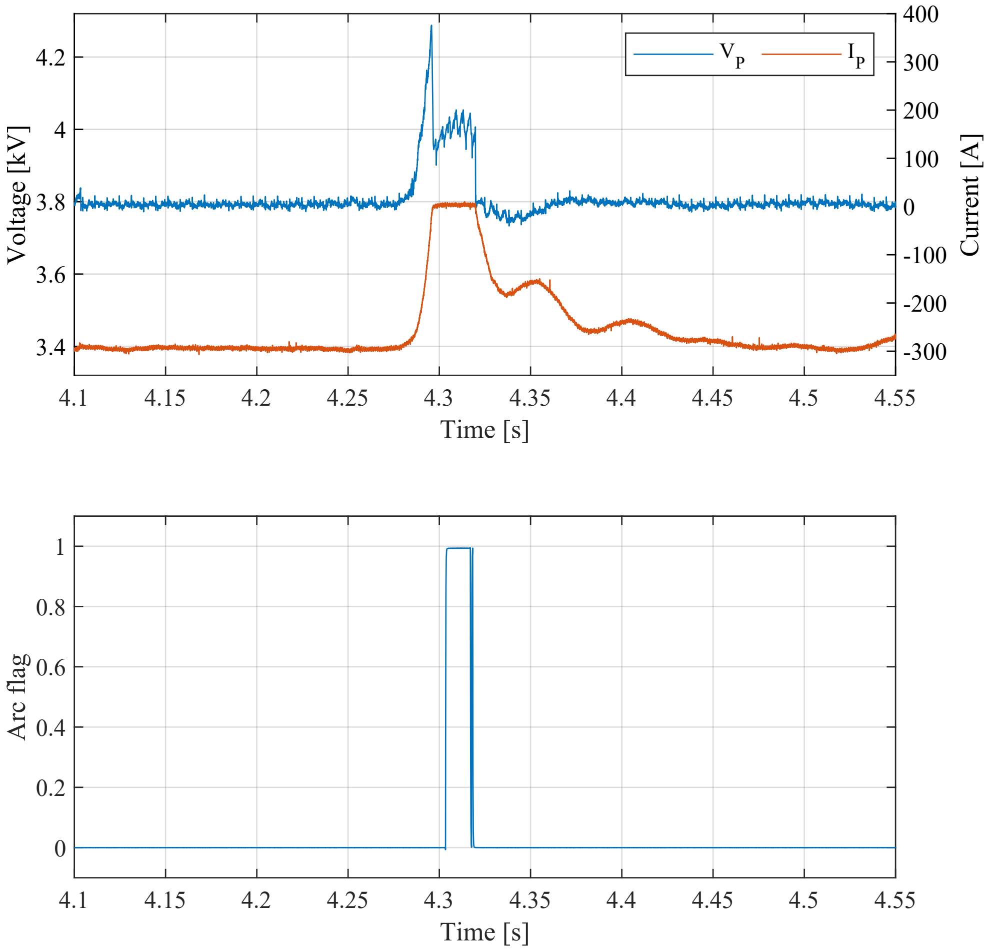

Fig. 4.26 Time behaviour of voltage and current at pantograph during an arc in braking stage (on the top) an time behaviour of the output flag of the detection algorithm (on the bottom)

The electric arc provokes a voltage dip in the voltage V_p if the locomotive is absorbing current and a swell if the locomotive is injecting current into the overhead contact line. Such fast variation induces an oscillation in the second-order low-pass filter that reflects on the current I_p. In detail, the current start to oscillate with a dumped behavior at the natural frequency of the filter. By exploiting the resonance of a specially designed filter, it is possible to easily detect the instants in which the oscillation on the voltage signal occurs and, by verifying the corresponding oscillation on the current signal, a hypothetical electric arc event is identified. The

Fig 4.26 provides the voltage and current during an arc event and the flag time behavior which is the output of the detection algorithm.

Chapter 5

The Phantom Power Calibrator

By 2019, the European commission requires that the billing for the energy consumption of the railway systems shall be computed on the actual energy consumed [20]. Until that date, there was no single regulation on pricing that was valid for all countries of the European Union but, typically, this was evaluated according to various parameters such as: the length of the rolling stock, the weight, the type of train, type of route, length of route, etc. This was mainly due to the lack of a continuous power/energy measurement system which, on the other hand, would allow the transition from this type of flat rate billing to a billing based on the actual consumption of traction energy.

In addition, the supply grid of the railway system, of course, is not ideal. It is strongly characterized by a non-stationary regime and many power quality events like harmonic pollution, electric arcs, dip, swell are verified during the normal operations. In order to evaluate the metrological reliability of an energy meter under actual operating conditions, calibration set ups and procedures which go beyond the well-known procedures developed for pure sinusoidal or continuous regimes are required.

Therefore, it is essential the realization of an accurate and reliable calibration system for evaluate the measurement of the energy absorbed/exchanged between the train and the railway grid, that takes into consideration the harsh on board measurement conditions and the frequent non stationary electrical conditions.

5.1 The Energy Measurement Function

For the porpoise of establishing a single European Railway Area that allows the free circulation of trains among the European nations, recent European regulations [21, 19] state that "all the train shall be equipped with an Energy Measurement Function (EMF), whose measurement accuracy has to be assessed and periodically verified". Before introducing the process that leads to its calibration, in order to have a clear idea of what actually is an EMF, here is reported the definition and description provided by the standard [20]. As shown in Fig. 5.1, the Energy Measurement System (EMS) on board the train is composed of an EMF and a Data Handling System (DHS). The EMF, in turn, is composed of:

- Voltage Measurement Function (VMF)
- Current Measurement Function (CMF)
- Energy Calculation Function (ECF)

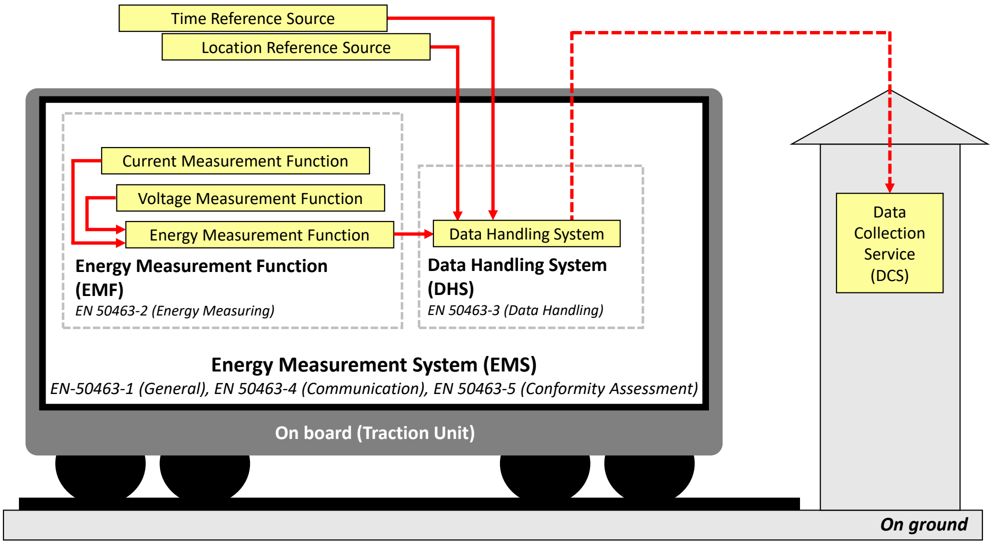

Fig. 5.1 Definition of EMF

These three functions can be implemented in one or more devices and their task is to provide respectively a measure of voltage, current and energy measured to the pantograph. The EMF provides energy data through an interface to the DHS. The

Table 5.1 Main characteristics of a commercial EMF.

Weight and dimension	• 12kg • 260 (H) x 410 (L) x 210 (D) cm
Input and Output	• Nominal line current: 1000 to 2500 A • Impulse Withstand Voltage: 40 kV – 1,2/50 µs • Maximum Current: 1200 to 3000A • ECF Current Analog Input Signal: -20/+20 mA • ECF Voltage Analog Iuput Signal: 0-20 mA • Current Accuracy: 0.5R • Voltage Accuracy: 0.5R • Energy Accuracy: 1R • Power Freq. Withstand Voltage: 20 kV/min
Line Voltage (Nominal DC)	• 750 V • 1.5 kV • 3 kV
Power supply	• Nominal 24 V DC to 110 V DC (wide range) • Power Consumption: 12 W @110 V typ.; 16W @110 V max

DHS elaborates the output of the EMF and, together with a Time Reference Source and a Location Reference Source, send these information in Data Collection Service (DCS) placed on ground through GSM communication.

Note that the communication between the outputs of VMF and CMF with the ECF is not standardized: it could be digital or analog, through current signals in scale ± 20 mA proportional to the input quantities. These implies that there are some EMF that allows the evaluation of the contributes of VMF and CMF on power error without considering the impact of the error introduced by the ECF. Table 5.1 reports the main characteristics of a commercial EMF.

Finally, it is important to remark that the EMF are active devices that need the simultaneous presence of both voltage and current signals. In fact, for safety reasons, if there is no voltage applied, the current sensor is not enabled. This means that an EMF may need a “real power" in order to be calibrated.

5.2 The Calibration System

5.2.1 The Phantom Power approach

One of the main aim of this thesis work is the realization of a calibration system for the EMF in DC railway systems. The calibration of an EMF under test is carried out by comparison with a standard system for the generation and measurement of electrical power. The EMF is a commercial device that allows to measure the energy and the power absorbed and delivered by the train during its activity and can work for different DC railway systems, from 1.5 kV to 3 kV (see Table 5.1), with current of rated line up to 2.5 kA. The system generally includes: a transducer for current measurement, usually a shunt; a transducer for voltage measurement, generally a resistive divider. The analog-to-digital conversion of the transduced signals can take place in the transducers stage or within the measurement unit (ECF). The calibration can be performed on the power data as the output of ECF, obtained with an average over generally 1 s intervals or on the power calculated on the output of the transducers section. Calibration can be performed on the ECF output power data, generally obtained with an average over 1 s intervals, or on the power calculated on the output of the transducer section. In the first case the measurand is actually the output of the EMF, in the second case the measurand is the output of the combined transducer that makes up the EMF. The error is defined as follows:

$$\varepsilon_{\mathrm{P}} = \frac{P_{\mathrm{EMF}} - P_{\mathrm{REF}}}{P_{\mathrm{REF}}} \tag{5.1}$$

In order to limit the power generated during the measurement the phantom power approach is used. This approach consists in applying simultaneously to the EMF under test a voltage and a current of a value equal to those found in the field but coming from two different amplifiers, each of which operating at almost zero power. The reference values of the voltage and current actually generated are measured by reference transducers. In case of combined transducer, two shunts are needed to transduce the analog output, composed by two currents, into two voltages for being collected by the acquisition system.

In details, in order to apply a phantom power type approach and to implement an admissible electrical configuration that do not put the operators and the instrumentation in danger, it is necessary that the common mode voltage on which the

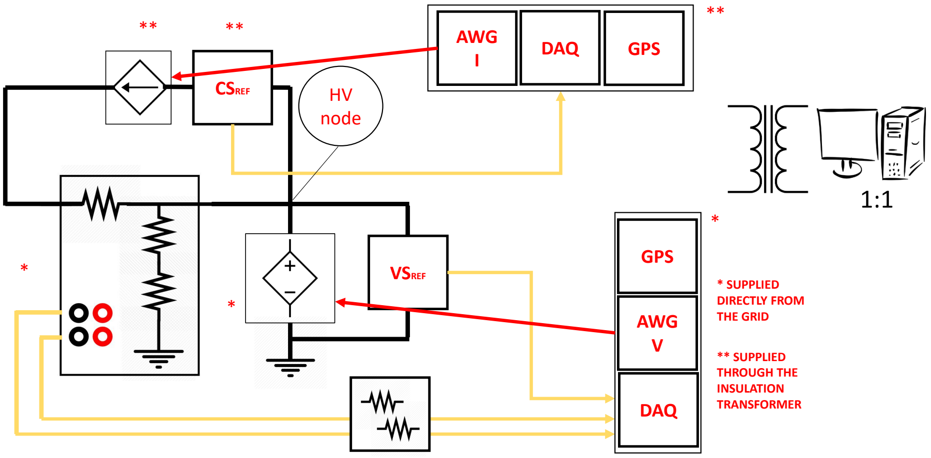

Fig. 5.2 Connection diagram of the Phantom Power Calibrator

current amplifier and the current reference work, is not higher than the maximum insulation voltage allowed for each of these instruments. The common mode voltage is imposed by the voltage amplifier and corresponds to the pantograph voltage.

To overcome this difficulty, the generation system has been divided into two independent sections, one for voltage and one for current (Fig. 5.2). Each section is composed by an amplifier, a reference transducer and control system. The current section is powered through an isolation transformer, that is a transformer with a 1:1 ratio and a very high isolation voltage between primary and secondary. At secondary of this transformer, the ground terminal is not connected to the real ground terminal but to the high voltage node; in this way, at secondary, the voltage between the reference terminal and new ground terminal is zero, but both these terminals are floating, with respect to the ground at primary, at a voltage imposed by the voltage amplifier.

Both control system are equipped with an Arbitrary Waveform Generation (AWG) module for reproducing low-voltage signals that have to be amplified, a Data AQuisition system (DAQ) for collecting the output of the reference transducers and the outputs of the device under test. The problem with this configuration is the lack of time synchronization between the two sections because, using different hardware, the time references between the two generation systems and between the two acquisition systems are misaligned. For this reason, each control system is equipped also with synchronization module that allows the synchronization of both controllers to the same time reference, provided by the GPS signal.

It is important to note that thanks to the presence of AWG, it is possible to generate not only stationary waveforms but also to replicate signals acquired from real measurement campaigns. In this way the performance of EMFs not only in nominal conditions but also to emulate the real operating conditions can be evaluated.

However, the method refers to the calibration of power and energy meters in Direct Current (DC). These quantities are not currently registered in the database of the Bureau international des poids et mesures (kCDB). Consequently, no international measurement comparisons have been made at the moment.

5.2.2 Measurement setup

For the voltage generation, NF HV4321 has been used; this is capable of generate a voltage signal up to 10 kV in a bandwidth of 10kHz proportional to the low voltage input signal. The current is generate with two identical Sorensen SGX High Power DC Supply. Each of them can amplify a low voltage signal and reproduce a proportional current up to 1.2 kA in a bandwidth of 600 Hz. As voltage reference, resistive-capacitive divider, designed, realized and calibrated at Inrim laboratories, with an overall accuracy of 0.05% in the frequency range from DC to 5 kHz is used. The reference transducer for the current measurements is the LEM ITZ 2000-S FLEX ULTRASTAB; it can measure currents up to 2 kA in a range up to 500 kHz with an overall accuracy lower than 12 ppm. The transduced signal is still a current and it is converted into a voltage by a Fluke A40 current shunt (1 Ω, 10 ppm).

Each of the two control system are implemented with a PCI eXtension for Instrumentation chassis (PXIe) that allows to use high-performance modular instruments. The synchronization module used for this application is the National Instruments (NI) 6683H, that provides a GPS disciplined 10 MHz oscillator with an overall accuracy of 100 ns. In order to reproduce non-standard waveforms, the high-performance module NI 5421 (100 MHz, 16 bit, ± 12 V) is used as AWG. The DAQs are the NI 4462 (4 channels, 24 bit, 204.8 kHz).

Both the voltage current units are remotely controlled by a PC desktop thanks to the NI 8375 Remote control module that allow the galvanic isolation thanks to its optic fiber connection.

In the specific case of a combined transducer, the analog output signals provided by the device under test (± 20 mA currents) are measured thanks to Tinsley Standard Resistor, with an overall accuracy lower than 10 ppm up to 10 kHz.

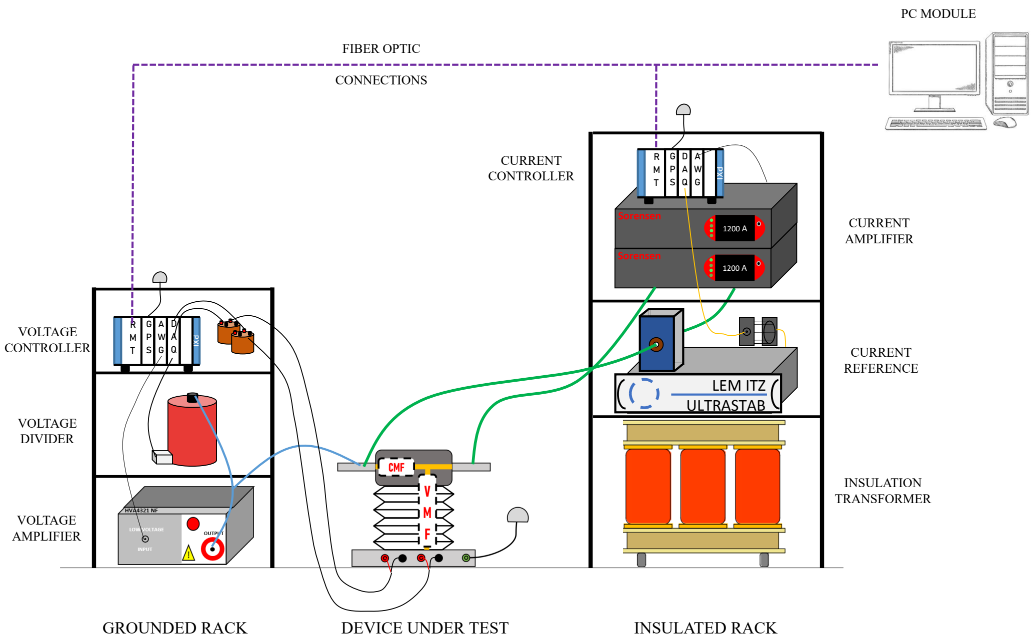

Fig. 5.3 Representation of the Phantom Power Calibrator setup

The system is capable of generating and measuring the voltage and current values reported in Table 5.2

Table 5.2 Generation capabilities of the Phantom Power Calibrator

Quantity	**Limit**
V_{min}	500 V
V_{max}	5000 V
I_{min}	5 A
I_{max}	2000 A

5.2.3 Calibration procedure

The calibration laboratory must be equipped with a temperature control system. Calibration is performed with instruments and transducers in thermal equilibrium with the environment for at least 24 hours. The environmental conditions in correspondence with the calibration operations are performed:

- Temperature: $(21 \pm 2)°C$
- Relative umidity: $(20 \pm 80)\%$

The measurand can be calibrated in two modes: stationary signal mode, dynamic signal mode. In stationary signals mode, constant voltages and currents are applied to the EMF under test, for 30 iterations of 1 second each, after a transient of 5 seconds. The amplitude values define a matrix of operating points, showed in Table5.3, in which the device will be calibrated. Considering the limits defined in [20], and according to the type of railway system on which the EMF operates, 4 voltage points and 12 (6 positive and 6 negative) current points are defined, for a total of 60 points.

The voltage operating points are the following:

- Nominal voltage $U_{\mathrm{n}} = V_1$
- Highest non permanent voltage $U_{\mathrm{max2}} = V_2$
- Lowest permanent voltage $U_{\mathrm{min1}} = V_3$
- Lowest non permanent voltage $U_{\mathrm{min2}} = V_4$

The current operating points are the $I_1 = 0.01 \cdot I_{\mathrm{n}}$, $I_2 = 0.05 \cdot I_{\mathrm{n}}$, $I_3 = 0.1 \cdot I_{\mathrm{n}}$, $I_4 = 0.2 \cdot I_{\mathrm{n}}$, $I_5 = I_{\mathrm{n}}$, $I_6 = 1.2 \cdot I_{\mathrm{n}}$ where I_{n} is the rated primary current.

In slowly variable dynamic signals mode, it is possible to test the EMF using voltage and current waveforms acquired in real measurement campaigns and reproduced in the laboratory. This type of verification aims to evaluate the performance of the device under calibration in real operating conditions and not in conditions of ideal stationary signals. In this case, the current can be both positive and negative during a test, therefore it is necessary to change the configuration of the two current amplifiers from the one shown in Fig 5.4a to the one shown in Fig 5.4b. Using the same equipment, the dynamics of the current signal is in the range [-1.2, + 1.2] kA.

Table 5.3 Calibration points needed by the standard

V_1I_1	V_2I_1	V_3I_1	V_4I_1
V_1I_2	V_2I_2	V_3I_2	V_4I_2
V_1I_3	V_2I_3	V_3I_3	V_4I_3
V_1I_4	V_2I_4	V_3I_4	V_4I_4
V_1I_5	V_2I_5	V_3I_5	V_4I_5
V_1I_6	V_2I_6	V_3I_6	V_4I_6
$-V_1I_1$	$-V_2I_1$	$-V_3I_1$	$-V_4I_1$
$-V_1I_2$	$-V_2I_2$	$-V_3I_2$	$-V_4I_2$
$-V_1I_3$	$-V_2I_3$	$-V_3I_3$	$-V_4I_3$
$-V_1I_4$	$-V_2I_4$	$-V_3I_4$	$-V_4I_4$
$-V_1I_5$	$-V_2I_5$	$-V_3I_5$	$-V_4I_5$
$-V_1I_6$	$-V_2I_6$	$-V_3I_6$	$-V_4I_6$

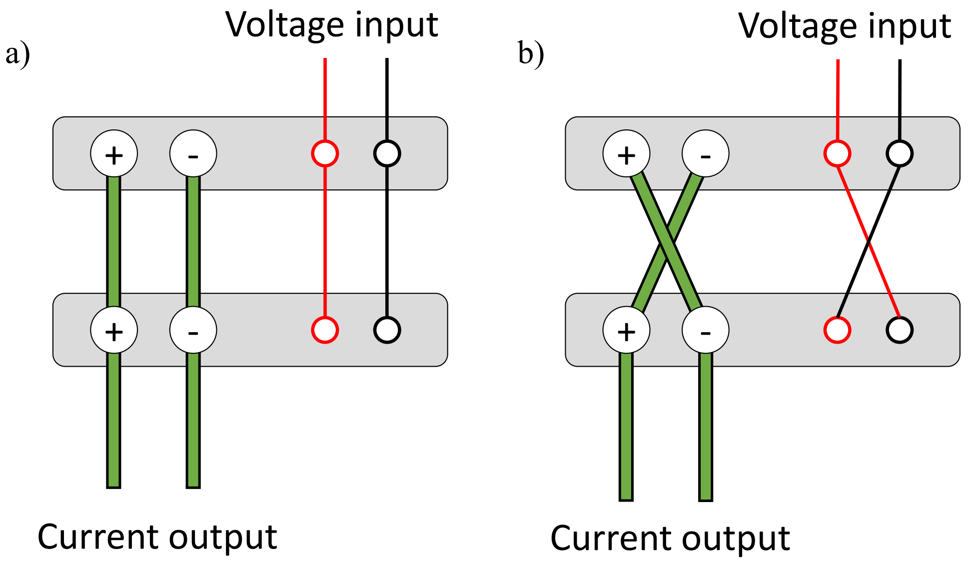

Fig. 5.4 Configurations for the current amplifier in static mode, a), and dynamic mode,b).

5.3 Systematic error compensation

5.3.1 The metrological traceability

Before proceeding with the calibration, it is important that the instrumentation used, the resistors, the acquisition systems and the reference transducers are calibrated, in accordance with what is indicated on the relative instrument sheet. In the following are reported the metrological traceability schemes for the calibration of the EMFs (see Fig. 5.5) and combined transducer (see Fig. 5.6). As already reported, the device under test can be a combined transducer, with analog outputs or the entire EMF. In the first case, it is necessary to transduce the current signals into voltage with compatible shunts previously calibrated in the laboratory. In the second case, it will be necessary to make a comparison with the measurement data obtained directly in digital and temporally referred to the GPS signal. It is also necessary to make sure, before the start of the test, of the actual presence of the GPS signal. This operation is automatically managed by the calibration software, which interrupts the measurement in case of lack of the synchronization signal during the test.

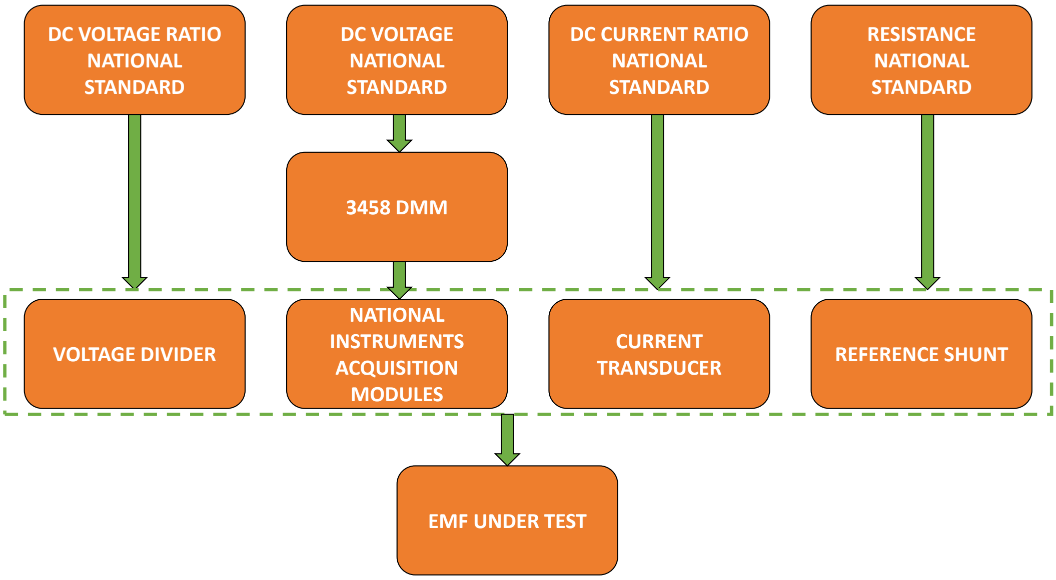

Fig. 5.5 Scheme of the metrological traceability for the calibration of EMF.

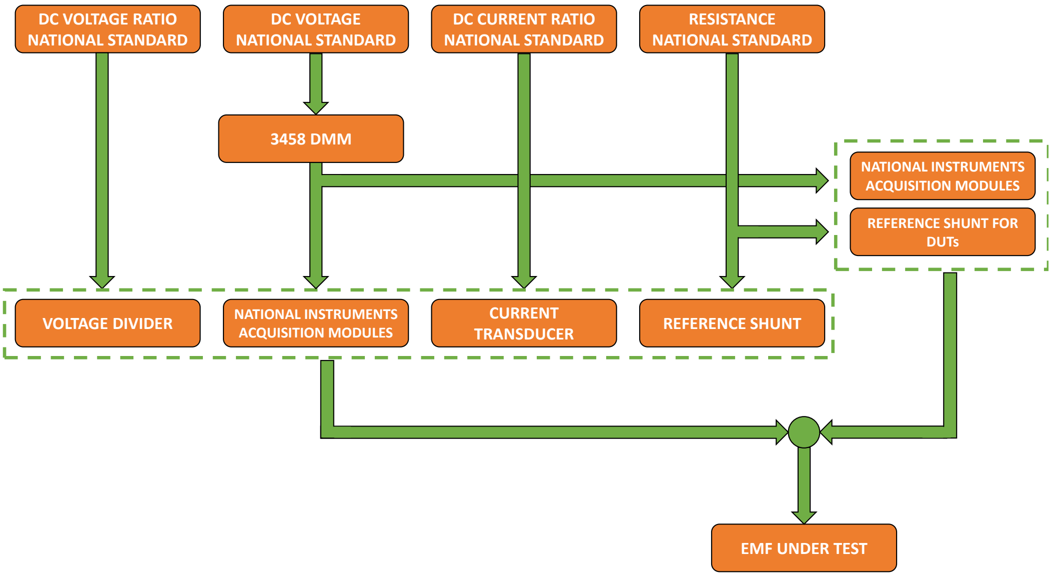

Fig. 5.6 Scheme of the metrological traceability for the calibration of a combined transducer.

5.3.2 Calibration of acquisition channels

Before starting the calibration of the measurement system, the calibration of the channels of the acquisition modules is performed. In order to estimate the scale factor of the acquisition channel and its offset, a Fluke 5500 calibrator is used to generate the continuous and stable voltage and a Keysight 3458A multimeter measures the voltage applied to the acquisition channel under test (see Fig.5.7). The characterization operations are automatically handled by a Labview software that controls both generation and acquisition. Finally, a MATLAB script determines the scale factor and the offset of the considered channel.

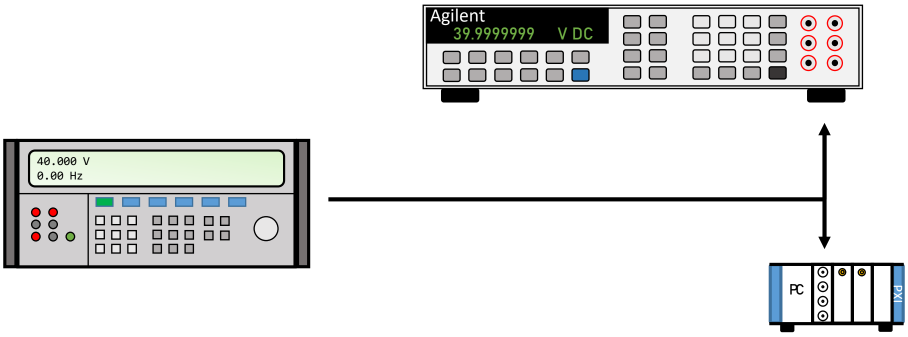

Fig. 5.7 Acquisition channels calibration procedure.

More in detail, for the characterization of each acquisition channel used, the scale factor and offset are estimated by applying, in sequence, a constant reference voltage, varying, for each test, the voltage level within the same amplitude range. The operation is repeated for all the ranges that will be used in the calibration phase of the device under test. For each range 30 tests are carried out by varying the voltage level between –FS to + FS where FS is the full scale of the range under test. The ranges of the module used are: 300 mV, 1 V, 10 V, 30 V.

The difference between the V_R value applied to the channel and the V_L value measured by the channel is calculated. Both readings are carried out by selecting an integration time which can be between 5 ms and 20 ms. The integration time is suitably set on the multimeter and is selected in the software that manages the acquisition module. The aforementioned difference is defined by the expression:

$$\varepsilon_\mathrm{CH} = \frac{V_\mathrm{L}}{V_\mathrm{R}} - 1 \tag{5.2}$$

After that, an analytic function $\varepsilon_\mathrm{CH,FIT}(V_\mathrm{R})$ is defined in order to fit, with the smallest deviation, the trend of the quantity ε_CH as the amplitude of the applied voltage varies V_R. The structure of the fit function is:

$$\varepsilon_\mathrm{CH,FIT} = \frac{1}{k_\mathrm{CH}} - \frac{V_\mathrm{O}}{V_\mathrm{R}} - 1 \tag{5.3}$$

The coefficients k_CH and V_O represent the unknowns of the problem, the scale factor and the offset associated with the channel under test respectively.

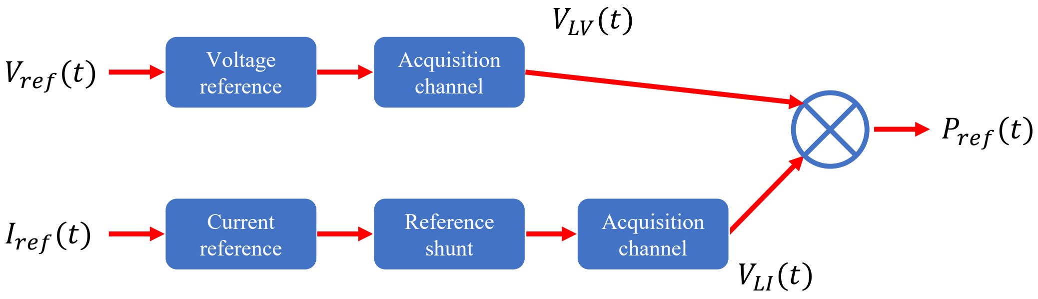

Fig. 5.8 Block diagram of the model for the acquisition channels

5.3.3 Model for the compensation of the systematic errors

From this point on, all the considerations made on the measurement model and the error compensation are valid for purely stationary signals. As previously reported, the standards define the tests only in stationary conditions, there are no dynamic tests for railway applications. Nevertheless, considering the good linearity of reference transducers and the low frequency content of the characteristic railway signals, it is reasonable to use a quasi-static approach for the compensation of the systematic error even in dynamic conditions.

EMF calibration

For the DC calibration of the EMF, consisting of the combination of voltage transducer, current transducer and power and energy meter, the calibration is carried out by comparison between the reading of the power supplied by the meter under test (P_{DUT}), through specific integrated software and the value of the reference quantity, P_{REF} (see Fig. 5.8), as follow:

$$\bar{P}_{\mathrm{REF}} = \bar{P}_{\mathrm{L}}^{*} \cdot \frac{k_{\mathrm{VR}} \cdot k_{\mathrm{IR}}}{R_{\mathrm{SH}}} \tag{5.4}$$

where:

$$\bar{P}_{\mathrm{L}}^{*} = \frac{1}{N} \cdot \sum_{j=1}^{N} (\bar{V}_{\mathrm{LV,j}}^{*} \cdot \bar{V}_{\mathrm{LI,j}}^{*}) \tag{5.5}$$

- $\bar{P}_{\mathrm{REF}}$ is the average value of the active power calculated on a number of samples N;

- N is the number of samples of the voltage and current quantities in the observation time interval T, generally 1 s, taking into account a sampling frequency of the quantities $\bar{V}^*_{\mathrm{LV,j}}$ and $\bar{V}^*_{\mathrm{LI,j}}$ equal to f_{sp}. Therefore, N is defined as: $N = T \cdot f_{\mathrm{sp}}$;
- $\bar{P}^*_{\mathrm{L}}$ is a quantity expressed in squared volt proportional to the primary power;
- $\bar{V}^*_{\mathrm{LV,j}}$ is the reading of the voltage proportional to the primary voltage applied to the EMF;
- k_{VR} is the scale factor of the reference voltage divider;
- $\bar{V}^*_{\mathrm{LI,j}}$ is the reading of the voltage proportional to the primary current applied to the EMF;
- R_{SH} is the reference resistor used to transform the current output of the reference transducer into voltage;
- k_{IR}: is the scale factor of the reference current transducer;

The readings $V_{\mathrm{LV,j}}$ and $V_{\mathrm{LI,j}}$ are obtained as an average value calculated over the period T_{L} which can be selected in the range of values 5 ms $\div$ 20 ms. Considering a sampling frequency usually equal to $f_{\mathrm{sv}} = 50$ kHz, the average reading on the observed values and appropriately corrected is defined according to the formula:

$$\bar{V}^*_{\mathrm{LV,j}} = \left[\frac{1}{N_{\mathrm{L}}}\sum_{k=1}^{N_{\mathrm{L}}} V_{\mathrm{LV,k}}\right] \cdot k_{\mathrm{CH-V}} - V_{\mathrm{oLV}}; \tag{5.6}$$

$$\bar{V}^*_{\mathrm{LI,j}} = \left[\frac{1}{N_{\mathrm{L}}}\sum_{k=1}^{N_{\mathrm{L}}} V_{\mathrm{LI,k}}\right] \cdot k_{\mathrm{CH-I}} - V_{\mathrm{oLI}}; \tag{5.7}$$

where:

- N_{L} is defined as $N_{\mathrm{L}} = T_{\mathrm{L}} \cdot f_{\mathrm{sv}}$
- V_{oLV} is the offset voltage associated with $V_{\mathrm{LV,k}}$
- V_{oLI} is the offset voltage associated with $V_{\mathrm{LI,k}}$
- $k_{\mathrm{CH-V}}$ and $k_{\mathrm{CH-I}}$ are the scale factors of the voltage channels used for the acquisition of the transduced primary voltage and primary current applied to the device under test (obtained from (5.3)).

Combined transducer calibration

For the calibration of the measurand, the ratio error (and the related scale factor) is calculated on the absorbed power. The formula used for each test is the following:

$$\varepsilon_{\mathrm{P}} = \frac{V_{\mathrm{DUT}} \cdot I_{\mathrm{DUT}}}{P_{\mathrm{REF}}} - 1 \tag{5.8}$$

where:

- V_{DUT} is the voltage measured by the device under test;
- I_{DUT} is the current measured by the device under test;
- P_{REF} is the power measured by the reference as shown in 5.3.3.

The quantities V_{DUT} and I_{DUT} are defined as follow:

$$\bar{V}_{\mathrm{DUT}} = \frac{k_{\mathrm{V\_DUT}}}{R_{\mathrm{V\_DUT}}} \cdot \left\{ \left[\frac{1}{N_{\mathrm{L}}} \sum_{k=1}^{N_{\mathrm{L}}} V_{\mathrm{LV\_DUT,k}} \right] \cdot k_{\mathrm{CH-V\_DUT}} - V_{\mathrm{oLV\_DUT}} \right\} \tag{5.9}$$

$$\bar{I}_{\mathrm{DUT}} = \frac{k_{\mathrm{I\_DUT}}}{R_{\mathrm{I\_DUT}}} \cdot \left\{ \left[\frac{1}{N_{\mathrm{L}}} \sum_{k=1}^{N_{\mathrm{L}}} V_{\mathrm{LI\_DUT,k}} \right] \cdot k_{\mathrm{CH-I\_DUT}} - V_{\mathrm{oLI\_DUT}} \right\} \tag{5.10}$$

where:

- $V_{\mathrm{oLV\_DUT}}$ is the voltage offset associate with the acquisition channel that measures the voltage proportional to V;
- $V_{\mathrm{oLI\_DUT}}$ is the voltage offset associate with the acquisition channel that measures the voltage proportional to I_{DUT};
- $k_{\mathrm{CH-V\_DUT}}$ and $k_{\mathrm{CH-I\_DUT}}$ are the scale factors of the acquisition channel that measure the voltage signals proportional to V_{DUT} and I_{DUT};
- $k_{\mathrm{V\_DUT}}$ and $k_{\mathrm{I\_DUT}}$ are the nominal values of the scale factors of the voltage and current transducer under test. Note that these quantities, unlike the others, do not have a statistical nature;

- $R_{\mathrm{V\_DUT}}$ and $R_{\mathrm{I\_DUT}}$ are the resistance values used to convert the current signals provided by the device under test, into voltage signals.

The quantities V_{DUT} and I_{DUT} are obtained starting from the average of the instantaneous values in a time interval whose duration can be selected between 5 ms and 20 ms.

Experimental results on commercial EMF

Here is reported an analysis of the performance of the combined transducer section of EMF under test in the actual operating condition. Its characteristics are reported in Table 5.1. In this analysis only the error contributes related to the VMF and CMF have been considered.

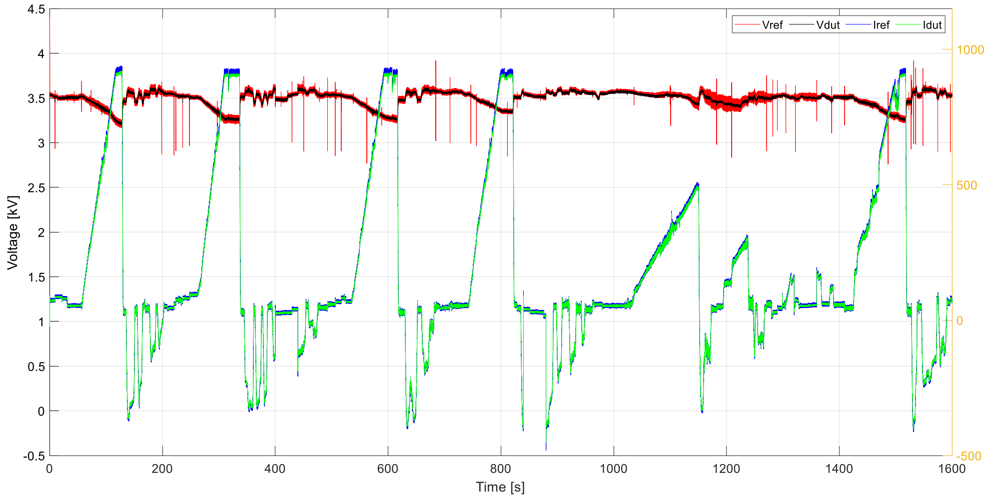

Fig. 5.9 Performance analysis on EMF in actual operating conditions

In Fig. 5.9 is shown a part of the route from Susa to Torino. The signals in red and blue are respectively the voltage and the current acquired by the reference transducers, while in black and green are reported the voltage and current obtained by the device under test. The first thing that can be noted is that the device under test completely neglects the fast voltage oscillation and the ripple. This is mainly due to a lack of resolution and a slow sampling frequency of the device under test acquisition system.

Thanks to this kind of test it is easy to understand that, especially for the current, the working condition for an EMF are very far from the ones currently tested during a calibration. Therefore, in order to obtain a more reliable knowledge of the energy consumption of the whole railway system, an improvement on the calibration procedures that takes into account the real operating condition is mandatory.

The ratio error (calculated as eq. 5.8) has been evaluated with three different time windows, t_{w}: 5 ms, 20 ms and the sampling step 20 μs. Considering the same time windows, the energy measured by the reference transducers and the energy measured with the outputs of the combined transducer have been evaluated as follow:

$$E = P \cdot t_{\mathrm{w}} \tag{5.11}$$

The results, reported in Table 5.4, show that there are no significant difference related to the time window.

Table 5.4 ε_{P} in dynamic conditions with 3 different time windows

Time window	ε_P	E_{REF}	E_{DUT}
20 µs	-1.34	258.763	255.298
5 ms	-1.34	258.764	255.298
20 ms	-1.34	258.764	255.298

5.4 Uncertainty analysis

5.4.1 Uncertainty on the calibration of acquisition modules

Identified the fitting function, 5.3, the maximum residual difference can be defined as:

$$RES = MAX(|\varepsilon - \varepsilon_{\mathrm{fit}}|) \tag{5.12}$$

Assuming a rectangular probability distribution, the standard uncertainty associated with the difference ε is obtained as:

$$u(\varepsilon) = \frac{RES}{\sqrt{3}} \tag{5.13}$$

Considering expression 5.3 and applying the uncertainty propagation, we obtain:

$$u(\varepsilon) = \sqrt{\frac{1}{k_{\mathrm{CH}}^2} \cdot \left(\frac{u(k_{\mathrm{CH}})}{k_{\mathrm{CH}}}\right)^2 + \left(\frac{u(V_{\mathrm{o}})}{V_{\mathrm{R}}}\right)^2} \tag{5.14}$$

The relative components $\frac{u(k_{\mathrm{CH}})}{k_{\mathrm{CH}}}$ and $\frac{u(V_{\mathrm{o}})}{V_{\mathrm{R}}}$ are assumed to be equal in value and equal to u_{r}. With this assumption, it is possible to calculate this value as follows:

$$u_{\mathrm{r}} = \frac{u(\varepsilon)}{\sqrt{\frac{1}{k_{\mathrm{CH}}^2} + 1}} \tag{5.15}$$

5.4.2 Uncertainty on the calibration of the EMF

EMF with digital output

The combined relative uncertainty, associated with the value of power Pref, is obtained starting from the relation (5.4), considering all the input quantities not correlated, and is expressed by the relation:

$$u_{\mathrm{c,r}} = \sqrt{(u_{\mathrm{c,r}}(\bar{P}_{\mathrm{L}}^*))^2 + (u_{\mathrm{r}}(k_{\mathrm{VR}}))^2 + (u_{\mathrm{r}}(R_{\mathrm{SH}}))^2 + (u_{\mathrm{r}}(k_{\mathrm{IR}}))^2} \tag{5.16}$$

The uncertainty related to $u_{\mathrm{c,r}}(\bar{P}_{\mathrm{L}}^*)$ is evaluated with the following:

$$u_{\mathrm{c,r}}(\bar{P}_{\mathrm{L}}^*) = \frac{1}{\bar{P}_{\mathrm{L}} \cdot N} \cdot \sqrt{\sum_{j=1}^{N} \left(u_{\mathrm{c}}(P_{\mathrm{j}})\right)^2} \tag{5.17}$$

where N is defined in 5.3.3. Moreover, $u_{\mathrm{c}}(P_{\mathrm{j}})$ is calculated as:

$$u_{\mathrm{c}}(P_{\mathrm{j}}) = P_{\mathrm{j}}^* \cdot \sqrt{(u_{\mathrm{r}}(\bar{V}_{\mathrm{LV,j}}^*))^2 + (u_{\mathrm{r}}(\bar{V}_{\mathrm{LI,j}}^*))^2} \tag{5.18}$$

Finally, the uncertainties $u_{\mathrm{r}}(\bar{V}^*_{\mathrm{LV,j}}$ and $u_{\mathrm{r}}(\bar{V}^*_{\mathrm{LI,j}}$ are calculated starting from (5.6 and 5.7), being the combination of a number of N_{L} observations whose average value is corrected by the offset introduced by the acquisition channels through the expressions:

$$\begin{cases} u_{\mathrm{r}}(\bar{V}^*_{\mathrm{LV,j}}) = \frac{1}{\bar{V}^*_{\mathrm{LV}}} \cdot \sqrt{\left(k_{\mathrm{CH-V}} \cdot u_{\mathrm{A}}(\bar{V}_{\mathrm{LV,j}})\right)^2 + \left(\bar{V}_{\mathrm{LV,j}} \cdot u(k_{\mathrm{CH-V}})\right)^2 + (u(V_{\mathrm{oLV}}))^2} \\ u_{\mathrm{r}}(\bar{V}^*_{\mathrm{LI,j}}) = \frac{1}{\bar{V}^*_{\mathrm{LI}}} \cdot \sqrt{\left(k_{\mathrm{CH-I}} \cdot u_{\mathrm{A}}(\bar{V}_{\mathrm{LI,j}})\right)^2 + \left(\bar{V}_{\mathrm{LI,j}} \cdot u(k_{\mathrm{CH-I}})\right)^2 + (u(V_{\mathrm{oLI}}))^2} \end{cases} \tag{5.19}$$

The approach described above can be used in a generic situation of variable voltage and current quantities over time. In the case of a calibration with steady state the voltage and current applied, assuming that the uncertainty associated with the power reading is the same for all observations, equation (5.18) becomes:

$$u_{\mathrm{c,r}}(\bar{P}^*_L) = \frac{1}{\bar{P}_L \cdot \sqrt{N}} \cdot u_{\mathrm{c}}(P^*) \tag{5.20}$$

As an example, the Uncertainty budget related to the measurement of power averaged over a time T of 1 s, obtained from observations averaged every 5 ms with a sampling frequency $f_{\mathrm{sv}} = 50$ kHz, is reported in Table 5.5. The quantities voltage and current, apply to the device under test are stationary. A voltage of 3 kV and a current of 500 A are applied.

Table 5.5 Uncertainty budget on EMF related to the measurement of power averaged over a time T of 1 s, obtained from observations averaged every 5 ms with a sampling frequency $f_{\mathrm{sv}} = 50$ kHz. V = 3 kV, I = 500 A

Quantity	**Estimate**	**Type Uncertainty**	**PDF**	**Sensitivity Coefficient**	**Uncertainty Component**
$\bar{V}_{\mathrm{LV}}$	2.499900 V	$75 \cdot 10^{-6}$ V	Normal	1.002 V/V	$75 \cdot 10^{-6}$ V
$k_{\mathrm{CH-V}}$	1.002000 V/V	$16 \cdot 10^{-6}$ V	Normal	2.5 V	$40 \cdot 10^{-6}$ V
V_{oLV}	$105 \cdot 10^{-6}$ V	$5 \cdot 10^{-6}$ V	Normal	1	$5 \cdot 10^{-6}$ V
$\bar{V}^*{}_{\mathrm{LV}}$	2.500000 V		$u(\bar{V}^*{}_{LV})$		$85 \cdot 10^{-6}$ V
$\bar{V}_{\mathrm{LI}}$	0.270166 V	$8 \cdot 10^{-6}$ V	Normal	1.000 V/V	$8 \cdot 10^{-6}$ V
$k_{\mathrm{CH-I}}$	1.001700 V/V	$16 \cdot 10^{-6}$ V	Normal	0.27 V	$4.3 \cdot 10^{-6}$ V
V_{oLI}	$105 \cdot 10^{-6}$ V	$5 \cdot 10^{-6}$ V	Normal	1	$5 \cdot 10^{-6}$ V
$\bar{V}^*{}_{\mathrm{LI}}$	0.267200 V		$u(\bar{V}^*{}_{LI})$		$13 \cdot 10^{-6}$ V
$\bar{V}_{\mathrm{LV}}$	2.500000 V/V	$32 \cdot 10^{-6}$ V	Normal	1	$32 \cdot 10^{-6}$ V
V_{oLI}	$105 \cdot 10^{-6}$ V	$50 \cdot 10^{-6}$ V/V	Normal	1	$50 \cdot 10^{-6}$ V
$\overline{P^*}_{\mathrm{L}}(V^2)$	0.674700 V^2		$\frac{1}{\sqrt{N}} \cdot \sqrt{\left(u_r\left(\bar{V}^*{}_{\mathrm{LV,j}}\right)\right)^2 + \left(u_r\left(\bar{V}^*{}_{\mathrm{LI,j}}\right)\right)^2}$		$13 \cdot 10^{-6}$ V

Table 5.6 and Table 5.7 show the best DC power measurement capabilities for two types of systems: the railway system, with variable voltage between 2.5 kV and 4 kV and for the metropolitan system, with variable voltage between 1.2 kV and 1.8 kV

Quantity	Estimate	Type Uncertainty	PDF	Sensitivity Coefficient	Uncertainty Component
$\overline{P^*}_{\mathrm{L}}(V^2)$	0.675680 V^2	$13 \cdot 10^{-6}$ V	Normal	1 $(\mathrm{A/A})^2$	$13 \cdot 10^{-6}$ (W/W)
k_{VR}	1200.00 V/V	$50 \cdot 10^{-6}$ V/V	Normal	1 (W/W)	$50 \cdot 10^{-6}$ (W/W)
R_{SH}	1.000000 Ω	$5 \cdot 10^{-6}$ Ω/Ω	Normal	1 $(\mathrm{A/A})^2$	$5 \cdot 10^{-6}$ (W/W)
k_{IR}	1875.00 A/A	$10 \cdot 10^{-6}$ V/V	Normal	1 (W/W)	$10 \cdot 10^{-6}$ (W/W)
P_{REF}	1.5 MW		$u_{c,r}(P_{REF})$		$54 \cdot 10^{-6}$ (W/W)

Table 5.6 Best DC power measurement capabilities for EMF for railway applications

Current range	Expanded Uncertainty (k=2) on power measurement $\mathrm{U}(\mathrm{P}_{\mathrm{ref}})$
± 5 A $\div \pm 50$ A	150 $\mu W/W$
± 51 A $\div \pm 125$ A	90 $\mu W/W$
± 126 A $\div \pm 200$ A	110 $\mu W/W$
± 201 A $\div \pm 375$ A	90 $\mu W/W$
± 376 A $\div \pm 1000$ A	110 $\mu W/W$
± 1001 A $\div \pm 2000$ A	90 $\mu W/W$

Table 5.7 Best DC power measurement capabilities for EMF for metro applications

Current range	**Expanded Uncertainty (k=2) on power measurement U($\mathbf{P_{ref}}$)**
±5 A ÷ ±50 A	200 $\mu W/W$
±51 A ÷ ±125 A	110 $\mu W/W$
±126 A ÷ ±200 A	130 $\mu W/W$
±201 A ÷ ±375 A	110 $\mu W/W$
±376 A ÷ ±1000 A	130 $\mu W/W$
±1001 A ÷ ±2000 A	110 $\mu W/W$

Combined transducer

Considering the measurement model expressed by relation (5.8), the following expression for the calculation of combined uncertainty associated with ε_{P} is obtained:

$$u(\varepsilon_{\mathrm{P}}) = \frac{V_{\mathrm{DUT}} \cdot V_{\mathrm{DUT}}}{P_{\mathrm{REF}}} \cdot \sqrt{(u_{\mathrm{r}}(P_{\mathrm{REF}}))^2 + (u_{\mathrm{r}}(\bar{V}_{\mathrm{DUT}}))^2 + (u_{\mathrm{r}}(\bar{I}_{\mathrm{DUT}}))^2} \tag{5.21}$$

where $u_{\mathrm{r}}(P_{\mathrm{REF}})$, $u_{\mathrm{r}}(\bar{V}_{\mathrm{DUT}})$, $u_{\mathrm{r}}(\bar{I}_{\mathrm{DUT}})$ represent the corresponding uncertainties expressed as relative with respect to their mean value. The calculation of the uncertainty associated with $\bar{V}_{\mathrm{DUT}}$ and $\bar{I}_{\mathrm{DUT}}$ is obtained as follows:

$$\begin{cases} [u_{\mathrm{r}}(\bar{V}^*_{\mathrm{DUT}})]^2 = \left(\dfrac{1}{\bar{V}_{\mathrm{DUT}*}}\right)^2 \cdot \\ \qquad (c_{\mathrm{V1}} \cdot u_{\mathrm{A}}(\bar{V}_{\mathrm{LV\_DUT}}))^2 + (c_{\mathrm{V2}} \cdot u(k_{\mathrm{CH-V\_DUT}}))^2 + \\ \qquad (c_{\mathrm{V3}} \cdot u(V_{\mathrm{oLV\_DUT}}))^2 + (c_{\mathrm{V4}} \cdot u(R_{\mathrm{V\_DUT}}))^2 \\ \\ [u_{\mathrm{r}}(\bar{I}^*_{\mathrm{DUT}})]^2 = \left(\dfrac{1}{\bar{I}_{\mathrm{DUT}*}}\right)^2 \cdot \\ \qquad (c_{\mathrm{I1}} \cdot u_{\mathrm{A}}(\bar{V}_{\mathrm{LI\_DUT}}))^2 + (c_{\mathrm{I2}} \cdot u(k_{\mathrm{CH-I\_DUT}}))^2 + \\ \qquad (c_{\mathrm{I3}} \cdot u(V_{\mathrm{oLI\_DUT}}))^2 + (c_{\mathrm{I4}} \cdot u(R_{\mathrm{I\_DUT}}))^2 \end{cases} \tag{5.22}$$

In the following Table 5.8 are listed the values of sensitivity coefficients

Table 5.8 Best DC power measurement capabilities for metro system

c_{V} **term**	**Expression**
c_{V1}	$k_{\mathrm{V\_DUT}} \cdot k_{\mathrm{CH-V\_DUT}} \cdot \frac{1}{R_{\mathrm{V\_DUT}}}$
c_{V2}	$k_{\mathrm{V\_DUT}} \cdot V_{\mathrm{LV\_DUT}} \cdot \frac{1}{R_{\mathrm{V\_DUT}}}$
c_{V3}	$-k_{\mathrm{V\_DUT}} \cdot \frac{1}{R_{\mathrm{V\_DUT}}}$
c_{V4}	$\frac{k^2_{\mathrm{V_{DUT}}}}{R_{\mathrm{V\_DUT}}} \cdot \left(V_{\mathrm{oLV\_DUT}} - \bar{V}_{\mathrm{LV\_DUT}} \cdot k_{\mathrm{CH\_V\_DUT}}\right)$
c_{I1}	$k_{\mathrm{I\_DUT}} \cdot k_{\mathrm{CH-I\_DUT}} \cdot \frac{1}{R_{\mathrm{I\_DUT}}}$
c_{I2}	$k_{\mathrm{I\_DUT}} \cdot V_{\mathrm{LI\_DUT}} \cdot \frac{1}{R_{\mathrm{I\_DUT}}}$
c_{I3}	$-k_{\mathrm{I\_DUT}} \cdot \frac{1}{R_{\mathrm{I\_DUT}}}$
c_{I4}	$\frac{k^2_{\mathrm{I_{DUT}}}}{R_{\mathrm{I\_DUT}}} \cdot \left(V_{\mathrm{oLI\_DUT}} - \bar{V}_{\mathrm{LI\_DUT}} \cdot k_{\mathrm{CH\_I\_DUT}}\right)$

Type A uncertainty, associated with N_{L} independent observations is estimated as:

$$\begin{cases} u_{\mathrm{A}}(\bar{V}_{\mathrm{LV\_DUT}}) = \sqrt{\frac{1}{N_{\mathrm{L}}-1\cdot N_{\mathrm{L}}} \sum_{k=1}^{N_{\mathrm{L}}} \left(\bar{V}_{\mathrm{LV\_DUT}} - V_{\mathrm{LV\_DUT,k}}\right)^2} \\ u_{\mathrm{A}}(\bar{V}_{\mathrm{LI\_DUT}}) = \sqrt{\frac{1}{N_{\mathrm{L}}-1\cdot N_{\mathrm{L}}} \sum_{k=1}^{N_{\mathrm{L}}} \left(\bar{V}_{\mathrm{LI\_DUT}} - V_{\mathrm{LI\_DUT,k}}\right)^2} \end{cases} \tag{5.23}$$

Table 5.9 Uncertainty budget on combined transducer related to the measurement of power averaged over a time T of 1 s, obtained from observations averaged every 5 ms with a sampling frequency $f_{\mathrm{sv}} = 50$ kHz. V = 3 kV, I = 500 A

Quantity	**Estimate**	**Type Uncertainty**	**PDF**	**Sensitivity Coefficient**	**Uncertainty Component**
$\bar{V}_{\mathrm{LV\_DUT}}$	0.202100 V	$7 \cdot 10^{-6}$ V	Normal	15000 V/V	$105 \cdot 10^{-3}$ V
$k_{\mathrm{CH-V\_DUT}}$	1.002000 V/V	$10 \cdot 10^{-6}$ V	Normal	3001.5 V	$30 \cdot 10^{-3}$ V
$V_{\mathrm{oLV\_DUT}}$	$105 \cdot 10^{-6}$ V	$10 \cdot 10^{-6}$ V	Normal	-1500	0.15 V
$R_{\mathrm{V\_DUT}}$	10 Ω	$50 \cdot 10^{-6}$ V	Normal	-300 A	$15 \cdot 10^{-3}$ V
$\bar{V}^{*}{}_{\mathrm{DUT}}$	3028.65 V		$u(\bar{V}^{*}{}_{\mathrm{DUT}})$		0.1860 V
$\bar{V}_{\mathrm{LI\_DUT}}$	0.270166 V	$8 \cdot 10^{-6}$ V	Normal	1.000 V/V	$8 \cdot 10^{-6}$ V
$k_{\mathrm{CH-I\_DUT}}$	1.001700 V/V	$16 \cdot 10^{-6}$ V	Normal	0.27 V	$4.3 \cdot 10^{-6}$ V
$V_{\mathrm{oLI\_DUT}}$	$105 \cdot 10^{-6}$ V	$5 \cdot 10^{-6}$ V	Normal	1	$5 \cdot 10^{-6}$ V
$R_{\mathrm{I\_DUT}}$	10 Ω	$50 \cdot 10^{-6}$ V	Normal	-50 A	$-2.5 \cdot 10^{-3}$ V
$\bar{I}^{*}{}_{\mathrm{DUT}}$	499.7100 V		$u(I_{\mathrm{DUT}})$		0.0767 A

Quantity	**Estimate**	**Type Uncertainty**	**PDF**	**Sensitivity Coefficient**	**Uncertainty Component**
$\bar{I}^*_{\mathrm{DUT}}$	499.7100 A	$153 \cdot 10^{-6}$ A	Normal	1	$153 \cdot 10^{-6}$ (W/W)
$\bar{V}^*_{\mathrm{DUT}}$	3028.65 V	$59 \cdot 10^{-6}$ V/V	Normal	1	$59 \cdot 10^{-6}$ (W/W)
P^*_{DUT}	1.506004 MW	$53 \cdot 10^{-6}$ W/W	Normal	1	$53 \cdot 10^{-6}$ (W/W)
P_{REF}	1.5 MW		$u(\varepsilon_P)$		$173 \cdot 10^{-6}$ (W/W)

Table 5.10 and Table 5.11 show the best DC power measurement capabilities for two types of systems: the railway system, with variable voltage between 2.5 kV and 4 kV and for the metropolitan system, with variable voltage between 1.2 kV and 1.8 kV

Table 5.10 Best DC power measurement capabilities for combined transducer for railway applications

Current range	**Expanded Uncertainty (k=2) on power measurement $\mathbf{U(P_{ref})}$**
±5 A $\div \pm$50 A	400 $\mu W/W$
±51 A $\div \pm$125 A	300 $\mu W/W$
±126 A $\div \pm$200 A	350 $\mu W/W$
±201 A $\div \pm$375 A	300 $\mu W/W$
±376 A $\div \pm$1000 A	350 $\mu W/W$
±1001 A $\div \pm$2000 A	300 $\mu W/W$

Table 5.11 Best DC power measurement capabilities for combined transducer for metro applications

Current range	**Expanded Uncertainty (k=2) on power measurement U($\mathbf{P_{ref}}$)**
±5 A ÷ ±50 A	450 $\mu W/W$
±51 A ÷ ±125 A	350 $\mu W/W$
±126 A ÷ ±200 A	400 $\mu W/W$
±201 A ÷ ±375 A	350 $\mu W/W$
±376 A ÷ ±1000 A	400 $\mu W/W$
±1001 A ÷ ±2000 A	350 $\mu W/W$

In the case of dynamic tests, from 5 A to 1200, the metrological capabilities are summarized below:

Table 5.12 Best DC power measurement capabilities for combined transducer for railway applications in dynamic conditions

Current range	**Expanded Uncertainty (k=2) on power measurement U($\mathbf{P_{ref}}$)**
±5 A ÷ ±50 A	1200 $\mu W/W$
±51 A ÷ ±125 A	900 $\mu W/W$
±126 A ÷ ±200 A	650 $\mu W/W$
±201 A ÷ ±375 A	500 $\mu W/W$
±376 A ÷ ±1200 A	460 $\mu W/W$

5.5 Testing the on-board detection systems

The development of power quality event detection technology and program in DC system is a new topic. The latest technology related to power quality in DC railway systems is provided by the standard EN 50163 [17] which defines the main characteristics of the supply voltage for traction systems and EN 50388 [18] which establishes the requirements. Compatibility of rolling stock with infrastructure. Both of these standards provide information related to catenary voltage, but do not take into account all possible events that can occur in the power supply system, nor do they provide an exhaustive description of the procedures that must be applied to power quality monitoring. PQ is a critical point in terms of electromagnetic compatibility when the electrical information flow in the binary track for signal transmission. In this case, limits in the frequency domain for the current absorbed and injected by trains are defined. Currently, there is no European or international standard providing such limits and procedures for estimating them. Only programs provided by the National Infrastructure Manager are available [71]. The definition of pq events and their classification in railway system is the subject of study of many researchers and technical committees. In addition to standard definitions of PQ in DC railway systems, measurement systems for continuous and accurate monitoring of power quality events are also evolving. Under real conditions, the electrical signal is very distorted and different events are happening at the same time. In addition, the nonlinearity of the transducers can bring in spurious harmonics or corrupt harmonic estimates. The Phantom Power calibrator can be used for reproducing the real electrical conditions experienced at the pantograph of a general locomotive and this can help to evaluate the reliability of the developed measurement system without having to equip the locomotive with a new measurement system for testing. The facility can be used to assess the reliability of power quality and impedance monitoring systems involving voltage and current sensors, acquisition systems, and detection algorithms for the presence of multiple power quality events. Considering the low linearity error of the transducer, it can be assumed that the relative uncertainty is estimated to be less than 1% even for the occurrence of fast PQ phenomena.

5.5.1 Examples of transient events

To characterize on-board detection systems, it must be taken into account that the voltage supplied to the train is often distorted, characterized by dips and swell, and affected by ripples; these distortions are much larger than those experienced by traditional power networks. At the same time, the current drawn by the train also contains high levels of ripple, as well as step changes [72] associated with the braking and acceleration of the trains. The arcing phenomenon caused by poor pantograph-to-line contact quality can also introduce transient distortion.

The voltage dip showed in Fig. 5.10, measured in on-field campaign, can be used for the characterization of the dip detection system.

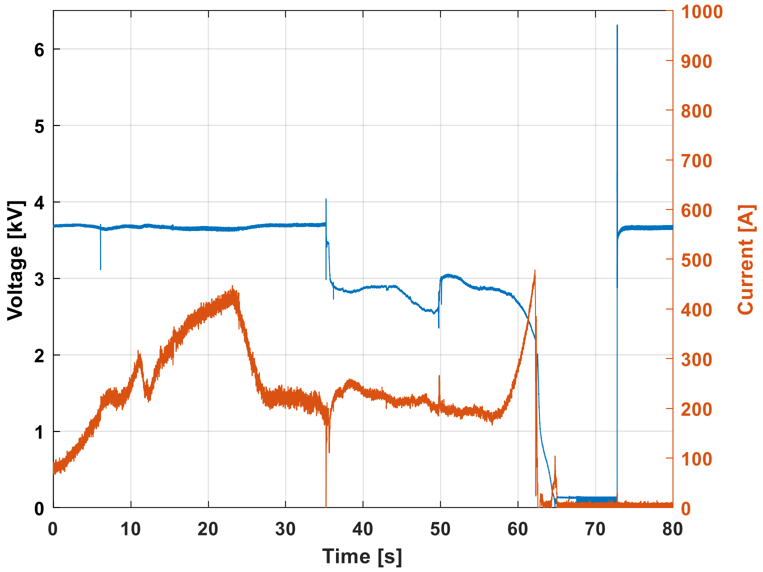

Fig. 5.10 Example of voltage dip generated by the calibration system

During the traction phase, a voltage drop occurs due to a failure of the power supply system. It seems that, the power supply system cannot withstand the increase in absorbed power, so the system shuts down in the subsequent traction.

Another PQ phenomenon very common in the railway system is the electric arc, very frequent at high speeds and with low temperatures characterizing the winter periods. Due to high arc temperatures, overhead contact lines suffer damage and performance degradation over time. Furthermore, due to the presence of the input filter of the locomotive, the sudden voltage changes trigger transients and strong harmonic distortion of the current, as shown in the Fig. 5.11 [73].

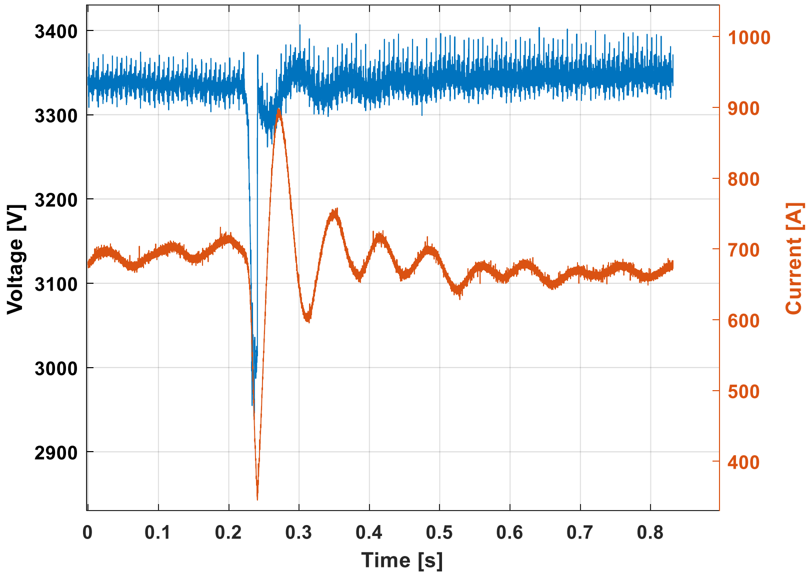

Fig. 5.11 Example of electric arc generated by the calibration system

Emission problems provided by current transients are so severe that they interfere with signaling systems to the point that infrastructure managers establish limits for harmonic content. Therefore, a tool like the presented calibration system, that emulates actual waveform with such particular characteristic could be very helpful in these circumstances [56].

A PQ phenomenon that characterizes the railway environment is the voltage ripple that is due to the AC/DC conversion stage in the substation. Fig. 5.12 shows behaviour of the actual ripple experienced during the Bardonecchia - Torino journey.

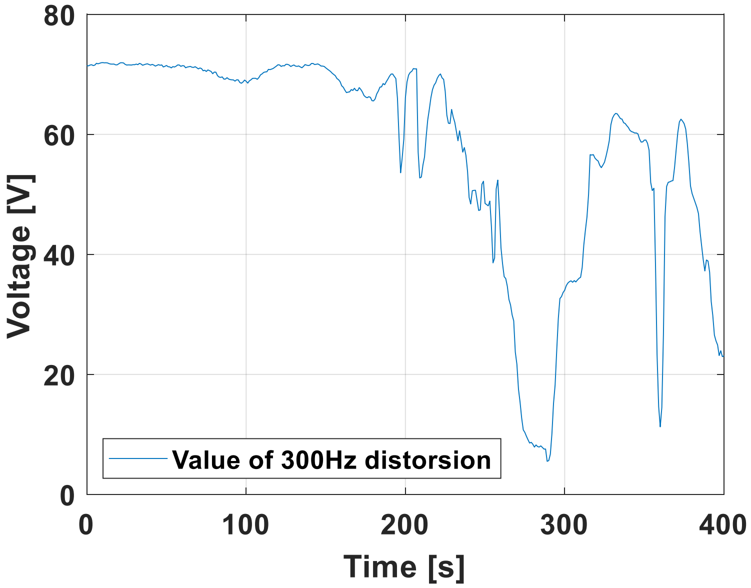

Fig. 5.12 Voltage ripple experienced on the route Bardonecchia - Torino

With a generation system capable of reproducing actual waveforms, it is possible to reproduce this phenomenon in the laboratory and analyse its impact on the performance of on-board instrumentation. As reported in Table 5.2, the system can generate voltages up to 10 kV, in a bandwidth of 10 kHz, so overvoltage phenomena can be widely replicated.

In order to reduce losses, in railway system the voltage level is often higher than the rated voltage of 3kV. Under certain circumstances, such as at night when traffic is significantly reduced, the line voltage may approach regulatory limits.

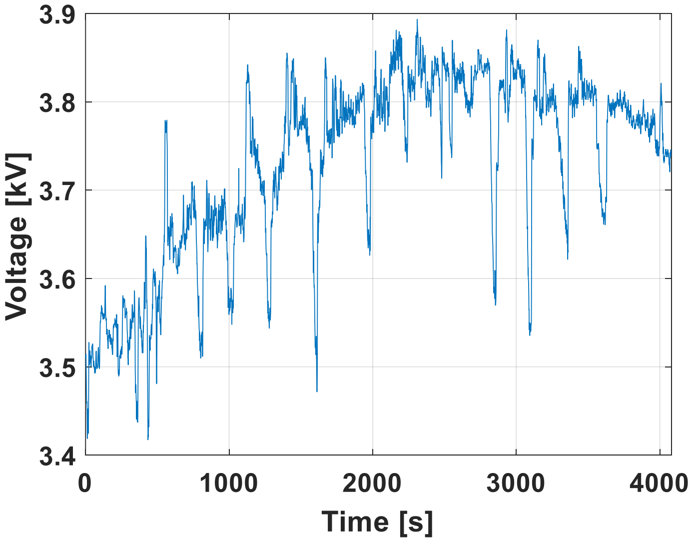

Fig. 5.13 Example of high voltage generated by the calibration system

Fig. 5.13 shows the voltage behaviour of the line during the Bussoleno - Torino journey after 10 pm. The voltage value is always higher than 3.5 kV and has an average of 3728V, almost 25% higher than the nominal voltage. Taking advantage of the possibility of generating signals like the one shown in Fig. 5.13, the performance of the whole voltage control system on board the train can be verified even in dynamic conditions. Furthermore, by applying these signals directly on board the train, it is possible to study the impact of these overvoltages on other components of the train such as the rheostatic braking system, fundamental in the management of energy consumption.

Chapter 6

Conclusions

This thesis reports the impact of metrology on the railway environment; the main topics covered include the analysis of energy flows on board two trains operating in a 3 kV DC railway system and a 1.5 kV DC metropolitan system, methodologies for the correction of errors in the measurement of dissipated energy on braking resistors, the analysis of PQ phenomena characteristic of the railway system and, finally, a system for the characterization of the energy meters on board the train.

The work presents the technical solutions and the setup arrangement for the measurement of the power/energy absorbed and generated by the analyzed DC locomotives, operating in commercial service, the amount of electrical power/energy recovered and wasted during a braking stage and the quality of the power at the pantograph. Moreover, this thesis discuss the results of a measurement campaign that has been conducted on-board of a train operating on the metro line that serves the city of Madrid, where a reversible substation is installed. A new index (L_u) that quantifies the line unavailability to receive energy is proposed. The impact of RSS was analysed by performing statistical analysis of a large number of braking events over a long-time interval taking into account separately different supply conditions (RSS on and off) and high and low circulating train number. The behaviour of L_u versus the actual and rated supply voltage, obtained by fitting the samples provided by each braking, clarifies that the impact of the RSS increases as such voltage ratio increases. Although the RSS is in experimental stage and the amount of energy sent back to the main grid is limited by the law in force, the results of this comparison show that the RSS adoption has potential to considerably improve the overall efficiency, in particular when the number of trains is low.

Two methodologies for the accurate estimation of the power and energy dissipated by a braking rheostat installed on-board rolling stock have been presented. A description of the measurement procedure applied on-board the vehicles and a model used for the power estimation are provided. The treatment focuses on the description, modeling and quantification of two systematic errors that affect the power estimation. One is due to the approximate model for the power estimation, a consequence of practical implementation of the measurement setup that has to guarantee an adequate level of safety, reliability and has to reduce, as much as possible the invasiveness towards the electrical apparatuses of the locomotive. The second error is introduced by the limited bandwidth of the current sensor employed in the chopped-current measurement and the limited sample frequency for the digitization of the signal.

The first methodology consists in obtaining the correct power dissipated by the braking rheostat by multiplying the measured power (obtained as the product of the DC voltage of the rheostat by the current of the rheostat) by two factors, functions of the duty-cycle, for the correction of the aforementioned systematic errors. It has been demonstrated that the correction factors dramatically affect the power estimation for low power amplitude, that is, low duty-cycle. For a duty-cycle of about 1%, which is the minimum duty-cycle experienced, the corrected power is reduced by about 36%. The same occurs for the range of variability introduced by the stochastic positions of the sampled data with respect to the current pulse. The variability at 1% duty-cycle ranges from 17% to 41% with an average value of 31%. This means that, as expected, the uncertainty associated with the power estimation is higher for low power amplitude. It can be assumed that long braking with low duty-cycle, that is, low dissipated power, is estimated with a high uncertainty. The proposed technique has been applied to a real dissipative braking event recorded on-board a metro vehicle.

The second methodology consists in a new approach to simplify the measurement of power dissipated on board rheostat task and it is applied to real test cases coming from measurement campaign on-board train. It is easy to implement because it relies only on information already available to the train control unit. Despite its simplicity, it allows taking into account the current transient due to the presence of the rheostat inductance. It allows obtaining fairly accurate results (1%). Still maintaining the cost low, it allows for reaching accuracies comparable with the first methodology used as reference method.

Some aspects of the assessment of the power quality, through standardized monitoring techniques, in the railway traction power supply systems are discussed in this thesis work. The measurement procedures of some of the main power quality index, well defined and widely used for conventional power systems (interruption, voltage dip/swell and harmonics) are analyzed and extended with minimal changes to become compatible with all railway systems. Proposed techniques are applied to a large measurement campaign. The obtained results were discussed, showing how the PQ indexes can be useful for predictive maintenance or to identify specific problems of the supply system and the train.

Particular attention is paid to the phenomenon of the electric arc in order to provide new data to understand the dynamics of the arc discharge, how it evolves and how it quenches when the current reaches zero ampere. In particular, the dissipated power terms associated to the arc itself and to the electric phenomena (oscillation of the onboard filter) and events (activation of the dissipative braking chopper) have been evaluated, showing that the peak power levels are notable.

Finally, a setup for the calibration of energy measurement chains for DC railway application has been described. The uncertainty estimation is provided for different configurations (integration-time, current amplitude). In steady state tests, a worst case uncertainty of 250 μW/W has been obtained while the uncertainty contributions in dynamic tests is in worst case of 1200 μW/W.

The same setup can be used as a facility to characterize the on board detection system. This because it allows to emulate signal as voltage dip and swell, electric arcs, bad-contact between pantograph and catenary and other PQ phenomena.

References

[1] European Commission. White paper roadmap to a single european transport area – towards a competitive and resource efficient transport system /* com/2011/0144 final */, Mar. 2011.

[2] European Commission. In-depth analysis in support of the commission communication com(2018) 773 - a clean planet for all. a european long-term strategic vision for a prosperous, modern, competitive and climate neutral economy.

[3] F. Cascetta, G. Cipolletta, A. Delle Femine, J. Quintana Fernández, D. Gallo, D. Giordano, and D. Signorino. Impact of a reversible substation on energy recovery experienced on-board a train. *Measurement*, page 109793, 2021.

[4] Vasilis A. Kleftakis and Nikos D. Hatziargyriou. Optimal control of reversible substations and wayside storage devices for voltage stabilization and energy savings in metro railway networks. *IEEE Transactions on Transportation Electrification*, 5(2):515–523, 2019.

[5] Giuliano Cipolletta, Antonio Delle Femine, Daniele Gallo, Mario Luiso, and Carmine Landi. Design of a stationary energy recovery system in rail transport. *Energies*, 14(9), 2021.

[6] G. Cipolletta, A. Delle Femine, D. Gallo, C. Landi, M. Luiso, A. Gallo, L. Pastena, F. Balic, J. Quintana Fernández, D. Giordano, and D. Signorino. Monitoring a dc train supplied by a reversible substation. In *2020 IEEE International Instrumentation and Measurement Technology Conference (I2MTC)*, pages 1–6, 2020.

[7] Mihaela Popescu and Alexandru Bitoleanu. A review of the energy efficiency improvement in dc railway systems. *Energies*, 12(6), 2019.

[8] EN 50163:2004-11- Railway applications - Supply voltages of traction systems . Standard, CEI-CT9, CEI-SC9C, 2006.

[9] EURAMET. Metrology for smart energy management in electric railway systems. https://myrails.it/, 16ENG04 MyRailS, 2017.

[10] Yu M In'kov, VP Feoktistov, OV Tretinnikov, et al. Control of recuperative braking of a locomotive under limitation of the energy recovery to a contact system. *Russian Electrical Engineering*, 86(9):509–513, 2015.

[11] Arturo González-Gil, Roberto Palacin, and Paul Batty. Sustainable urban rail systems: Strategies and technologies for optimal management of regenerative braking energy. *Energy conversion and management*, 75:374–388, 2013.

[12] C Spalvieri, I Rossetta, R LaMedica, A Ruvio, and A Papalini. Train braking impact on energy recovery: The case of the 3 kv dc railway line roma-napoli via formia. In *2019 AEIT International Annual Conference (AEIT)*, pages 1–6. IEEE, 2019.

[13] İbrahim Şengör, Hasan Can Kılıçkıran, Hüseyin Akdemir, Bedri Kekezoğlu, Ozan Erdinc, and Joao PS Catalao. Energy management of a smart railway station considering regenerative braking and stochastic behaviour of ess and pv generation. *IEEE Transactions on Sustainable Energy*, 9(3):1041–1050, 2017.

[14] Vitaly Gelman. Braking energy recuperation. *Vehicular Technology Magazine, IEEE*, 4:82 – 89, 10 2009.

[15] Daniel Cornic. Efficient recovery of braking energy through a reversible dc substation. In *Electrical Systems for Aircraft, Railway and Ship Propulsion*, pages 1–9, 2010.

[16] S Menicanti, M Di Benedetto, A Lidozzi, L Solero, and F Crescimbini. Recovery of train braking energy in 3 kv dc railway systems: a case of study. In *2020 International Symposium on Power Electronics, Electrical Drives, Automation and Motion (SPEEDAM)*, pages 589–594. IEEE, 2020.

[17] EN 50163:2006 Railway applications - Supply voltages of traction systems . Standard, 2006.

[18] EN 50388:2012-08 Railway applications - Power supply and rolling stock - Technical criteria for the coordination between power supply (substation) and rolling stock to achieve interoperability. Standard, 2012-08.

[19] COMMISSION REGULATION (EU). No 1302/2014 of 18 november 2014 concerning a technical specification for interoperability relating to the ‘rolling stock — locomotives and passenger rolling stock’ subsystem of the rail system in the european union.

[20] EN 50463-2:2018 Railway applications - Energy measurement on board trains - Part 2: Energy measuring . Standard, CEI-CT9, April 2018.

[21] COMMISSION REGULATION (EU). No 1301/2014 of 18 november 2014 on the technical specifications for interoperability relating to the ‘energy’ subsystem of the rail system in the union.

[22] International Organization for Standardization. *Guide to the expression of uncertainty in measurement, Supported by BIPM, IEC, IFCC, ISO IUPAC, IUPAP and OIML.* Geneva, 2008.

[23] G. Crotti, A. Delle Femine, D. Gallo, D. Giordano, C. Landi, and M. Luiso. Calibration of voltage and current transducers for dc railway systems. *IEEE Transactions on Instrumentation and Measurement*, 68(10):3850–3860, 2019.

[24] International Organization for Standardization. *Guide to the expression of uncertainty in measurement (GUM)-Supplement 1: Numerical methods for the propagation of distributions*. Geneva, 2004.

[25] Mahdiyeh Khodaparastan, Ahmed A. Mohamed, and Werner Brandauer. Recuperation of regenerative braking energy in electric rail transit systems. *IEEE Transactions on Intelligent Transportation Systems*, 20(8):2831–2847, 2019.

[26] Seyed Saeed Fazel. Energy-efficient emplacement of reversible dc traction power substations in urban railtransport through regenerative energy recovery. *International Journal of Railway*, 1:11–22, 2014.

[27] Morris Brenna, Federica Foiadelli, and Dario Zaninelli. *Electrical railway transportation systems*. John Wiley & Sons, 2018.

[28] Heather Douglas, Clive Roberts, Stuart Hillmansen, and Felix Schmid. An assessment of available measures to reduce traction energy use in railway networks. *Energy Conversion and Management*, 106:1149–1165, 2015.

[29] Shuai Su, Xuekai Wang, Yuan Cao, and Jiateng Yin. An energy-efficient train operation approach by integrating the metro timetabling and eco-driving. *IEEE Transactions on Intelligent Transportation Systems*, 21(10):4252–4268, 2020.

[30] María Dominguez, Antonio Fernández-Cardador, Asunción P. Cucala, and Ramón R. Pecharroman. Energy savings in metropolitan railway substations through regenerative energy recovery and optimal design of ato speed profiles. *IEEE Transactions on Automation Science and Engineering*, 9(3):496–504, 2012.

[31] Zhuopu Hou, Hairong Dong, Shigen Gao, Gemma Nicholson, Lei Chen, and Clive Roberts. Energy-saving metro train timetable rescheduling model considering ato profiles and dynamic passenger flow. *IEEE Transactions on Intelligent Transportation Systems*, 20(7):2774–2785, 2019.

[32] Maite Pena-Alcaraz, Antonio Fernández, Asunción Cucala, Andres Ramos, and Ramón Pecharromán. Optimal underground timetable design based on power flow for maximizing the use of regenerative-braking energy. *Proceedings of the Institution of Mechanical Engineers, Part F: Journal of Rail and Rapid Transit*, 226:397–408, 07 2012.

[33] Xin Yang, Xiang Li, Ziyou Gao, Hongwei Wang, and Tao Tang. A cooperative scheduling model for timetable optimization in subway systems. *IEEE Transactions on Intelligent Transportation Systems*, 14(1):438–447, 2013.

[34] Andrés Ramos, María Teresa Pena, Antonio Fernández, and Paloma Cucala. Mathematical programming approach to underground timetabling problem for maximizing time synchronization. *Dirección y Organización*, (35):88–95, 2008.

[35] A. Nasri, M. Fekri Moghadam, and H. Mokhtari. Timetable optimization for maximum usage of regenerative energy of braking in electrical railway systems. In *SPEEDAM 2010*, pages 1218–1221, 2010.

[36] Daniel Cornic. Efficient recovery of braking energy through a reversible dc substation. In *Electrical Systems for Aircraft, Railway and Ship Propulsion*, pages 1–9, 2010.

[37] G. Crotti, D. Giordano, D. Signorino, A. Delle Femine, D. Gallo, C. Landi, M. Luiso, A. Biancucci, and L. Donadio. Monitoring energy and power quality on board train. In *2019 IEEE 10th International Workshop on Applied Measurements for Power Systems (AMPS)*, pages 1–6, 2019.

[38] Mahdiyeh Khodaparastan, Ahmed A. Mohamed, and Werner Brandauer. Recuperation of regenerative braking energy in electric rail transit systems. *IEEE Transactions on Intelligent Transportation Systems*, 20(8):2831–2847, 2019.

[39] Harkaitz Ibaiondo and Asier Romo. Kinetic energy recovery on railway systems with feedback to the grid. In *Proceedings of 14th International Power Electronics and Motion Control Conference EPE-PEMC 2010*, pages T9–94–T9–97, 2010.

[40] Gabriella Crotti, Antonio Delle Femine, Daniele Gallo, Domenico Giordano, Carmine Landi, Mario Luiso, Andrea Mariscotti, and Paolo Emilio Roccato. Pantograph-to-ohl arc: Conducted effects in dc railway supply system. *IEEE Transactions on Instrumentation and Measurement*, 68(10):3861–3870, 2019.

[41] Vasilis A. Kleftakis and Nikos D. Hatziargyriou. Optimal control of reversible substations and wayside storage devices for voltage stabilization and energy savings in metro railway networks. *IEEE Transactions on Transportation Electrification*, 5(2):515–523, 2019.

[42] European Commission. Transport 2050: The major challenges, the key measures, Mar. 2011.

[43] Jane Lehr and Pralhad Ron. *Pulsed Voltage and Current Measurements*, pages 493–546. 2018.

[44] Helko van den Brom, Domenico Giordano, Danielle Gallo, Andreas Wank, and Yljon Seferi. Accurate measurement of energy dissipated in braking rheostats in dc railway systems. In *2020 Conference on Precision Electromagnetic Measurements (CPEM)*, pages 1–2, 2020.

[45] G. Crotti, D. Giordano, D. Signorino, A. Delle Femine, D. Gallo, C. Landi, M. Luiso, A. Biancucci, and L. Donadio. Monitoring energy and power quality on board train. In *2019 IEEE 10th International Workshop on Applied Measurements for Power Systems (AMPS)*, pages 1–6, 2019.

[46] K. Fujiwara, F. Tamura, A. Tokuchi, K. Takahashi, T. Sasaki, and T. Kikuchi. Design and analysis on coil parameter of linear rogowski coil for measurement of high frequency pulsed current. In *2019 IEEE Pulsed Power Plasma Science (PPPS)*, pages 1–3, 2019.

[47] Domenico Giordano, Davide Signorino, Daniele Gallo, Helko E. van den Brom, and Martin Sira. Methodology for the accurate measurement of the power dissipated by braking rheostats. *Sensors*, 20(23), 2020.

[48] Feng Du, Zhen Liu, Weigang Chen, Yue Zhuo, and Michael Anheuser. A novel combined alternate current sensor for variable-frequency scenario. In *2017 IEEE International Workshop on Applied Measurements for Power Systems (AMPS)*, pages 1–5, 2017.

[49] Gabriella Crotti, Daniele Gallo, Domenico Giordano, Carmine Landi, and Mario Luiso. Industrial comparator for smart grid sensor calibration. *IEEE Sensors Journal*, 17(23):7784–7793, 2017.

[50] Antonio Cataliotti, Dario Di Cara, Alexander E. Emanuel, and Salvatore Nuccio. Improvement of hall effect current transducer metrological performances in the presence of harmonic distortion. *IEEE Transactions on Instrumentation and Measurement*, 59(5):1091–1097, 2010.

[51] Gabriella Crotti, Daniele Gallo, Domenico Giordano, Carmine Landi, and Mario Luiso. A characterized method for the real-time compensation of power system measurement transducers. *IEEE Transactions on Instrumentation and Measurement*, 64(6):1398–1404, 2015.

[52] Antonio Cataliotti, Dario Di Cara, Salvatore Nuccio, and Alexander E. Emanuel. Hall effect current transducer characterization under nonsinusoidal conditions. In *2009 IEEE Instrumentation and Measurement Technology Conference*, pages 98–103, 2009.

[53] Michele Norgia, Alessandro Pesatori, and Angelo Colombo. Temperature measurement system for train rheostat. In *2013 IEEE International Instrumentation and Measurement Technology Conference (I2MTC)*, pages 484–487, 2013.

[54] Andrea Mariscotti and Domenico Giordano. Experimental characterization of pantograph arcs and transient conducted phenomena in dc railways. *ACTA IMEKO*, 9:10–17, 06 2020.

[55] Andrea Mariscotti. Characterization of power quality transient phenomena of dc railway traction supply. *ACTA IMEKO*, 1:26, 07 2012.

[56] A. Mariscotti, D. Giordano. Discussion of power quality metrics suitable for dc power distribution and smart grids. https://doi.org/10.5281/zenodo.3604343, September 2019.

[57] Mario A. Suárez, Jorge W. González, and Israel Celis. Transient overvoltages in a railway system during braking. In *2010 IEEE/PES Transmission and Distribution Conference and Exposition: Latin America (T D-LA)*, pages 204–211, 2010.

[58] E. Pons, P. Colella, and R. Rizzoli. Overvoltages in dc urban light railway systems: Statistical analysis and possible causes. In *2018 IEEE International Conference on Environment and Electrical Engineering and 2018 IEEE Industrial and Commercial Power Systems Europe (EEEIC / I CPS Europe)*, pages 1–6, 2018.

[59] Andrés Emiro Díez, Mauricio Restrepo, Julián Vega, Camilo Meléndez, José Dariel Arcila, and Edison Manrique. A power quality case study of contact overhead lines in the medellin metro system. In *2019 IEEE Workshop on Power Electronics and Power Quality Applications (PEPQA)*, pages 1–6, 2019.

[60] Hamed Jafari Kaleybar, Morris Brenna, Federica Foiadelli, Seyed Saeed Fazel, and Dario Zaninelli. Power quality phenomena in electric railway power supply systems: An exhaustive framework and classification. *Energies*, 13(24), 2020.

[61] Antonio Delle Femine, Daniele Gallo, Domenico Giordano, Carmine Landi, Mario Luiso, and Davide Signorino. Power quality assessment in railway traction supply systems. *IEEE Transactions on Instrumentation and Measurement*, 69(5):2355–2366, 2020.

[62] IEC 61000-4-7 - Electromagnetic compatibility (EMC) - part 4-7: Testing and measurement techniques - general guide on harmonics and interharmonics measurements and instrumentation, for power supply systems and equipment connected thereto. Standard, August 2002.

[63] IEC 62313 - Railway applications - power supply and rolling stock - technical criteria for the coordination between power supply (substation) and rolling stock. Standard, 2009.

[64] Ravel F. Ammerman and P.K. Sen. Modeling high-current electrical arcs: A volt-ampere characteristic perspective for ac and dc systems. In *2007 39th North American Power Symposium*, pages 58–62, 2007.

[65] Wooho Kim, Yong-Jung Kim, and Hyosung Kim. Arc voltage and current characteristics in low-voltage direct current. *Energies*, 11:2511, 09 2018.

[66] Surajit Midya, Dierk Bormann, Thorsten Schutte, and Rajeev Thottappillil. Pantograph arcing in electrified railways—mechanism and influence of various parameters—part i: With dc traction power supply. *IEEE Transactions on Power Delivery*, 24(4):1931–1939, 2009.

[67] Andrea Mariscotti, Domenico Giordano, Antonio Delle Femine, and Davide Signorino. Filter transients onboard dc rolling stock and exploitation for the estimate of the line impedance. In *2020 IEEE International Instrumentation and Measurement Technology Conference (I2MTC)*, pages 1–6, 2020.

[68] Andrea Mariscotti, A. Marrese, Nicola Pasquino, Rosario Schiano, and Rosario Schiano Lo Moriello. Time and frequency characterization of radiated disturbance in telecommunication bands due to pantograph arcing. *Measurement*, 46:4342–4352, 05 2013.

[69] D. Signorino, D. Giordano, A. Mariscotti, D. Gallo, A.D. Femine, F. Balic, J. Quintana, L. Donadio, and A. Biancucci. Dataset of measured and commented pantograph electric arcs in dc railways. *Data in Brief*, 31, 2020.

[70] Shiwu Yang, Jianzhao Tian, Hao Xu, Yong Cui, and Lei Chen. Analysis on harmonic current and its impact on track circuit in high speed railway. In *2016 IEEE International Conference on Intelligent Rail Transportation (ICIRT)*, pages 315–321, 2016.

[71] Trenitalia. Mascherafs. http://www.ansf.it/documents/19/3733556/370582-1.1%20(Maschera%20FS96).pdf.

[72] Antonio Delle Femine, Daniele Gallo, Domenico Giordano, Carmine Landi, Mario Luiso, and Davide Signorino. Power quality assessment in railway traction supply systems. *IEEE Transactions on Instrumentation and Measurement*, 69(5):2355–2366, 2020.

[73] Giordano D., Crotti G., Roccato P., Mariscotti A., Gallo D., Luiso M., Filippini N., Rossetta I., Spalvieri C., Biancucci A., Donadio L. Pantograph-catenary arc detection technique based on conducted effects measurement on railway supply system. https://doi.org/10.5281/zenodo.4587794, March 2021.